

# DISSERTATION

---

## **Application of CO as a tracer for dynamics in the polar winter middle atmosphere**

A study based on ground-based microwave observations in Kiruna

---

Vorgelegt der Universität Bremen,  
Fachbereich für Physik und Elektrotechnik,  
Institut für Umweltphysik

zur Erlangung des akademischen Grades  
Doktor der Naturwissenschaften (Dr. rer. nat.)

von

**Dipl. Phys. Christoph Gregor Hoffmann**

1. Gutachter: Prof. Dr. Justus Notholt
2. Gutachter: Priv.-Doz. Dr. Christian von Savigny

Eingereicht am 26. Januar 2012  
Promotionskolloquium am 20. April 2012



*Für meine Eltern*



# Abstract

The dynamics of the polar winter middle atmosphere exhibits a pronounced variability, which is of importance for other atmospheric components, especially for the ozone layer. The full extent of this variability has not been observed so far and the causes are not fully understood. The present thesis contributes to this field in diverse aspects from an observational perspective. The central point is the application of middle atmospheric CO as tracer for polar dynamics.

A time series of vertical CO profiles covering the two winters 2008/2009 and 2009/2010 is retrieved from ground-based microwave observations obtained with the Kiruna microwave radiometer (KIMRA) in Kiruna, northern Sweden ( $68^\circ$  N). A detailed analysis of the retrieval characteristics reveals among others that the KIMRA CO retrieval provides information between 40 km and 80 km altitude. All major features of the polar winter dynamics are identified in the obtained CO time series: the descent of mesospheric air during fall, the sudden stratospheric warmings, and the vortex breakups in spring.

A comparison of time-averaged CO profiles of the KIMRA dataset with all recent satellite datasets (MLS, ACE-FTS, and MIPAS) is presented. It is the first such comparison of ground-based microwave observations and satellite datasets. The comparison reveals that KIMRA is generally consistent with the satellite datasets below 65 km. However, the KIMRA profile shape deviates systematically from those of the satellite datasets and is strongly high-biased above 70 km altitude. This bias is likely connected to residual contributions from the thermosphere to the received signal. It does, however, not affect the temporal variability of CO, which is of major interest for dynamical studies.

The representation of the polar middle atmosphere dynamics in the comprehensive atmospheric model SD-WACCM4 is validated. This model version has recently been developed, so that the comparison with observations presented here is among the first. In particular, the simulated CO time series is compared to the KIMRA CO time series. This comparison is particularly challenging for the global model since it is only evaluated at one model grid point. Correlation coefficients between both CO time series are as high as 0.9. Since CO is a tracer for dynamics in this region, the comparison reveals that the polar winter middle atmosphere dynamics is very well represented in SD-WACCM4. Only the comparison of extracted rapid variations (time scales below 20 d) shows a lower correlation. This behavior is attributed to the gravity wave parametrization in SD-WACCM4.

Model studies are carried out to clarify the general meaning of the descent rates of mesospheric air, which have been derived from CO time series. It is shown that first, descent rates from local CO time series (representing ground-based observations) are comparable to those derived from zonal mean CO (representing satellite observations). Second, it is shown that CO-loss by processes other than descent (mainly horizontal dynamics) cannot be neglected during any period of the season, in contrast to a common assumption. It is proposed that the descent rates might be interpreted as the ‘effective’ velocity of mesospheric air.



# List of Publications

## Publications:

C. G. Hoffmann, U. Raffalski, M. Palm, B. Funke, S. H. W. Golchert, G. Hochschild, and J. Notholt. Observation of strato-mesospheric CO above Kiruna with ground-based microwave radiometry — retrieval and satellite comparison. *Atmos. Meas. Tech.*, 4:2389–2408, 2011. doi: 10.5194/amt-4-2389-2011

C. G. Hoffmann, D. E. Kinnison, R. R. Garcia, M. Palm, J. Notholt, U. Raffalski, and G. Hochschild. CO at 40-80 km above Kiruna observed by the ground-based microwave radiometer KIMRA and simulated by the Whole Atmosphere Community Climate Model. *Atmos. Chem. Phys. Discuss.*, 12:559–587, 2012. doi: 10.5194/acpd-12-559-2012

C. G. Hoffmann, M. Palm, J. Notholt, U. Raffalski, and G. Hochschild. A brief example on the application of remotely sensed tracer observations in atmospheric science — studying the impact of stratosphere-mesosphere coupling on polar ozone variability. In G. Lohmann, D. Wolf-Gladrow, J. Notholt, V. Unnikrishnan, K. Grosfeld, and A. Wegner, editors, *Earth System Sciences: Bridging the gaps between disciplines — A multi-disciplinary Helmholtz Graduate Research School*. Springer, submitted (publication scheduled for 2012)

M. Palm, C. G. Hoffmann, S. H. W. Golchert, and J. Notholt. The ground-based MW radiometer OZORAM on Spitsbergen — description and status of stratospheric and mesospheric O<sub>3</sub>-measurements. *Atmos. Meas. Tech.*, 3:1533–1545, 2010. doi: 10.5194/amt-3-1533-2010

## Conference contributions (first author):

C. G. Hoffmann, M. Palm, B. Funke, D. E. Kinnison, R. R. Garcia, U. Raffalski, S. H. W. Golchert, G. Hochschild, J. Notholt: Comparison of Middle Atmosphere CO datasets above Kiruna (68°N), VIIth MIPAS IMK/IAA Data User Meeting, Granada, 12-13 May 2011 (oral)

C. G. Hoffmann, U. Raffalski, M. Palm, D. E. Kinnison, R. R. Garcia, S. H. W. Golchert, G. Hochschild, J. Notholt: Ground-based Observations of the Tracer CO above the Arctic and the Comparison to SD-WACCM model data, 3rd HEPPA Workshop, Granada, 9-11 May 2011 (poster)

C. G. Hoffmann, U. Raffalski, M. Palm, S. H. W. Golchert, G. Hochschild, J. Notholt: Observation of the Descent of Mesospheric Air above the Arctic during the Northern Winter 2009/2010 using the Tracer CO, AGU Fall Meeting, San Francisco, 13-17 December 2010 (poster)

C. G. Hoffmann, U. Raffalski, M. Palm, S. H. W. Golchert, G. Hochschild, J. Notholt: Observation of the Descent of Mesospheric Air above the Arctic, COSPAR 38th scientific

---

assembly, Bremen, 18.-25. July 2010 (oral)

C. G. Hoffmann, U. Raffalski, M. Palm, S. H. W. Golchert, G. Hochschild, J. Notholt: Observation of Descending Mesospheric Air above the Arctic during the Three Winters 2007/2008 to 2009/2010 by Ground-based Microwave Radiometry, SCOSTEP's Symposium STP12, Berlin, 12-16 July 2010. (oral)

C. G. Hoffmann, U. Raffalski, M. Palm, S. H. W. Golchert, G. Hochschild, J. Notholt: Bestimmung von Absinkraten mesosphärischer Luft über der Arktis durch Messung des Tracers CO, DPG-Frühjahrstagung 2010, Hannover, 8-12 March 2010. (oral)

C. G. Hoffmann, M. Palm, G. Kopp, U. Raffalski, S. H. W. Golchert, G. Hochschild, J. Notholt: Measurement of Subsidence Rates in the Middle Atmosphere during the Winter Season over Northern Polar Regions, EGU General Assembly, Vienna, 19-24 April 2009 (poster)

# Contents

<b>1</b>	<b>Introduction</b>	<b>1</b>
<b>2</b>	<b>Key aspects of the middle atmosphere</b>	<b>5</b>
2.1	Basic definitions . . . . .	5
2.1.1	Coordinate systems, winds, and other basic quantities . . . . .	5
2.1.2	Volume mixing ratio . . . . .	6
2.1.3	Potential temperature . . . . .	7
2.1.4	Potential vorticity . . . . .	7
2.1.5	Chemical tracers . . . . .	7
2.2	Middle atmosphere dynamics . . . . .	8
2.2.1	Description of the mean circulation . . . . .	8
2.2.1.1	Zonal winds . . . . .	8
2.2.1.2	Meridional circulation . . . . .	9
2.2.2	Impact of atmospheric waves . . . . .	11
2.2.2.1	Exertion of force to the mean flow . . . . .	12
2.2.2.2	Mixing and redistribution of airmasses . . . . .	12
2.2.2.3	Introduction of variability . . . . .	13
2.2.3	Polar winter dynamics: the polar vortex . . . . .	13
2.2.3.1	Overall description of the polar vortex . . . . .	13
2.2.3.2	Impact of the polar vortex . . . . .	14
2.2.3.3	Variability of the polar vortex . . . . .	14
2.2.3.4	Sudden stratospheric warmings . . . . .	16
2.2.4	Influence of the middle atmosphere dynamics on tracer distributions	16
2.2.5	Residual circulation and TEM formalism . . . . .	18
2.2.6	Continuity equation . . . . .	20
2.3	A brief description of the polar ozone layer . . . . .	21
2.3.1	Basic ozone chemistry . . . . .	21
2.3.2	Polar ozone depletion . . . . .	22
2.3.3	Importance of the dynamical variability for polar ozone . . . . .	22
2.3.4	Effects of energetic particle precipitation . . . . .	23
2.4	CO in the middle atmosphere . . . . .	25
2.4.1	Chemistry of CO in the middle atmosphere . . . . .	25
2.4.2	CO as a tracer for polar dynamics . . . . .	26
2.4.2.1	Chemical timescales . . . . .	26
2.4.2.2	Spatial gradients . . . . .	26
2.4.2.3	Representation of dynamical features in CO time series . . . . .	27
2.4.2.4	A heuristic method to derive polar descent rates . . . . .	28
2.4.3	Previous and ongoing CO observations in the middle atmosphere . . . . .	28

---

<b>3</b>	<b>Microwave radiometry</b>	<b>33</b>
3.1	Microwave radiation in the atmosphere	33
3.1.1	Radiative transfer	33
3.1.1.1	Transfer equation	33
3.1.1.2	Rayleigh-Jeans equivalent brightness temperature	34
3.1.1.3	Solution of the transfer equation	34
3.1.2	The absorption coefficient	35
3.1.2.1	Rotational spectrum of CO	35
3.1.2.2	Line intensities	36
3.1.2.3	Line broadening	36
3.2	Microwave radiometer	37
3.2.1	Requirements	38
3.2.2	Calibration	39
3.2.2.1	Hot-cold calibration	39
3.2.2.2	Balanced calibration	40
3.2.3	Critical hardware parameters	40
3.2.3.1	Spectral resolution	41
3.2.3.2	Detection limit	41
3.3	Retrieval of vmr profiles from microwave spectra	42
3.3.1	Inversion	42
3.3.2	Characterization of the retrieval results	43
3.3.2.1	Sensitivity	44
3.3.2.2	Vertical resolution	45
3.3.2.3	Degrees of freedom	45
3.3.2.4	Center altitudes of the AVKs	45
3.3.3	Error estimation	45
<b>4</b>	<b>Retrieval of the KIMRA CO data</b>	<b>47</b>
4.1	Properties of the KIMRA CO measurements	47
4.1.1	Measurement location	47
4.1.2	Instrument	47
4.1.3	Dataset	48
4.2	Retrieval setup	50
4.2.1	Forward model and inversion software	50
4.2.2	Numerical setup	50
4.2.3	Input data	51
4.2.4	Inclusion of instrumental properties	52
4.2.5	A remark about the line broadening of thermal CO emission	52
4.3	Characterization of the retrieval results	54
4.3.1	Average characteristics	55
4.3.1.1	Sensitivity	55
4.3.1.2	Center altitudes of the AVKs	55
4.3.1.3	Vertical resolution	57
4.3.2	Individual AVK functions	57
4.3.3	A remark about the spectral resolution of the instrument	58
4.3.4	Summary of retrieval performance	59

4.4	Retrieval Results . . . . .	60
4.4.1	A typical KIMRA CO retrieval result . . . . .	60
4.4.2	Complete retrieved KIMRA CO time series . . . . .	61
4.5	Error estimation . . . . .	63
4.5.1	Setup of the error estimation . . . . .	63
4.5.2	Results of the error estimation . . . . .	64
4.5.3	Variation of the a priori . . . . .	66
4.6	Summary . . . . .	68
<b>5</b>	<b>Comparison of the KIMRA CO with satellite observations</b>	<b>71</b>
5.1	Computation of time-averaged profiles . . . . .	72
5.2	Satellite datasets . . . . .	73
5.3	Comparison with MLS . . . . .	74
5.3.1	Influence of the collocation criteria . . . . .	74
5.3.2	Influence of the measurement period . . . . .	77
5.4	Multi-instrument comparison . . . . .	77
5.5	Discussion of the KIMRA profile shape deviation . . . . .	78
5.6	Summary . . . . .	82
<b>6</b>	<b>CO-based validation of the polar dynamics in the model SD-WACCM4</b>	<b>83</b>
6.1	The Whole Atmosphere Community Climate Model (WACCM) . . . . .	84
6.1.1	Context: Community Earth System Model . . . . .	84
6.1.2	Description of WACCM4 . . . . .	84
6.1.3	Description of SD-WACCM4 . . . . .	85
6.2	Comparison of the CO time evolution . . . . .	86
6.2.1	Datasets and preprocessing . . . . .	86
6.2.2	Visual inspection of the time series . . . . .	87
6.2.3	Correlation analysis . . . . .	88
6.2.3.1	KIMRA–MLS comparison . . . . .	88
6.2.3.2	KIMRA–SD-WACCM4 comparison . . . . .	90
6.2.4	Interpretation of the correlation analysis . . . . .	92
6.3	Summary and future perspectives . . . . .	95
<b>7</b>	<b>On the essence of descent rates derived from CO time series</b>	<b>97</b>
7.1	Descent rates derived from KIMRA CO and SD-WACCM4 CO . . . . .	98
7.1.1	Numerical implementation . . . . .	98
7.1.2	Derived descent rates of the winter 2009/2010 . . . . .	98
7.2	Simulation of CO evolutions for realistic and ideal conditions . . . . .	100
7.2.1	Implementation of the one-dimensional vertical advection simulation	101
7.2.2	Comparison of the simulated CO evolutions . . . . .	102
7.2.3	Interpretation of the simulation results . . . . .	102
7.3	Comparison of the descent rates and the TEM wind in SD-WACCM4 . . .	106
7.4	Future research and an alternative interpretation of the descent rates . . .	107
7.5	Summary . . . . .	108
<b>8</b>	<b>Summary and Outlook</b>	<b>109</b>

<b>Appendix</b>	<b>115</b>
<b>A Comparison of the time-averaged CO profiles including SD-WACCM4</b>	<b>115</b>
<b>List of Figures</b>	<b>117</b>
<b>List of Tables</b>	<b>119</b>
<b>Acronyms</b>	<b>121</b>
<b>Symbols</b>	<b>125</b>
<b>Bibliography</b>	<b>129</b>

# 1 Introduction

The dynamics of the polar middle atmosphere shows, particularly in the Arctic, pronounced variability on different time scales. This variability has a strong influence on the ozone layer, one of the key components of the climate system. Most aspects of the variability are still not fully understood and are unpredictable, despite several decades of observations and research. The impact of this variability became remarkably obvious in spring 2011, when extraordinary dynamical conditions lead to the strongest Arctic ozone depletion on record. It was the first time that Arctic ozone depletion reached the order of the Antarctic ozone hole [Manney et al., 2011].

The basic state of the polar winter middle atmosphere is dominated by the ‘polar vortex’, a strong, circumpolar, westerly wind located between the polar region and the mid-latitudes. This wind is associated with a barrier against meridional transport and thus isolates polar air masses from mid-latitude air. This isolation, together with the polar night, allows for low temperatures, which is the major precondition for polar ozone depletion in spring. However, there is also a meridional component of the circulation directed toward the winter pole, which leads to convergence and descent of air above the polar region. Although being weaker than the zonal component, the meridional circulation has a strong impact on the distribution of trace species [e.g., Andrews et al., 1987].

For a consistent understanding of the middle atmosphere dynamics, it is essential to consider the impact of atmospheric waves and wave breaking. The latter turns out to be the driver of the meridional circulation [e.g., Holton and Alexander, 2000] and, furthermore, to be the cause for large parts of the observed dynamical variability [e.g., Fritts et al., 2006]. Complex interactions of wave processes and the mean flow as well as the associated variability are therefore thought to be the main reason for the development of extreme events, particularly in the northern hemisphere.

The record-breaking ozone loss in 2011 and further extreme events observed in the last years demonstrate that the full range of conditions, which the winter middle atmosphere can exhibit, has not been observed so far. Hence, the extent and the particular causes of natural variability are still unclear, although the potential for extreme cases is known to be high [Manney et al., 2011]. However, the middle atmosphere research has been most intense in the altitude range containing the major part of the ozone layer, the lower stratosphere. Consequently, knowledge on the upper stratosphere and the mesosphere is more uncertain. For example, the vertical extent of the polar vortex and the strength of the mixing barrier are expected to decrease with increasing altitude. However, clear and consistent information on the vertical variability throughout the middle atmosphere is scarce in the literature. Whereas, for example, Schoeberl and Hartmann [1991] state that 30 km altitude “roughly marks the top of the highly isolated region of the polar vortex”, Randall et al. [2006] describe an “exceptionally strong” polar vortex at the stratopause altitude (approximately 50 km), suggesting that a ‘strong vortex’ is generally expected in this region. These statements are not necessarily contradictory, but show that knowledge

is still vague in this region, in addition to the actual variability of the described states.

An important example of an area of ongoing research is the coupling of the mesosphere and stratosphere through the descent of air above the winter pole. This descent transports air with a mesospheric composition into the stratosphere. On the one hand, the polar stratosphere is therefore supplied with mesospheric ozone, which partly masks the ozone depletion caused by anthropogenic emissions of Chlorofluorocarbons (CFCs) [e.g., Manney et al., 1995]. On the other hand, the descent also transports ozone depleting substances into the stratosphere and, consequently, naturally intensifies ozone depletion [e.g., Randall et al., 2005]. Moreover, stratospheric temperatures are changed by the descent due to adiabatic heating, which has impacts on the ozone chemistry. Although the existence and general importance of the descent are well established, the detailed variability is only poorly quantified. In particular, the velocity and the persistence of the descent are of importance. These parameters control to which altitude the mesospheric air descends and therefore the strength of the impact on stratospheric ozone [e.g., Randall et al., 2005].

Another field of ongoing research is the evolution of major sudden stratospheric warmings (SSWs). These events represent the strongest disturbance that the polar winter middle atmosphere can exhibit; the zonal wind is reversed, so that the polar vortex and the associated mixing barrier vanish completely for a certain period, which has a strong impact on the temperature and composition of the polar air [e.g., Brasseur and Solomon, 2005]. There are many open questions and unexplained observations regarding the general evolution of SSWs. For example, the stratopause seems to appear at higher altitudes after SSWs. Another example is the fact that the descent of mesospheric air seems to be particularly strong when the vortex is reestablished after certain SSWs [e.g., Manney et al., 2009]. Note that the strongest SSW on record also occurred recently during the Arctic winter of 2008/2009. Contrarily, this winter was expected to develop comparatively undisturbed [Labitzke and Kunze, 2009; Manney et al., 2009], which further demonstrates that the understanding of the dynamical variability is incomplete.

The last example of ongoing research with respect to dynamical variability given here is the persistence of the polar vortex. Since the timing of the vortex breakup controls the time span during which the inner-vortex air develops separately, it has strong implications on the air composition in spring. Also this timing exhibits strong variability; in the Arctic, the breakup occurs within the time span of February to May [Vaugh and Rong, 2002].

A related, broad field of ongoing research is the mentioned impact of the dynamical variability on ozone. The general aims of this field are the separation of chemical and dynamical ozone changes [e.g., Tegtmeier et al., 2008a,b; Manney et al., 1995] as well as the detailed understanding of feedbacks between ozone variability and dynamics [e.g., Shindell et al., 1998].

Whereas questions related to the fundamentals of polar dynamics still remain open, new questions arise due to anthropogenic climate change. Climate change is expected to interact with the polar middle atmosphere dynamics through different mechanisms. The middle atmospheric zonal wind and the polar vortex strength are expected to change due to modified temperatures. Also the wave-driven meridional circulation is expected to change due to both a modification of the tropospheric wave excitation and interactions of the waves with the modified zonal middle atmosphere winds [e.g., Garcia and Randel, 2008]. Furthermore, reactions of the ozone layer to these modifications are expected to cause feedbacks via the stratospheric heat budget and the temperature distribution

---

[WMO, 2011]. Although a definite link has not been established, it should be noted in the context of climate change that the four most dynamically disturbed and warm Arctic winters as well as the two most quiet and cold Arctic winters on record occurred in the last decade [Manney et al., 2011]. Furthermore, the coldest winters have become colder during the last 40 years bearing a higher potential for severe ozone loss [Rex et al., 2006].

Concluding the examples of open questions, research on the polar winter middle atmosphere dynamics is on the one hand still fundamental research aiming at basic understanding of the observed natural variability. On the other hand, this fundamental research is directly linked to two major fields of strong current and public interest: the evolution of the ozone layer as well as the interaction with climate change. The present thesis contributes to the former, the basic understanding of the middle atmosphere dynamics, as will be shown below.

Comprehensive numerical models of the atmosphere are a powerful interface between these three research fields; particularly those models, which can be coupled to complete climate system models if required. The advancement of these models is therefore of continued importance. Similarly important is the validation of new model developments with observations, to prove the capability of reproducing particular atmospheric features; here the reproduction of the variability of the polar middle atmosphere dynamics. Such a successfully validated model then serves as a multi-purpose diagnostic tool to understand both the processes involved in the production of dynamical variability as well as the connections to ozone and climate change. In the long-term, the ability to predict the evolution of polar middle atmosphere winters using these models might be achieved. However, this ability is currently very limited [Manney et al., 2011].

Observations of various aspects of the middle atmosphere are therefore necessary for both a better understanding of the extent and causes of the strong variability and for an extension of the observational database that is available for model validations. However, observations of the middle atmosphere are still challenging. Due to the high altitude and low density, in-situ measurements (e.g., with balloon sondes or rocket experiments) are difficult to conduct. Therefore, most observations are based on remote sensing of electromagnetic radiation, which carries information on different atmospheric parameters like trace gas abundances or temperature. Information on dynamics must, however, often be gained indirectly from changes in the abundances of certain species. Species suitable for being such a ‘tracer’ for dynamics are those whose abundances are dominated by dynamics rather than chemistry.

The application of such a tracer approach is the central point of the present thesis. In particular, carbon monoxide (CO) is used as tracer for polar middle atmosphere dynamics. Although the potential of CO as tracer in this region has been known for some decades, it remains complex to attribute changes in CO to individual dynamical processes. The present thesis therefore aims at both the actual application of the tracer CO to gain information on polar dynamics and concurrently at a further critical investigation of the tracer capabilities of CO.

The basis for this study is a set of microwave spectra obtained with the ground-based Kiruna microwave radiometer (KIMRA) located in Kiruna, northern Sweden (68° N). A time series of CO profiles, covering large parts of the two winters 2008/2009 and 2009/2010, is ‘retrieved’ from this dataset in the present work. This CO time series,

which is completed by a detailed assessment of the retrieval characteristics and data quality, broadens the observational database related to the Arctic middle atmosphere dynamics and is available for further research.

The derived KIMRA CO dataset is compared with datasets of all three relevant satellite instruments MLS, MIPAS, and ACE-FTS to evaluate the consistency of these different observation techniques. This is the first detailed comparison of ground-based microwave measurements of middle atmosphere CO with satellite observations, despite the number of published ground-based CO datasets.

The KIMRA CO time series is used to validate the representation of the polar middle atmosphere dynamics in a recently developed atmospheric model. The examined model, SD-WACCM4, is a special version (driven with specified dynamical fields, ‘SD’) of the comprehensive, established Whole Atmosphere Community Climate Model, version 4 (WACCM4) [Garcia et al., 2007]. It is therefore expected to be a powerful tool for atmospheric research after its validation, particularly with respect to the open questions outlined above. SD-WACCM4 has the advantage compared to WACCM4 that it is not completely free-running, so that simulation results are directly comparable to a specific set of measurements. The comparison with the KIMRA CO dataset, presented in this thesis, is one of the first utilizations of this feature. To overcome the difficulties, mentioned before, in the attribution of dynamical properties to features in the CO time series, the CO evolutions as measured by KIMRA and simulated by SD-WACCM4 are compared directly, instead of a comparison of dynamical quantities. This indirect examination of the model dynamics is the most robust application of CO as tracer.

CO time series have been used several times to derive ‘descent rates’ of the polar winter descent of mesospheric air [Allen et al., 2000; Forkman et al., 2005; Funke et al., 2009; Di Biagio et al., 2010]. For the attribution of these descent rates to the actual vertical velocity, the descent must have continuously been the dominating influence on CO. Although being questionable, this is a common assumption for the derivation of descent rates. Also in the present study, descent rates are derived from the KIMRA CO time series based on this assumption. The major aspect here is, however, the investigation of an adequate interpretation of the derived descent rates, considering a potential violation of this assumption. This is tackled by a comparison of two different simulated CO evolutions; first, CO produced by SD-WACCM4, which is regarded as representing the real atmosphere, and second, an ideal CO time series, which is certainly only affected by vertical descent.

This thesis is organized as follows. The known key aspects of the middle atmosphere are reviewed in Chapter 2. The basics of microwave radiometry and the retrieval technique are outlined in Chapter 3, whereas the retrieval of the KIMRA CO profiles and the characterization of the dataset are presented in Chapter 4. The comparison of the KIMRA CO to satellite observations is discussed in Chapter 5. The validation of the model SD-WACCM4 is presented in Chapter 6. Finally, the interpretation of derived descent rates is elaborated on in Chapter 7, before the thesis is summarized in Chapter 8. Furthermore, each of the chapters presenting results (Chapters. 4–7) contains an individual summary.

## 2 Key aspects of the middle atmosphere

The ‘middle atmosphere’ is a generic term for the two atmospheric layers stratosphere and mesosphere. These layers share many features, for example the forcing of the dynamical circulation. The middle atmosphere covers the altitude range from about 15 km to 80 km and is enclosed by the troposphere at the bottom and the thermosphere at the top (Fig. 2.1). The basic feature unique to the stratosphere is the ‘ozone layer’, a maximum of the ozone abundance in the vertical. The ozone layer absorbs solar ultraviolet (UV) radiation, which heats the stratosphere from its interior and leads to a temperature increase with altitude. A local vertical temperature maximum, the stratopause, marks the transition to the mesosphere at about 50 km altitude. The mesosphere is characterized by again decreasing temperatures with altitude. Here, effects of penetrating high energetic particles from the sun and from space become important, which have implications for the mesospheric chemistry. Since these effects are similar in the mesosphere and lower thermosphere, both regions are often considered together as the mesosphere-lower thermosphere (MLT) region.

This chapter explains basic properties of the middle atmosphere, which are of general importance for the understanding of this study. Aside from the various references in the text, the textbooks Andrews et al. [1987], Brasseur and Solomon [2005], and Holton [2004] have generally been used to compile this information.

### 2.1 Basic definitions

#### 2.1.1 Coordinate systems, winds, and other basic quantities

The geometric altitude  $z$  is mostly used as vertical coordinate throughout this thesis. However, pressure  $p$  is partly used in internal calculations and the ‘log-pressure’ vertical coordinate is partly used in the theoretical framework,

$$z_{\log p} = -H \ln \left( \frac{p}{p_0} \right) \quad (2.1)$$

with  $p_0$  a standard pressure level (usually 1000 hPa) and the scale height  $H = g_0^{-1} R \bar{T}_S$ .  $H$  equals approximately 7 km using a standard mean temperature  $\bar{T}_S$  for the middle atmosphere of 240 K, the standard gravity  $g_0$ , and the gas constant for air  $R$ . The log-pressure coordinate is monotone with  $z$  and since the differences to  $z$  are small, they are only relevant for detailed quantitative considerations, in contrast to the application here. Therefore, the log-pressure coordinate will be denoted for convenience in the following

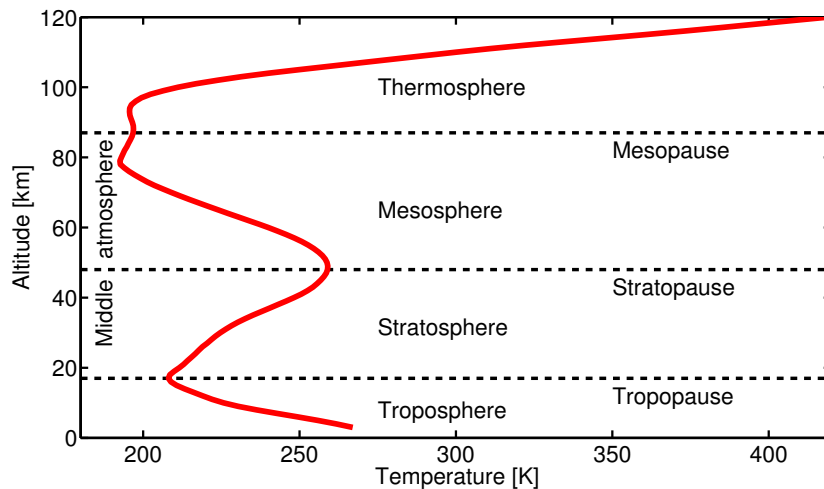


Figure 2.1: Global and annual mean vertical temperature profile of the atmosphere as simulated by SD-WACCM4<sup>1</sup> for the year 2009. The individual atmospheric layers (‘spheres’) defined by the temperature gradient are obvious. The regions between these layers (‘pauses’) are marked with dashed lines. The ‘middle atmosphere’ is a generic term for the stratosphere and the mesosphere.

simply as  $z$ , similar to the geometric altitude. However, the use of log-pressure coordinates is explicitly mentioned where appropriate.

As horizontal coordinates, either spherical coordinates with the latitude  $\phi$  and the longitude  $\lambda$  or local Cartesian coordinates with  $x$  in the zonal direction and  $y$  in the meridional direction are used. Furthermore, the components of the wind vector  $\frac{dx}{dt}$ ,  $\frac{dy}{dt}$ , and  $\frac{dz}{dt}$  in the zonal, meridional, and vertical direction, respectively, are denoted with  $u$ ,  $v$ , and  $w$ , which also applies in spherical coordinates.

Other quantities generally used here are the density  $\rho$ , the basic density  $\rho_0 = p (R\bar{T}_S)^{-1}$ , the Coriolis parameter  $f = 2\Omega \sin \phi$ , with  $\Omega$  denoting the angular speed of the rotation of the earth, and the earth’s radius  $r$ .

## 2.1.2 Volume mixing ratio

The volume mixing ratio (vmr)  $\chi$  is a measure for the abundance of a trace constituent in the atmosphere; the respective number density  $n_T$  is normalized with the total air number density  $n_{\text{Air}}$  in a given volume.

$$\chi = \frac{n_T}{n_{\text{Air}}} \quad (2.2)$$

The vmr is conserved following the motion of an air parcel and is only changed by sources or sinks. Commonly, vmrs are expressed in the ‘parts per’ notation; in this work the unit ‘parts per million by volume’ (ppmv) is used, which corresponds to a fraction of  $10^{-6}$ .

<sup>1</sup>Data of the model SD-WACCM4 will be used several times for illustrations in the following. The model data is expected to be close to the real atmosphere. This is shown in the present thesis below, which also includes a model description (Chap. 6).

### 2.1.3 Potential temperature

The potential temperature  $\theta$  is the temperature, which an air parcel with temperature  $T$  at a pressure level  $p$  would have, if it were adiabatically transferred to a standard pressure  $p_0$ . It is given by Poisson's equation,

$$\theta = T \cdot \left[ \frac{p_0}{p} \right]^{\frac{R}{c_p}}, \quad (2.3)$$

with  $c_p$  denoting the specific heat of air under constant pressure. Potential temperature is conserved for adiabatic motions in the atmosphere. Hence, adiabatic air movement takes place on lines of constant potential temperature, on the 'isentropes'.

### 2.1.4 Potential vorticity

The potential vorticity (PV)  $P$  is an important quantity that is conserved for adiabatic, frictionless motion of air. It is a measure of the angular momentum of fluids, so that the conservation of PV is related to the conservation of angular momentum of a rigid body. The concept of PV provides powerful tools and diagnostics for atmospheric analyses, so that it is extensively described in the mentioned textbooks as well as in McIntyre [2003]. PV is generally defined as  $P = \rho^{-1} \boldsymbol{\omega}_a \cdot \nabla \theta$  with the absolute vorticity  $\boldsymbol{\omega}_a$  (see mentioned literature). The actual expression for  $P$  used in computations depends on the applied approximations and coordinate systems. The expression used throughout this study is based on pressure coordinates in the vertical and spherical coordinates in the horizontal [Andrews et al., 1987, Eq. 3.1.4, transformed to pressure coordinates],

$$P = -g_0 \left\{ \frac{\partial \theta}{\partial p} \left[ f - \frac{\partial}{\partial \phi} (u \cos \phi) + \frac{\partial v}{r \cos \phi} \right] - \frac{\partial \theta}{\partial \lambda} \frac{\partial v}{r \cos \phi} + \frac{\partial \theta}{\partial \phi} \frac{\partial u}{r} \right\}. \quad (2.4)$$

The Coriolis parameter  $f$  represents a background PV field with a positive meridional PV gradient on isentropic surfaces. This hinders a meridional shift of air masses since air parcels in adiabatic, frictionless flow move along isocontours of PV due to the PV conservation. Particularly in regions with stronger PV gradients, air masses that encounter a meridional shift experience a restoring force, which implies the existence of Rossby waves (Sect. 2.2.2). Regions with strong meridional PV gradients on isentropic surfaces act therefore as 'barriers' against meridional transport [e.g., Holton, 2004], which is important for the polar winter middle atmosphere (Sect. 2.2.3).

Due to the conservation of PV, this quantity is a useful dynamical tracer, i.e., it can be used to distinguish different air masses and to track their positions. Special about the PV is thereby that it is derived from purely meteorological data (winds and temperature), which are comparatively easy to observe. Furthermore, PV is not only advected with the flow field like other tracers, but determines the flow itself. It can therefore be inverted to obtain the wind and temperature fields ('PV inversion', see McIntyre [2003]).

### 2.1.5 Chemical tracers

In addition to dynamical tracers as the PV, chemical tracers can be used to identify particular air masses and to track their motions. Chemical tracers are trace constituents whose

‘chemical timescale’ is of similar order of magnitude as the ‘dynamical timescale’ [e.g., Holton, 2004]. The chemical timescale is a measure for the average time needed to remove or replace the respective trace constituent chemically. The dynamical timescale measures the time needed for advective or diffusive processes to transport the trace constituent over characteristic distances, e.g., from the equator to the pole. Since these quantities are variables in space and time, the tracer property of a trace constituent may be limited to a certain atmospheric region.

The condition that chemical and dynamical timescales have to be of the same order of magnitude is understood best by considering the opposite cases. First, if the chemical timescale were much shorter, the trace substance abundance would have changed chemically before a significant transport had occurred; the substance would therefore be in chemical equilibrium and thus not directly be influenced by transport. Second, if the chemical timescale were much longer than the dynamical timescale, the dispersive nature of the atmospheric transport would distribute the trace substance equally throughout large regions of the atmosphere. Therefore the trace constituent abundance would be no distinctive property of one air mass anymore.

In conclusion, the chemical time scale of a potential tracer for dynamics must, on the one hand, be long enough compared to the dynamical timescale, so that transport has a significant influence on the distribution. On the other hand, it has to be short enough to maintain abundance differences in certain regions, thus abundance gradients.

## 2.2 Middle atmosphere dynamics

The main motion systems in the middle atmosphere are generally of planetary scale. The basic principles of the middle atmosphere circulation are well established and have been described extensively in textbooks [e.g., Andrews et al., 1987] and review papers [e.g., Shepherd, 2007], so that the present description is focused on the polar regions. Furthermore, the discussion here is intentionally kept on a qualitative level to stress the basic ideas. Nevertheless, the mathematical basis is briefly sketched in Sect. 2.2.5.

### 2.2.1 Description of the mean circulation

#### 2.2.1.1 Zonal winds

The zonal mean wind in the middle atmosphere for near-solstice conditions is basically given by the geostrophic approximation [e.g., Brasseur and Solomon, 2005]; in the winter hemisphere, the temperature and the pressure over the pole drop due to missing sunlight during the polar night, so that the pressure gradient force points from the equator to the pole. The Coriolis force acts on the resulting poleward flow, such that it balances the pressure gradient force (Fig. 2.2, left). As a result, the flow is turned into a zonal, circumpolar, westerly wind. The region, which is enclosed by this strong zonal jet and roughly centered above the winter pole, the ‘polar vortex’, is in the focus of this work and discussed in detail below (Sect. 2.2.3).

According to the thermal wind relation [e.g., Brasseur and Solomon, 2005],

$$\frac{\partial u}{\partial z} = -\frac{R}{H} \frac{1}{f r} \frac{\partial T}{\partial \phi}, \quad (2.5)$$

the zonal wind speed increases with altitude, leading to a maximum at approximately 60 km altitude [Holton, 2004]. Above, the wind speed decreases again. As will be shown below (Sect. 2.2.2), a third force is of great importance for a consistent understanding of this observation. This force, which is exerted by the breaking of atmospheric waves, acts mainly in the opposite direction of the mean zonal flow. The observed wind speeds are therefore generally lower than expected from the geostrophic theory alone and decrease with altitude above 60 km. Nevertheless, the observed wind speeds are with 80 m/s at the maximum still much higher than in the troposphere [Holton and Alexander, 2000]. Furthermore, the wave forcing is thought to be responsible for a reversal of the direction of the zonal winds above the mesopause [Holton and Alexander, 2000].

The zonal wind in the summer hemisphere is similarly explained by a geostrophic approximation. There, the pressure is higher over the pole, so that the pressure gradient force is directed from the pole to the equator, resulting in easterly winds (Fig. 2.2, left). The zonal winds in one particular hemisphere are therefore reversed seasonally.

### 2.2.1.2 Meridional circulation

The existence of a meridional circulation in the stratosphere was first suggested by Brewer [1949] and Dobson [1956]. It has been confirmed by many observations in the stratosphere and the mesosphere, so that its existence belongs to the established knowledge. However, considering merely the geostrophic explanation of the zonal wind (Sect. 2.2.1.1), there is no obvious reason for a meridional circulation, since any poleward flow is turned in the zonal direction. Instead, the already mentioned force exerted by wave breaking has to be taken into account for an understanding of the meridional circulation (this force is discussed in Sect. 2.2.2). The existence of this third force leads to a deviation from the geostrophic balance (Fig. 2.2, middle and right panel) and causes the meridional circulation, which is indicated in Fig. 2.3 by white arrows. Note that potential other non-conservative mechanical forcings, ‘friction’, are neglectable at this level of approximation.

In the stratosphere, the meridional flow is mainly directed from the equator to the winter pole and is driven by the breaking of ‘Rossby’ waves (Sect. 2.2.2). A possible meridional circulation from the equator to the summer pole is weak or does even not exist. The overall mesospheric meridional circulation is directed from the summer pole to the winter pole and is mainly driven by the breaking of gravity waves (Sect. 2.2.2).

Due to the continuity of mass, the meridional circulation also invokes a vertical branch of the middle atmosphere circulation. This branch is directed upwards above the equator (stratosphere) and the summer pole (upper stratosphere and mesosphere) and downwards above the high latitudes of the winter hemisphere, particularly in the polar vortex region. The latter, the descent of air within the polar vortex, is one of the main interests of this work (Sects. 2.2.3.2, 2.3.3, 2.4.2.4).

One implication of the vertical circulation, mentioned here only for completeness, is that the temperature distribution of the middle atmosphere is driven away from its radiative equilibrium by adiabatic heating and cooling in regions with descending and ascending air, respectively.

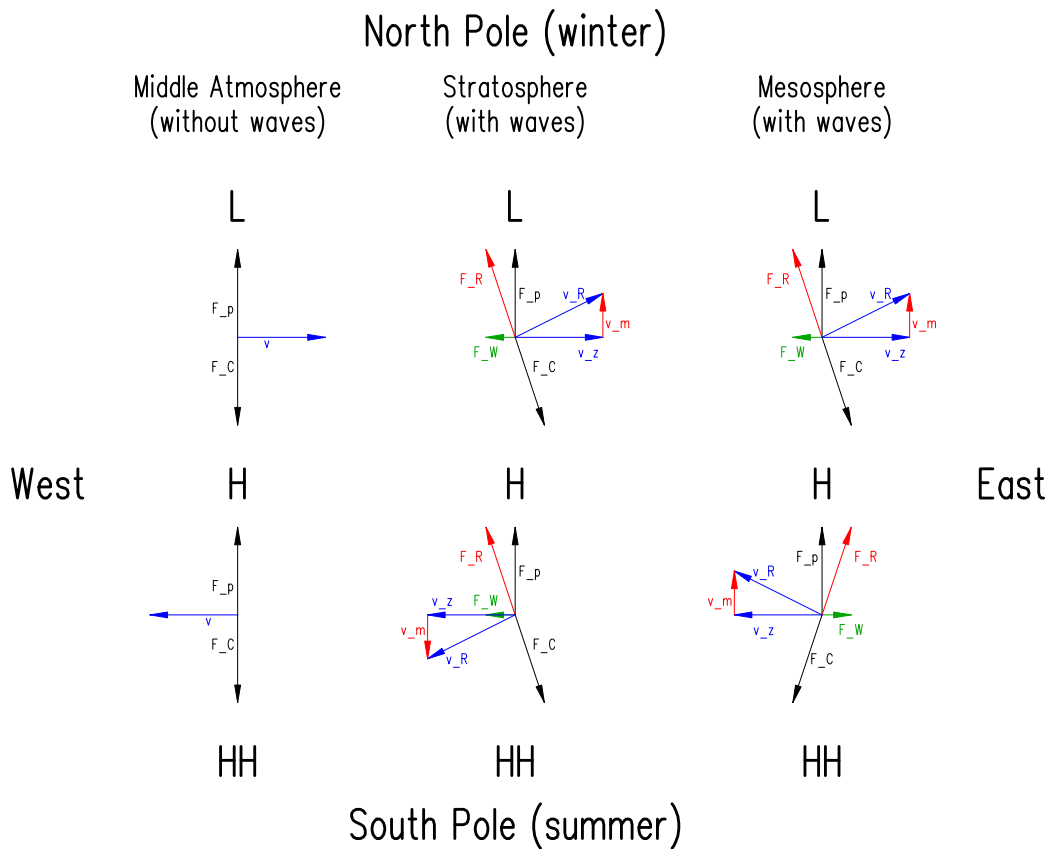


Figure 2.2: Sketch of forces driving the middle atmosphere circulation for northern winter and southern summer. The pressure distribution is denoted with ‘L’, ‘H’, and ‘HH’ from lower to higher pressure, respectively. Arrows denote only the directions of the forces, whereas the relative strengths are not reproduced correctly; particularly the summer stratospheric circulation is weaker. **Left:** Hypothetic situation of a geostrophic flow, i.e., without wave influence. The pressure gradient force (here  $F_p$ ) is balanced by the Coriolis force (here  $F_C$ ) leading to a zonal flow (here  $v$ ). **Middle:** Approximation of the stratospheric situation including a wave force (here  $F_W$ ). Together with  $F_p$  this wave force leads to a new resulting force (here  $F_R$ ), which is balanced by  $F_C$ , so that a meridional component of the wind (here  $v_m$ ) is introduced. **Right:** Situation with waves for the mesosphere. It is similar to the stratosphere in the winter hemisphere, but different in summer, since  $F_W$  points to the opposite direction (see Sect. 2.2.2).

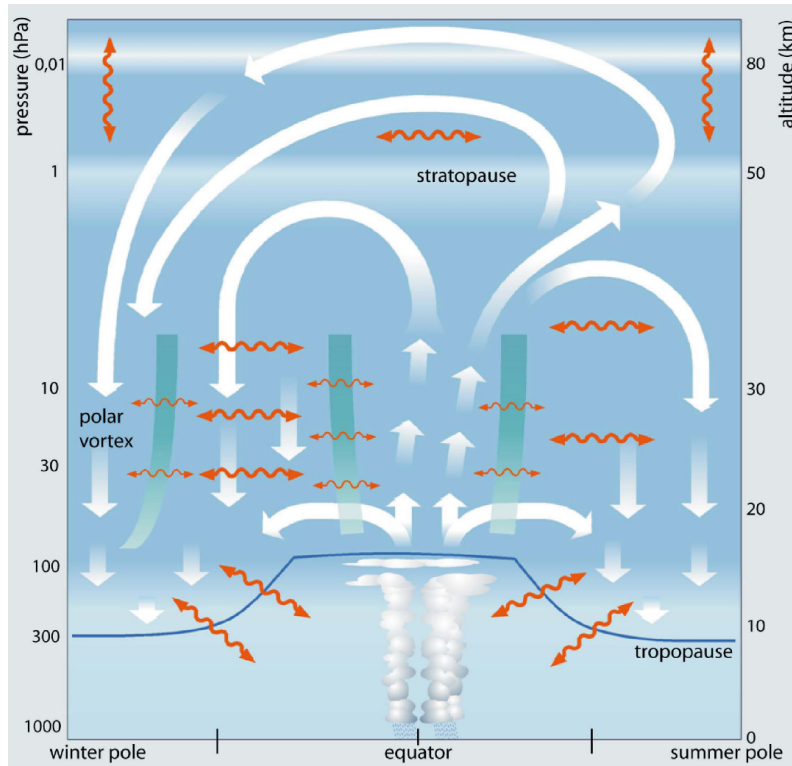


Figure 2.3: Sketch of the meridional circulation in the middle atmosphere, showing among others the stratospheric branch from the equator to the winter pole and the mesospheric branch from the summer pole to the winter pole. Both branches lead to descending air above the winter pole. Furthermore, turbulent mixing is indicated by orange wavy arrows. Heavy arrows correspond to regions with strong mixing (e.g., the ‘surf zone’ in the mid-latitude winter stratosphere), whereas light arrows indicate weak mixing across the transport barriers. Adopted from Bönisch et al. [2011].

### 2.2.2 Impact of atmospheric waves

Atmospheric waves, particularly the breaking of atmospheric waves, play a major role in the middle atmosphere dynamics [Holton and Alexander, 2000]. The two relevant types of waves in the polar middle atmosphere are ‘Rossby waves’ and ‘gravity waves’. Rossby waves are related to the conservation of PV, whereas gravity waves owe their existence to the buoyancy restoring force. Details on these wave types are discussed in the textbooks mentioned before or in, e.g., Holton and Alexander [2000]. Note that it is too complex to distinguish entirely between the two wave types in the following. Thus, the present discussion is only intended to give a rough idea of the general role of atmospheric waves in the context of this work.

The relevant waves are generated mainly in the troposphere by different processes (flow over topography, convection, weather fronts, geostrophic adjustment processes) and propagate upwards through the middle atmosphere. Depending on their properties (type, wavenumber, phase speed) and their environment (mainly zonal winds), certain waves are not able to propagate through particular altitudes, so that they are ‘filtered out’.

Therefore, the spectrum of waves, which are present at a particular altitude, is basically reduced with increasing altitude.

The waves that encounter levels through which they cannot propagate break in the respective altitudes, which is of major interest for the middle atmosphere dynamics. Wave breaking is defined as a “rapid, irreversible deformation of material contours”<sup>2</sup> [Holton, 2004]. For an intuitive understanding of this process, one might think of ocean waves, which break at the beach; away from the beach a wave is defined by the undulating surface of the water. The amplitude grows while the wave approaches the beach until the overturning takes place. During this process the energy and momentum associated with the wave dissipate through the turbulent motion. Although this analogy should not be stressed too much, there are also undulating quantities constituting the atmospheric waves (e.g., PV contours for Rossby waves). The amplitudes of these undulations grow exponentially while the wave propagates vertically through the atmosphere, which is explained by the decreasing air density. Finally, atmospheric waves also overturn during the breaking event and transfer their energy and momentum to the mean flow. A careful analysis of the propagation properties reveals the fact mentioned before; Rossby wave breaking is mainly relevant in the stratosphere, whereas gravity wave breaking dominates in the mesosphere [Holton and Alexander, 2000].

### 2.2.2.1 Exertion of force to the mean flow

One major implication of the breaking of atmospheric waves is that this process transfers momentum to the mean flow. Hence, wave breaking exerts a force, which is crucial for the existence of the meridional circulation (Sect. 2.2.1.2). Again, the ocean wave analogy may be helpful for an intuitive understanding; surfers use exactly the fact that breaking waves exert a force on their surf boards to accelerate.

For a complete understanding of all branches of the meridional circulation, it is necessary to evaluate the directions of the exerted forces in consideration of the atmospheric region and the season. The main outcome of these considerations [e.g., discussed by Holton and Alexander, 2000] is that the filtering of waves is controlled by the zonal winds, such that the exerted force always weakens the zonal flow (Fig. 2.2). The only exception is the summer stratosphere, where this force is weak anyway. Consequently, the seasonal reversal of the zonal winds implies also a seasonal reversal of the meridional circulation.

Note that the region where Rossby wave breaking dominantly occurs, the mid-latitude winter stratosphere, has consequently been named ‘surf-zone’ [McIntyre and Palmer, 1984].

### 2.2.2.2 Mixing and redistribution of airmasses

Another important implication of wave breaking, as irreversible deformation of material contours, is the introduction of turbulence. It causes mixing of air masses and homogenizes the air constituents in regions with strong wave breaking, e.g., in the surf-zone. Due to its impact on the PV field, Rossby wave breaking can also lead to mixing across transport barriers originating from strong PV gradients [e.g., Brasseur and Solomon, 2005]. Since

---

<sup>2</sup>The term ‘material contours’ refers to contours of distinctive properties of air masses. They are, e.g., realized by the contours of long-lived tracers or PV.

Rossby wave breaking is accompanied by an irreversible deformation of the PV contours, it can, moreover, lead to a redistribution of the PV field [McIntyre and Palmer, 1983] and thus to a modification of PV gradients. This is important for the development and erosion of the transport barrier associated with the polar vortex (Sect. 2.2.3).

### 2.2.2.3 Introduction of variability

Processes including waves and wave breaking are frequently highly variable; a fact that appears intuitively plausible. Here, the physical reasons are not the major point, so that they are only briefly mentioned (see, e.g., Fritts et al. [2006] for a review on gravity wave variability). First, the sources of waves are partly highly variable themselves, e.g., the generation of gravity waves by convective weather systems in the troposphere. Second, after their generation, waves propagate vertically through—and may experience modifications by—the lower atmosphere, which exhibits high variability itself (meteorological processes). Third, the relevant processes of wave propagation and breaking involve non-linear interactions with other waves or the mean flow, which may even amplify variability.

Of major importance for the middle atmosphere is the fact that this intrinsic variability is transferred to the middle atmospheric properties by wave propagation and breaking. It is therefore expected that the middle atmosphere dynamics exhibits pronounced variability on different time scales. Particularly gravity waves, which exist in a wide range of spatial scales (wavelengths of 10 km to 1000 km [Brasseur and Solomon, 2005]), are expected to create also pronounced spatial variability and therefore to have a strong local influence.

Since one important source of atmospheric waves is the flow over topography, the unequal distribution of land masses on the earth is also reflected in the middle atmosphere dynamics. Much more waves are excited in the Northern Hemisphere (NH), which finally results in the fact that the NH middle atmosphere exhibits much more variability than the Southern Hemisphere (SH).

## 2.2.3 Polar winter dynamics: the polar vortex

### 2.2.3.1 Overall description of the polar vortex

In the winter hemisphere, the middle atmosphere circulation is dominated by the strong, circumpolar, westerly wind (Sect. 2.2.1.1), which is accompanied by a strong meridional PV gradient forming an effective transport barrier (Sect. 2.1.4). The region enclosed by this barrier (roughly poleward from 60° latitude) is the ‘polar vortex’, whose air is identified by high absolute PV values (Fig. 2.4). On the other side of the transport barrier, mid-latitude air with lower PV values is found; a picture that was established by McIntyre and Palmer [1983, 1984].

The strong zonal wind and the strong mixing barrier are often mentioned in the same breath. However, the existence of the strong PV gradient is subject to a complex interaction of the zonal jet, wave activity and PV redistribution (Sect. 2.2.2). This interaction involves positive feedback mechanisms that flatten the PV gradient in the surf-zone and further sharpen the strong PV gradient that constitutes the vortex boundary [McIntyre and Palmer, 1984; Dritschel and McIntyre, 2008]. Generally, the PV gradient serves as observable indicator for the vortex boundary (Fig. 2.4). However, Nash et al. [1996] pro-

pose a more sophisticated determination of the vortex edge employing additionally the zonal wind maximum to reduce uncertainty.

As mentioned before, the inner-vortex air descends during the course of the winter due to the meridional circulation and the continuity of mass (Sect. 2.2.1.2). This is an important feature of the polar vortex dynamics since it has a significant impact on different properties of the inner-vortex air, as discussed below (Sects. 2.2.3.2, 2.3.3).

### **2.2.3.2 Impact of the polar vortex**

Two distinct air masses are in principle identified in the extratropical winter middle atmosphere, the inner-vortex air and the mid-latitude air. Both air masses experience very different conditions under which they develop during winter; either mostly polar night or partly sunlight conditions, respectively. Therefore, many properties evolve differently, which results in strong horizontal gradients of certain quantities at the vortex edge. This is illustrated for PV, temperature, and the CO vmr in 50 km altitude for a day in October 2009 in Fig. 2.4; the two different air masses as well as the steep gradients can clearly be seen. These differences cannot be diminished by exchange of air during winter and become more pronounced during the course of the winter so that they are generally largest in late winter.

Special about the inner-vortex air evolution are particularly the following facts. The temperature of the vortex air is much lower since it is mostly exposed to the polar night and cools radiatively. The atmospheric chemistry is changed due to both, the missing sunlight and the lower temperatures. Therefore, some chemical reactions are slower or stop completely in the polar vortex, whereas other reactions based on heterogeneous chemistry are enabled (Sect. 2.3.2). This modified chemistry results in different abundances of trace gases in the polar vortex. Furthermore, the vertical descent of air above the winter pole (Sect. 2.2.1.2) also modifies the trace gas abundances in the polar vortex since air with a mesospheric composition enters the stratospheric polar vortex. There, the mesospheric composition is comparatively persistent since the modified chemistry prevents it from being as fast converted to the stratospheric composition as it would be the case under mid-latitude conditions. A key example for the implications of the special polar vortex conditions is the development of the Antarctic ozone hole (Sect. 2.3.2).

### **2.2.3.3 Variability of the polar vortex**

The static picture, drawn above, of the circular polar vortex with an impermeable transport barrier has to be refined to include the variability that is introduced by wave activity, among others. This is particularly important for the NH polar vortex, which is in the focus of this work. Since the wave activity is much stronger in the NH (Sect. 2.2.2), the vortex is also much more variable than in the SH. Consequently, the mixing barrier is not perfectly impermeable, but the degree of impermeability (also referred to as ‘vortex strength’) is highly variable and depends on the altitude and the time period. Generally, the polar vortex is weakened by wave breaking events, which lead to mixing across the transport barrier and disturb the PV gradient by pulling filaments of vortex air with high PV into the mid-latitudes, where they dissipate.

In terms of altitude, the mixing barrier exists from about 16 km on [Brasseur and Solomon, 2005], is assumed to be strongest in the lower and middle stratosphere and

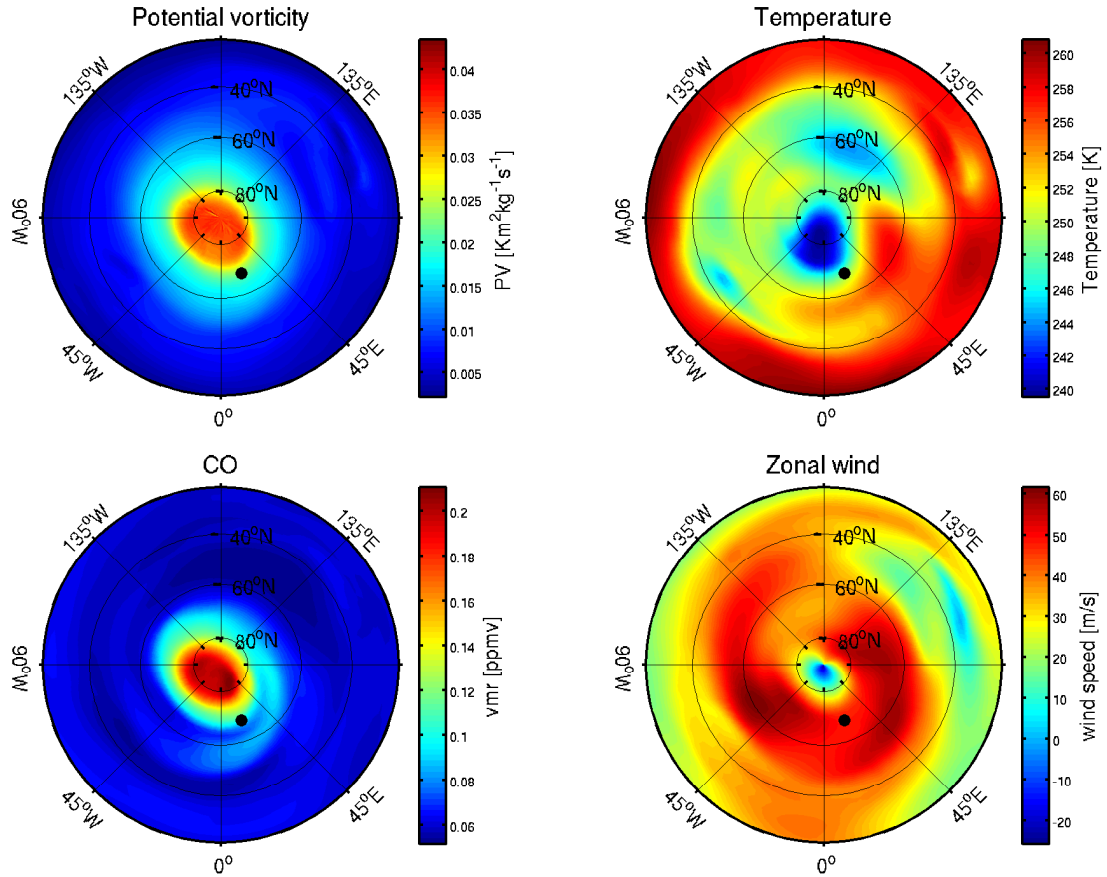


Figure 2.4: Manifestation of the Arctic polar vortex in the atmospheric parameters PV (**top, left**), temperature (**top, right**), CO vmr (**bottom, left**), and zonal wind (**bottom, right**) exemplified by SD-WACCM4 simulations for 17 October 2009 in 50 km altitude. The black dot marks Kiruna, the location of major interest in this work. The vortex with high PV, high CO, and low temperatures is easily identified, being roughly centered above the pole and enclosed by strong zonal winds.

weakens towards the mesosphere, where increasing amounts of mid-latitude air enter polar regions following the meridional circulation.

Variability of the vortex strength in time appears over a wide range of time scales. First, there is obviously a seasonal dependence, since the vortex is built up in fall and breaks down in spring (also referred to as ‘final warming’) in connection with the reversal of the zonal winds (Sect. 2.2.1.1). Second, there is variability on shorter time scales connected with the high variability of the wave activity. This intraseasonal variability is therefore more pronounced in the NH, where it frequently leads to sudden stratospheric warmings (SSWs), the strongest disturbance of the polar vortex (Sect. 2.2.3.4). Third, the polar winter dynamics of the middle atmosphere exhibits also interannual variability, which is introduced by different internal (e.g., the quasi-biennial oscillation (QBO) and quasi-decadal variability (QDV)) and external forcings (e.g., variations of solar insolation and variations of sea surface temperatures (SSTs)). The reader is referred to the review

by Hamilton [2000] and references therein for further reading on this topic.

Note that the temporal and spatial variability of many parameters of the polar vortex is only coarsely known and is a subject of ongoing research. The pure existence of the variability is, however, well-established (cf. Chap. 1).

#### **2.2.3.4 Sudden stratospheric warmings**

SSWs are the most pronounced features of intraseasonal variability of the polar winter middle atmosphere. During a SSW, the inner-vortex temperature increases strongly (up to 80 K in extreme cases [Brasseur and Solomon, 2005]) within just a few days. This temperature increase is accompanied with a weakening or even a reversal of the zonal westerly wind (Fig. 2.5) and a cooling in the mesosphere. Such an event is considered to be a ‘major’ SSW if the zonal wind actually reverses poleward of 60° latitude and above the 10 hPa pressure level [Brasseur and Solomon, 2005]. The initial reason for an SSW, which usually occurs in late winter or spring, is thought to be a complex interaction of enhanced Rossby wave activity with the mean flow (e.g., Brasseur and Solomon [2005]). Since the transport barrier is also strongly weakened, effective mixing with mid-latitude air is possible during the occurrence of a (major) SSW. Therefore, such an event usually strongly modifies the evolution of the inner-vortex air (Fig. 2.5) with some of the consequences persisting for the rest of the season.

Aside from being an example of the strong intraseasonal variability, the occurrence of SSWs exhibits itself interannual and inter-hemispheric differences. In the SH, relatively weak SSWs occur regularly in every winter with a comparable magnitude. A major SSW has only been observed once in the SH, namely in 2002 [WMO, 2011; Sinnhuber et al., 2003]. Contrarily, the SSW occurrence shows large interannual variability in the NH [Labitzke, 1981]. Particularly, major SSWs occur more frequently in the NH. The higher variability of NH SSWs generally corresponds to the higher wave activity in the NH (Sect. 2.2.2.3). Furthermore, links to the interannual variability of known phenomena as, e.g., the QBO or the solar sunspot cycle, could be established [Labitzke and Kunze, 2009]. This fact was thought to allow for rough predictions of the SSW occurrence in particular winters. However, in the winter 2008/2009 the strongest SSW on record so far developed [Labitzke and Kunze, 2009], in contrast to the predicted undisturbed winter. SSWs are therefore subject of ongoing research (Chap. 1).

#### **2.2.4 Influence of the middle atmosphere dynamics on tracer distributions**

The impact of the middle atmosphere dynamics including advection, mixing, and transport barriers, which has already been discussed with respect to the polar region (Sect. 2.2.3), is here briefly extended to the whole middle atmosphere according to the description in Holton and Alexander [2000]. Due to the strong zonal winds in the middle atmosphere, trace gases are quickly zonally distributed and the discussion of their distribution is usually reduced onto a meridional plane. To understand the general meridional tracer distribution it is again necessary to consider the two major effects of wave breaking (Sect. 2.2.2). First, wave breaking drives the meridional circulation and thus leads to advective transport of trace gases. Second, wave breaking introduces turbulent mixing,

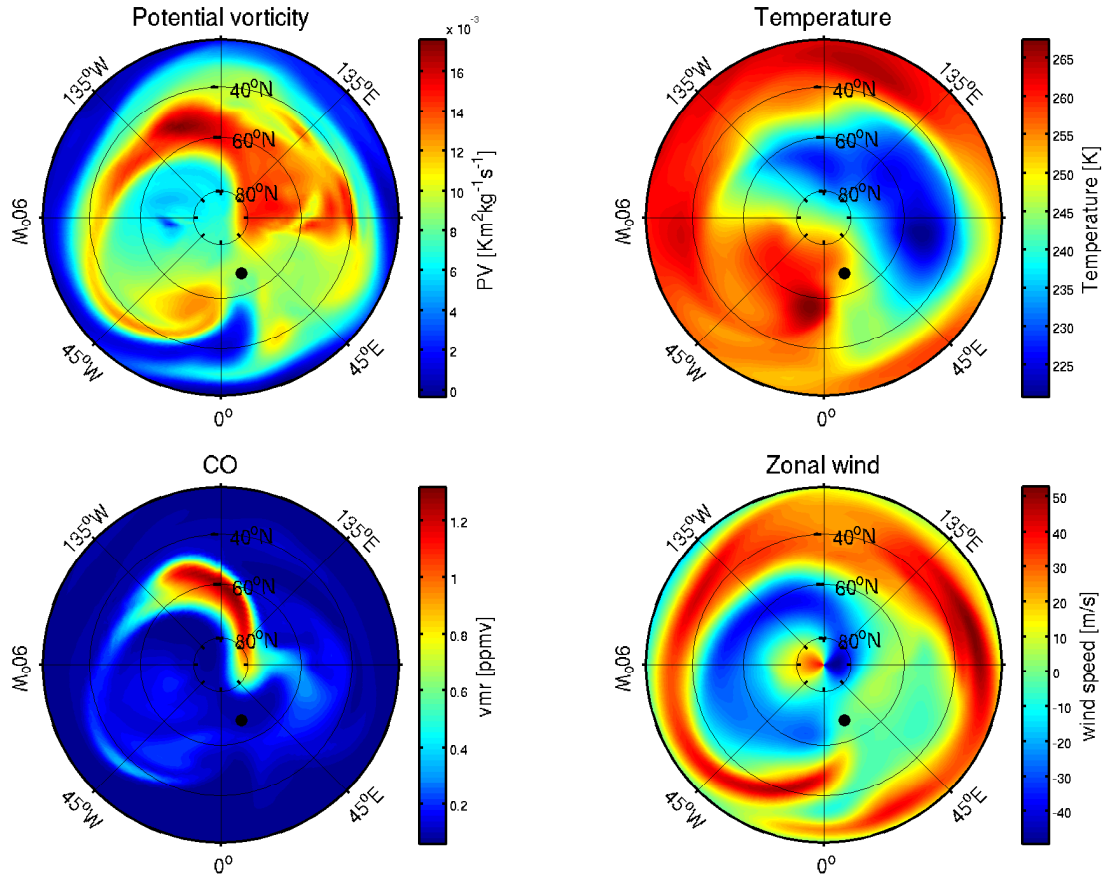


Figure 2.5: This figure is analog to Fig. 2.4, but for 2 February 2010, showing the disturbances caused by an SSW. The zonal wind is reversed (blue structure in bottom, right panel) and the former vortex air (high PV, and high CO) exhibits an extremely irregular shape; it is partly found far away from the pole (down to about  $40^\circ\text{N}$ ). Note that the color scales have changed compared to Fig. 2.4. Note further that the temperature increase associated with the SSW has to be seen relative to the state a few days before the SSW and can therefore not be identified from a comparison with Fig. 2.4.

which tends to equalize differences of trace gas distributions. The latter allows for the fact that the isopleths of a tracer in a well mixed region, such as the surf-zone, are close to horizontal in an annual mean, which is the result of a balance between photochemical destruction and the redistribution by turbulent mixing. Strong gradients of tracer abundances are, contrarily, expected in the vicinity of mixing barriers. Both types of region are indicated in Fig. 2.3 with heavy or light orange arrows, respectively.

As regards a long-lived tracer (Sect. 2.1.5), the isopleth are close to horizontal in the mid-latitudes, where the strong mixing occurs. In the polar winter region, however, they are shifted to lower altitudes due to the descent of air above the high latitudes and the transport barrier associated with the polar vortex. Accordingly, the isopleths are shifted to higher altitudes in regions with ascending air, especially in the polar summer mesosphere. This is exemplified for the tracer used in this study, CO, in Fig. 2.6.

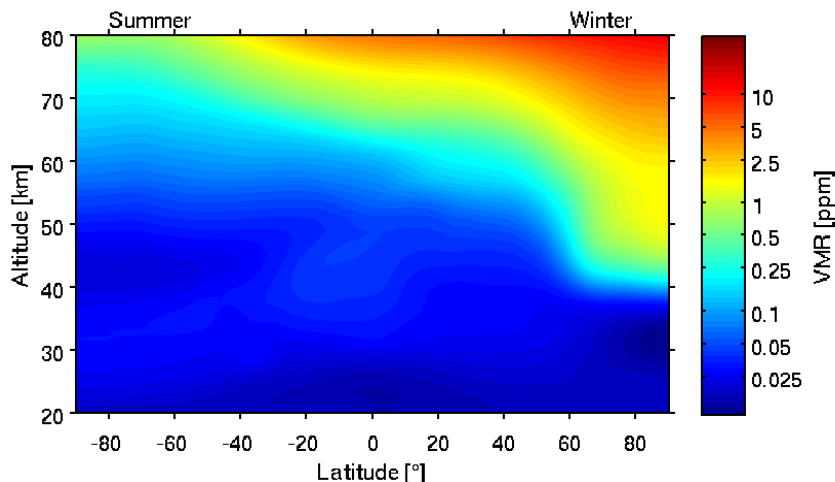


Figure 2.6: Zonally and monthly averaged CO vmr in the meridional plane for December 2009, illustrating the influence of the middle atmosphere dynamics on the distribution of long-lived tracers; the CO vmr contours are clearly shifted to lower altitudes in the polar winter region. This region is closed by a strong horizontal CO gradient (e.g., at 50 km altitude), which marks the polar transport barrier. The contours are much more flat in the well-mixed mid-latitudes and shifted to higher altitudes in the polar summer mesosphere. Data are taken from an SD-WACCM4 simulation.

### 2.2.5 Residual circulation and TEM formalism

The main ideas of the Transformed Eulerian-mean (TEM) formalism, a powerful framework for the mathematical description of the middle atmosphere meridional circulation, are sketched here. An introduction to this theory is given by Holton [2004] and Brasseur and Solomon [2005], whereas an extensive description is found in Andrews et al. [1987].

Many properties of the middle atmosphere are studied successfully in a two-dimensional meridional plane, thus in a zonal mean sense. As seen before for tracer distributions (Sect. 2.2.4), this simplification is facilitated by the strong zonal winds. Nevertheless, recalling the importance of wave disturbances, it is obvious that the resulting deviations from the zonal mean, the ‘eddies’, may not be neglected in an appropriate description. Hence, all relevant quantities (here once denoted arbitrarily as  $x$ ) are split into two parts each, the first part representing the zonal mean (denoted with an overbar) and the second part representing the eddy (denoted with a prime),

$$x(\lambda, \phi, z, t) = \bar{x}(\phi, z, t) + x'(\lambda, \phi, z, t), \quad (2.6)$$

with the zonal mean being a standard Eulerian mean over all longitudes  $\lambda$ .

However, it turns out that a mathematical framework based directly on these Eulerian means is not appropriate to describe the transport by the wave-driven meridional circulation. Instead, it leads to a ‘nontransport’ paradox [Sect. 12.2.1 in Holton, 2004]; the zonal mean vertical wind,  $\bar{w}$ , is found to be nonzero for the case of adiabatic, stationary, large-scale waves. This is, contrarily, exactly a case for which no real vertical transport across isentropes can occur. This paradox is resolved by the fact that the adiabatic contributions

to this zonal mean wind  $\bar{w}$  are canceled by the eddy heat fluxes, which is not obvious from the perspective of an Eulerian mean. Only the comparatively small fraction of diabatic heating due to the irreversible breaking of waves leads to a net vertical transport across isentropes. Hence, a representation of the transport by the zonal mean meridional circulation is sought, which is restricted to the residual effects of diabatic heating, thus represents the net transport across isentropes.

Such a representation is found with the definition of the TEM winds  $\bar{v}^*$  and  $\bar{w}^*$  [Andrews et al., 1987], which explicitly accounts for the eddy heat flux  $\overline{v'\theta'}$ , or more precise for its divergence. This definition is stated here in spherical coordinates in the horizontal, as well as log-pressure coordinates in the vertical:

$$\bar{v}^* = \bar{v} - \rho_0^{-1} \frac{\partial}{\partial z} \left( \rho_0 \frac{\overline{v'\theta'}}{\frac{\partial \theta}{\partial z}} \right) \quad (2.7)$$

$$\bar{w}^* = \bar{w} + \frac{1}{r \cos \phi} \frac{\partial}{\partial \phi} \left( \cos \phi \frac{\overline{v'\theta'}}{\frac{\partial \theta}{\partial z}} \right). \quad (2.8)$$

These meridional and vertical winds (with the TEM zonal wind set to zero) define the residual mean meridional circulation, which directly represents the net mean meridional mass flow associated with diabatic processes [Holton, 2004].

For the application within the scope of this work, the pure definitions (Eqs. 2.7 and 2.8) of the TEM winds are the major point since these equations can be used to calculate the residual circulation from given meteorological fields as, e.g., model data. A major general application of the TEM theory is, however, the mathematical derivation and explanation of the nature of the meridional circulation as a wave-driven system. Therefore, a few major points of the theoretical derivation are sketched here, although this is strictly not necessary at this point; Andrews et al. [1987] is recommended for a detailed description.

The ‘primitive equations’ (the zonal and meridional momentum balance, the vertical hydrostatic balance, the continuity equation, and the thermodynamic relation of diabatic heating and the change of potential temperature), which represent the basic description of the atmospheric circulation, are transformed into the zonal mean TEM formalism as starting point. Here, only the zonal momentum balance is important, which is further simplified by using local Cartesian coordinates in the horizontal, applying a quasi-geostrophic approximation, and neglecting frictional forces:

$$\frac{\partial \bar{u}}{\partial t} - f \bar{v}^* = \rho_0^{-1} \nabla \cdot \mathbf{F}_{\text{EP}}. \quad (2.9)$$

The vector  $\mathbf{F}_{\text{EP}}$  is the ‘Eliassen-Palm flux’, defined in the meridional plane. Its divergence is with the same simplifications and only considering Rossby waves given by

$$\nabla \cdot \mathbf{F}_{\text{EP}} = -\frac{\partial}{\partial y} (\rho_0 \overline{v'u'}) + \frac{\partial}{\partial z} \left( \rho_0 f \frac{\overline{v'\theta'}}{\frac{\partial \theta}{\partial z}} \right), \quad (2.10)$$

thus it contains the eddy heat flux  $\overline{v'\theta'}$  and the eddy momentum flux  $\overline{v'u'}$ . The Eliassen-Palm flux is therefore the generalized influence of the eddy-forcing; it is the link between

the theory of breaking waves, which has to provide an appropriate formulation of the eddy-terms incorporated in  $\mathbf{F}_{\text{EP}}$  (so that Eq. (2.10) only serves as example), and the reaction of the mean circulation to this eddy forcing, which is given by Eq. (2.9). This reaction becomes very clear in this simplified case if one further assumes a steady-state atmosphere without seasonal cycle ( $\frac{\partial \bar{u}}{\partial t} = 0$ ) representing near solstice conditions, so that Eq. (2.9) becomes

$$-f\bar{v}^* = \rho_0^{-1} \nabla \cdot \mathbf{F}_{\text{EP}}. \quad (2.11)$$

For non-equatorial regions, this is the mathematical formulation of the statement made above (Sects. 2.2.1.2 and 2.2.2) that the meridional circulation only exists (i.e.,  $\bar{v}^*$  is nonzero) if a forcing due to wave breaking exists (i.e.,  $\nabla \cdot \mathbf{F}_{\text{EP}}$  is nonzero). Another interesting result, an expression for  $\bar{w}^*$ , can be derived starting from Eq. (2.11) and using the TEM continuity equation (Sect. 2.2.6, Eq. 2.15) as well as appropriate boundary conditions:

$$\bar{w}^*(z) = -\rho_0^{-1} \frac{\partial}{\partial y} \left[ \frac{1}{f} \int_z^\infty \nabla \cdot \mathbf{F}_{\text{EP}} dz' \right] \quad (2.12)$$

This ‘downward control principle’ (Haynes et al. [1991], here adopted from Holton [2004]) states that the vertical velocity  $\bar{w}^*$  at a given altitude  $z$  is determined only by wave breaking above this altitude. More general, the transport by the residual circulation at a certain level is given by the force exerted by wave dissipation above this level [Brasseur and Solomon, 2005].

Due to the strong simplifications, these results serve only as rough idea of the causes of the wave-driven circulation. Inclusion of the other primitive equations is essential and allows further insights in, e.g., the temperature distribution in the middle atmosphere. And, of course, a higher level of complexity is necessary to produce results which are comparable to the real atmosphere. In this context, it is interesting to note that the quantity representing the eddies,  $\mathbf{F}_{\text{EP}}$ , depends in general also on the mean flow, introducing the mentioned complex wave-mean flow feedbacks.

## 2.2.6 Continuity equation

For fluids, the basic principle of the conservation of mass is expressed with the continuity equation. Therefore, the continuity equation is usually formulated for the mass density  $\rho$ . It can, however, be converted to be applicable to the number density or the vmr  $\chi$  of certain species [appendix 10A in Andrews et al., 1987]. The latter is used to describe temporal changes of atmospheric trace constituents and has generally the form

$$\frac{d\chi}{dt} = S + D_{\text{ur}}. \quad (2.13)$$

$S$  is the net chemical production term, thus the difference between chemical production and loss. The term  $D_{\text{ur}}$ , which is often neglected, represents changes by turbulent diffusion that are unresolved (‘ur’) [Andrews et al., 1987]. For an actual application, this equation has to be expressed in appropriate coordinates. Using Cartesian coordinates, the well known form of the continuity equation is obtained,

$$\frac{\partial \chi}{\partial t} + u \frac{\partial \chi}{\partial x} + v \frac{\partial \chi}{\partial y} + w \frac{\partial \chi}{\partial z} = S + D_{\text{ur}}. \quad (2.14)$$

Commonly, a scale analysis of the individual terms is performed, which may reveal that certain terms of the continuity equation can be neglected for a specific application.

Furthermore, the zonal mean continuity equation for the meridional plane, formulated in the TEM formalism (Sect. 2.2.5), is given by [Andrews et al., 1987]

$$\frac{\partial \bar{\chi}}{\partial t} + \bar{v}^* \frac{\partial \bar{\chi}}{\partial y} + \bar{w}^* \frac{\partial \bar{\chi}}{\partial z} = \bar{S} + \rho_0^{-1} \nabla \cdot \mathbf{M} \quad (2.15)$$

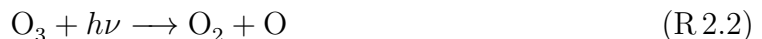
in log-pressure coordinates and without explicit consideration of unresolved effects. The quantity  $\mathbf{M}$  is the TEM eddy flux vector that considers the vmr eddy disturbances  $\chi'$  and is explicitly defined in the appendix 9A of Andrews et al. [1987].

## 2.3 A brief description of the polar ozone layer

The ozone layer is not directly in the focus of this work. However, it is one of the major atmospheric components of the climate system. Furthermore, the variability of the polar ozone layer highly depends on the dynamical variability. The general relevance of the polar ozone variability is therefore an indirect, though important, motivation for the present thesis, so that the main aspects of polar ozone will be summarized here briefly.

### 2.3.1 Basic ozone chemistry

The pure existence of the ozone layer is generally explained by the ‘Chapman cycle’ [Chapman, 1930], in which only oxygen species, as well as solar radiation and collision partners are considered. Molecular oxygen is converted to ozone and the other way around by basically the following two reactions (see, e.g., Brasseur and Solomon [2005] for details)



with  $h\nu$  denoting sunlight in the UV region. The initially necessary atomic oxygen O is produced by the photolysis of  $\text{O}_2$ . This cycle, in which the ozone is continuously destroyed and reproduced, leads to a stable state constituting the ozone layer. After the stable state has been reached, this cycle converts effectively only solar UV radiation to kinetic energy of the collision partners M, thus heats the stratosphere.

For a detailed quantitative understanding of the global distribution of ozone, it is necessary to consider the varying availability of sunlight, as well as the transport of ozone with the meridional circulation (Sect. 2.2.1.2) in the middle atmosphere. It turns out that the largest partial columns of ozone are found between 10 km and 35 km altitude, whereas the largest vmr of ozone is found between 30 km and 40 km.

Quantitative analyses show, furthermore, that the Chapman cycle alone would lead to ozone abundances that are higher than observed. This is resolved by the consideration of additional ozone loss reactions based on catalytic chemistry. A bunch of catalysts and respective reaction chains were found during the second half of the 20th century, among

them the  $\text{NO}_x$ ,  $\text{HO}_x$ ,  $\text{ClO}_x$ , and  $\text{BrO}_x$  cycles<sup>3</sup> (see, e.g., Lary [1997] or Brasseur and Solomon [2005] for a review of these reactions). The efficiencies of the individual loss reactions depend on altitude among others. Roughly,  $\text{NO}_x$  reactions are effective between 35 km and 45 km altitude and  $\text{HO}_x$  above 40 km altitude. Catalytic reactions involving  $\text{ClO}_x$  and  $\text{BrO}_x$  could generally be efficient in the lower stratosphere, where the major part of the ozone column is located. However, these catalysts are mostly unavailable, since they are bound in slowly reacting reservoir gases like  $\text{HCl}$  and  $\text{ClONO}_2$  and can only be released under special conditions, as will be described in the following (Sect. 2.3.2).

### 2.3.2 Polar ozone depletion

A special group of chemical reactions occurs only on the surface of solid particles like water ice. To this group belong reactions that can convert the reservoir gases into precursors of catalysts for ozone depletion. The probably most important reaction among them releases chlorine [e.g. Schoeberl and Hartmann, 1991]



Due to its dryness, the required ice particles are usually rare in most regions of the stratosphere. However, the separated air within the polar vortex cools radiatively during the course of the winter (Sect. 2.2.3), so that temperatures within the polar vortex can be low enough to form clouds of either nitric acid trihydrate (NAT) (freezing point 196 K) or water ice (189 K). These clouds are generally referred to as polar stratospheric clouds (PSCs).

This together with the anthropogenic emissions of Chlorofluorocarbons (CFCs) explains the appearance of the Antarctic ozone hole since the 1970s (discovered by Farman et al. [1985]) and the Arctic ozone depletion since a few years later [e.g., Solomon et al., 1988; Salawitch et al., 1993; Newman et al., 1997] in the respective spring. Due to the anthropogenic emissions of CFCs, the air is enriched with reservoir gases. Furthermore, the vortex air is cold enough to form PSCs. Thus, the reservoir gases are converted to  $\text{Cl}_2$  on the PSC surfaces. As soon as the sunlight returns in spring, the  $\text{Cl}_2$  is photolyzed and becomes active in ozone depletion, leading to the rapid spring ozone destruction.

### 2.3.3 Importance of the dynamical variability for polar ozone

As major precondition for polar ozone loss in spring, the temperatures within the polar vortex need to be sufficiently low during winter (Sect. 2.3.2). The inner-vortex temperature itself depends strongly on the persistence of the vortex mixing barrier. However, the vortex exhibits a strong variability (Sect. 2.2.3.3), particularly in the NH. This dynamical variability therefore causes a temperature variability, which, in turn, results in a strong ozone variability, depending on whether the temperature has fallen below the thresholds for the formation of PSCs or not.

---

<sup>3</sup>This notation refers to the reactive nitrogen oxide family: nitrogen molecules (in this case  $\text{NO}$  and  $\text{NO}_2$ ), which are rapidly converted into each other, so that they do not have to be treated separately for many applications; the same applies for the other families mentioned in the text; exact definitions can be found in Brasseur and Solomon [2005].

A measure which can be seen as a quantitative link between dynamical variability and ozone loss is the volume of potential PSC formation in the polar vortex,  $V_{\text{PSC}}$ , averaged over the period from mid-December to March [Rex et al., 2004, 2002]. Large ozone loss may be expected when  $V_{\text{PSC}}$  is large (mostly corresponding to a large base area of the polar vortex) and when this volume persists continuously from winter well into spring. Additional factors are the strength of the mixing barrier, the vertical position of  $V_{\text{PSC}}$  relative to the vertical ozone maximum, as well as the horizontal position of the polar vortex, i.e., whether it is located completely within the polar night region or displaced from the pole, so that parts of the air are illuminated.

All these aspects are influenced by the polar dynamical variability. Manney et al. [2011] showed recently that the largest NH ozone loss on record in the Arctic spring 2011 was a result of the fact that all these factors jointly favored ozone loss for the first time. Due to the variable Arctic dynamics, only some of these factors work usually toward strong ozone depletion, whereas the others do not, so that ozone depletion is commonly moderate in the NH. This is different in the SH, where wave activity is weaker, leading to a persistent and strong polar vortex. Ozone depletion is therefore much more pronounced in the SH, giving rise to the use of the term ‘ozone hole’ in the SH.

Dynamical variability does not only influence polar ozone indirectly via the vortex temperature. It has also a direct influence by the transport of ozone; either via meridional mixing across the vortex edge or via the downward transport of ozone-rich air with the descending branch of the residual circulation above the poles [Tegtmeier et al., 2008b]. The latter acts as an ozone supply for the lower stratosphere and is able to mask up to 35 % of the chemical ozone loss in the Arctic [Manney et al., 1995]. It is therefore important to separate dynamical and chemical contributions to the ozone variability to understand the full impact of the anthropogenic chemistry changes. Also other trace species influencing ozone are transported with the descending air (Sect. 2.3.4) and additionally, the descent of air has also an influence on the vortex temperature via adiabatic heating. Therefore, the descent of air from the upper stratosphere and mesosphere into the lower stratosphere above the high latitudes is of particular interest.

### 2.3.4 Effects of energetic particle precipitation

The upper and middle atmosphere are influenced by energetic particle precipitation (EPP), which refers mainly to electrons and protons that reach the atmosphere coming from the sun or from space. The penetration depth of these particles into the atmosphere is mainly determined by their energy and mass; most of the particles that belong to the background flux, which routinely reaches the atmosphere, are absorbed in the MLT region, where they modify the chemistry. Solomon et al. [1982] examined first the effect for the middle atmosphere, showing that the dissociation of  $\text{N}_2$  by EPP in the MLT region results in production of  $\text{NO}_x$ , among others. This  $\text{NO}_x$  can be transported into the stratosphere via the descending branch of the residual circulation above the polar winter region. Solomon et al. [1982] state that  $\text{NO}_x$  generated by EPP in the thermosphere can indeed be a significant source of  $\text{NO}_x$  in the stratosphere. This effect on the middle atmosphere is referred to as the ‘indirect EPP effect’. A ‘direct EPP effect’ is also known, which does not depend on the transport of  $\text{NO}_x$  generated by EPP, so that it is mentioned here only for completeness. It refers to sporadic events during which particles with even higher

energies are able to penetrate directly into the stratosphere, thus form  $\text{NO}_x$  directly where it is active as a catalyst.

The strength of the indirect EPP effect is also subject to interannual variability. In the stable SH polar vortex, the amount of  $\text{NO}_x$  reaching the stratosphere is dominated by the source strength in the MLT region [Randall et al., 2007a]. Contrarily, the variability of the transport of  $\text{NO}_x$ , i.e., the variability of the descent of air above the pole, has a significant influence in the NH. Randall et al. [2006], for example, present data showing that Arctic upper stratospheric  $\text{NO}_x$  was enhanced by a factor of 3 to 6 in spring 2006, whereas the  $\text{NO}_x$  production in the MLT region was not enhanced. This is explained with particularly strong descent in an unusually strong upper polar vortex, thus with a feature of dynamical variability.

As mentioned before,  $\text{NO}_x$  is a catalyst for ozone destruction in the stratosphere and thus the indirect EPP effect is an additional source of ozone variability. Randall et al. [2005, 2009] have shown that an ozone destruction of up to 60 % in the upper stratosphere can be caused by the indirect EPP effect if the descent is strong and persistent. The other way around, significant effects on ozone are expected if the  $\text{NO}_x$  is able to descend down to the region in which it is mostly effective as catalyst (below 45 km; Sect. 2.3.1). An example for extraordinary strong  $\text{NO}_x$  descent without a significant influence on ozone is apparent after the already mentioned strong SSW 2009 (Sect. 2.2.3.4). This event was followed by a strong descent transporting  $\text{NO}_x$ . However, this condition persisted not long enough to transport the  $\text{NO}_x$  down to altitudes low enough to have significant influence on ozone [Randall et al., 2009].

Note that the influence of the indirect EPP effect is usually limited to the upper and middle stratosphere, hence does not strongly affect the total column of ozone. The mentioned 60 % depletion in the upper stratosphere should therefore not be confused with something like an ‘ozone hole introduced by EPP’ since it only corresponds to a few percent of the total ozone column. In fact, the main interest in ozone changes induced by the indirect EPP effect arises from their impact on the stratospheric heat budget, which in turn causes feedbacks on the middle atmosphere dynamics. These impacts are not well understood yet, but a modeling study by Rozanov et al. [2005] shows that ozone loss due to the indirect EPP effect can lead to cooling of 2 K in the high latitude middle stratosphere. Furthermore, it may indirectly even cause detectable changes in the surface air temperature. The latter is also supported by analyses of meteorological data presented by Seppälä et al. [2009]. The authors point out that the physical mechanism behind this coupling is unclear but likely complex.

## 2.4 CO in the middle atmosphere

CO is the key species in this study. However, the main interest is not the abundance of CO itself, but the utilization of CO as tracer for the middle atmosphere dynamics in the polar winter. The foundation for this application is laid in this section.

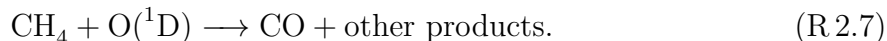
### 2.4.1 Chemistry of CO in the middle atmosphere

CO is in the middle atmosphere largely inert with respect to other constituents so that the involved chemistry is comparatively simple [Solomon et al., 1985]. This is in contrast to the troposphere, where CO is a pollutant and plays a major role in photochemical smog reactions. Early studies on CO in the middle atmosphere established the connection between CO and CO<sub>2</sub> [Hays and Olivero, 1970], as well as CH<sub>4</sub> [Wofsy et al., 1972]. Here, the chemistry of CO in the middle atmosphere is summarized according to Solomon et al. [1985], Brasseur and Solomon [2005], and Minschwaner et al. [2010].

The major source of CO for the middle atmosphere is the photolysis of CO<sub>2</sub>



The absorption of CO<sub>2</sub> is strongest in the Schumann-Runge continuum and at the Lyman- $\alpha$  wavelengths. Light of these wavelengths is mainly available at higher altitudes and causes the photolysis reaction to occur mainly in the MLT region. In the stratosphere and mesosphere, CO is also one of the end products of the oxidation of methane. This process includes several subreactions and is started with either OH, Cl or O(<sup>1</sup>D)



Above 120 km altitude, ion chemistry becomes relevant for CO, where it is produced by the oxidation of CO<sub>2</sub> with O<sup>+</sup> [Solomon et al., 1985]. Furthermore, a minor fraction of tropospheric CO can be transported into the tropical lower stratosphere, where the CO abundance shows a tape recorder-like seasonal variation (The name refers to the water vapor tape recorder observed earlier [e.g., Mote et al., 1996], although the reason for the development of the signal is different) [Schoeberl et al., 2006]. However, this source is only relevant for the lower stratosphere and is mentioned here only for completeness.

The dominant loss process for CO in the middle atmosphere is a reaction with hydroxyl



Above 100 km altitude, however, a three body recombination is the major loss process



Here, only two of these reactions are of major importance, the production in the MLT region (R 2.4) and the destruction below (R 2.8). The interplay of both reactions explains roughly the general shape of the CO vmr profile, showing low values in the stratosphere and strongly increasing values toward the MLT region (Fig. 2.7). This shape, particularly the strong vertical gradient, is an important property qualifying CO as tracer (Sect. 2.4.2).

## 2.4.2 CO as a tracer for polar dynamics

### 2.4.2.1 Chemical timescales

To be suitable as a tracer, the chemical timescales of the respective species have to be comparable to the dynamical timescales (Sect. 2.1.5). Lifetimes of CO in the middle atmosphere were first estimated by Allen et al. [1981] using a one-dimensional model and later by Solomon et al. [1985] with a two-dimensional model, which laid the foundation for the usage of CO as a tracer. Recently, Minschwaner et al. [2010] presented a derivation of the chemical lifetimes of CO based on observations of the two satellite instruments MLS and ACE-FTS. They confirm that the chemical timescales in winter are longer than 30 d for about 50° latitude. No measurement-based estimation is, however, possible poleward from 50° latitude in the winter hemisphere due to a lack of sunlight. Nevertheless, chemical lifetimes are known to increase strongly toward the winter pole, which is a result of the polar night; both the production of CO (R 2.4) and the main destruction (R 2.8) depend on sunlight, which is obvious for the former, a photolysis reaction. The latter is also connected to photolysis, since the reactant OH is product of photolysis reactions and thus only available in sunlit conditions.

Consequently, the chemical lifetimes of CO in the polar region are much longer than 30 d during winter. The expected dynamical timescales are in the order of days to months (timescales of the dynamical variability in the polar vortex region discussed in Sect. 2.2.3.3), so that CO is well-suited as tracer in the polar region during winter. When the light comes back in polar spring, the chemical timescale may, however, be reduced below 20 d, so that the use of CO as a tracer has to be considered carefully for the spring season [Minschwaner et al., 2010].

### 2.4.2.2 Spatial gradients

The second basic property that qualifies a species for being used as a tracer is the existence of spatial gradients. The reason is recognizable in the continuity equation (Eq. 2.14), where the spatial gradients appear in the advection terms together with the winds; only the advection of species with spatial gradients leads to changes of the abundance at a given location.

CO exhibits a strong vertical gradient with low vmr in the stratosphere and high vmr in the MLT region (Fig. 2.7, Sect. 2.4.1). Therefore, CO is sensitive to vertical transport and is expected to be suitable to study the descent of mesospheric air within the polar vortex (Sect. 2.2.1.2).

Furthermore, CO exhibits strong horizontal gradients in the polar winter region. This is a result of the combination of the downward transport of CO-rich air into the polar vortex and the mixing barrier at the vortex boundary. The mixing barrier prevents the descended CO-rich air from being quickly mixed with CO-poor air from the mid-latitudes (Sect. 2.2.3). The horizontal CO gradient is therefore located close to the vortex boundary (Fig. 2.4). This makes CO sensitive to horizontal advection, particularly to displacements of the polar vortex. Unfortunately, the sensitivity to both horizontal and vertical dynamics complicates the extraction of purely vertical motions from CO measurements. It is elaborated on this issue extensively in Chap. 7.

### 2.4.2.3 Representation of dynamical features in CO time series

The knowledge of the CO properties is used to consider how the main features of the polar winter middle atmosphere dynamics (Sect. 2.2) will appear in a time series of CO vmr profiles measured at one particular location. Generally, all dynamical processes can only lead to an increase or a decrease of the CO vmr at a certain location and altitude.

Considering a measurement location that is certainly within the polar vortex, there is only one possibility how CO can be increased at a certain altitude. This is the downward transport of CO-rich air from above, thus the mentioned descent of air. However, having in mind that the Arctic polar vortex is commonly disturbed and has an irregular shape, there is a second possibility to increase CO above the measurement location: the crossing of the vortex boundary over the measurement location such that CO-poor mid-latitude air is measured before the crossing and inner-vortex CO-rich air afterwards. These events, if identified in the observations, could be used to precisely determine the vortex position, but they certainly complicate the investigation of the descent.

There are three possibilities to decrease CO at a certain position. First, again the crossing of the vortex boundary, but in the opposite direction, decreases CO. Second, ascending air would lead to a CO decrease within the vortex. However, ascent is not expected in polar winter dynamics, except during SSWs, where it is still uncertain. The third possibility, probably of major relevance, is inflow of CO-poor mid-latitude air into the polar vortex by mixing across a weakened transport barrier. Since this effect is controlled by wave influences, it is expected to produce a high variability on short time scales in the CO time series.

It was so far implicitly assumed that the inner-vortex air is homogeneous, which must not perfectly be the case, especially close to the vortex boundary. Due to the motion of the vortex, inhomogeneities would also produce CO variability above a certain location. This variability is, however, expected to be of smaller magnitude than the effects mentioned before since only comparatively slight deviations from homogeneity are expected.

It is obvious that the separation of the causes of individual variations seen in a CO dataset is a challenging task. It appears therefore comprehensible that although many publications highlight the potential of CO as a tracer (Sect. 2.4.3), it is mostly just used as rough qualitative indication for the existence of the descent of mesospheric air. In some studies, descent rates are additionally estimated from CO using a straightforward method described below (Sect. 2.4.2.4).

Nevertheless, three major features of the polar winter middle atmosphere dynamics are commonly obvious in CO time series (compare to the time series derived in this work: Sect. 4.4.2, Fig. 4.9). First, the descent of air in fall and winter. Second, SSWs in spring, which lead to a rapid decrease of CO in a large altitude range. This is either due to the breakdown of the mixing barrier or due to an ascent of air, which is currently debated. And third, the reversal of the circulation in spring, during which the vortex breaks down and mixing with mid-latitude air is possible in addition to the increasing effects of the returning sun.

#### 2.4.2.4 A heuristic method to derive polar descent rates

The common method for an estimation of the descent rates of mesospheric air based on a CO time series is straightforward. At least two CO profiles are chosen that were measured with a time difference  $\Delta t$ . A certain value of the CO vmr,  $\chi_{\text{CO}}$ , is chosen (Fig. 2.7, there 1.5 ppmv, marked with arrows) and the altitudes in which this value is found are determined for both profiles. The average descent rate, which corresponds to the average slope of the CO isoline, can be calculated from the altitude difference  $\Delta z$ ,

$$w_{\text{CO}} = \frac{\Delta z}{\Delta t} \Big|_{\chi_{\text{CO}}} \quad (2.16)$$

with  $w_{\text{CO}}$  denoting the estimate of the descent rate based on CO profiles and  $\Big|_{\chi_{\text{CO}}}$  denoting that the CO vmr,  $\chi_{\text{CO}}$ , was left constant. It is implicitly assumed for the application of this method that the only relevant process changing CO is actually the downward transport. The equality of  $w_{\text{CO}}$  and the vertical velocity,  $w$ , depends on the validity of this assumption. This is shown formally by making  $\Delta t$  infinitesimal and using the triple product rule<sup>4</sup> for partial derivatives

$$w_{\text{CO}} = \frac{\partial z}{\partial t} \Big|_{\chi_{\text{CO}}} = - \frac{\partial z}{\partial \chi_{\text{CO}}} \Big|_t \frac{\partial \chi_{\text{CO}}}{\partial t} \Big|_z \quad (2.17)$$

$$\Rightarrow \frac{\partial \chi_{\text{CO}}}{\partial t} + w_{\text{CO}} \frac{\partial \chi_{\text{CO}}}{\partial z} = 0. \quad (2.18)$$

The latter, Eq. (2.18), is exactly the continuity equation (Eq. 2.14) for CO, given that only the vertical advection term is relevant and the other terms are neglectable. Only if this is justified, the estimate  $w_{\text{CO}}$  is equal to the vertical wind  $w$  (The same applies in the zonal mean perspective using the TEM formalism (Sect. 2.2.5) with  $\bar{\chi}_{\text{CO}}$ ,  $\bar{w}^*$  and the TEM continuity equation, Eq. 2.15). For the chemical source term  $S$ , the justification is mostly valid since the chemical lifetimes are sufficiently long (Sect. 2.4.2.1). Furthermore, the term of unresolved effects  $D_{\text{ur}}$  is usually considered to be neglectable. The neglectation of the horizontal advection terms, however, is questionable considering the possible CO variability introduced by the horizontal processes mentioned above. This will be further examined in Chapter 7.

### 2.4.3 Previous and ongoing CO observations in the middle atmosphere

Previously conducted and ongoing observations of middle atmosphere CO and their applications are briefly summarized in this section. In some of the studies, descent rates have been derived, as will be noted below. All these derivations of descent rates basically apply the method described before (Sect. 2.4.2.4).

The first detection of mesospheric CO was reported by Waters et al. [1976], who analyzed the absorption of solar radiation by the 115 GHz transition using ground-based

<sup>4</sup>For a function  $z(x, y)$  the triple product rule states that  $\frac{\partial x}{\partial y} \Big|_z \frac{\partial y}{\partial z} \Big|_x \frac{\partial z}{\partial x} \Big|_y = -1$ . It is also known as Euler's chain rule and is often used in thermodynamics.

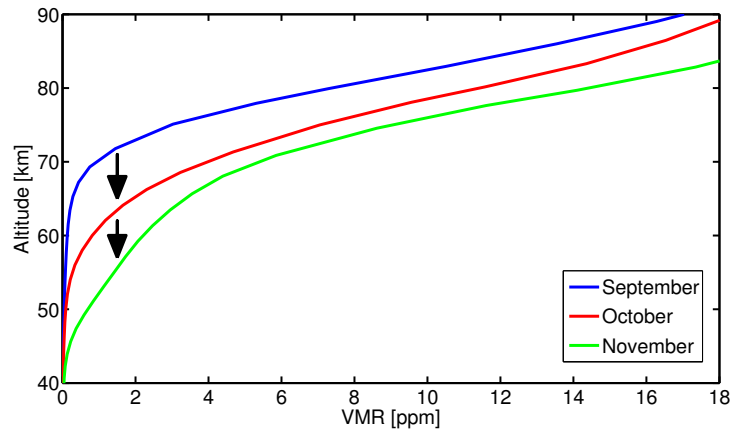


Figure 2.7: Monthly and zonally averaged CO profiles at 67°N latitude for three months in fall. First, the general shape of a common CO profile—with low values in the stratosphere and high values in the MLT region—is apparent in each example. Second, the application of CO as tracer for vertical motions is shown: the same CO vmr values are located at lower altitudes later in fall as it is indicated here for the 1.5 ppmv level with arrows. This is assumed to correspond to the descent of air during fall and winter in the Arctic polar vortex. The profiles were simulated with SD-WACCM4.

microwave radiometry. Goldsmith et al. [1979] extended this technique for measurements of the 230 GHz line. The detection of the thermal emission of CO, which is the approach that is mostly used in microwave remote sensing of CO today, was firstly reported by Künzi and Carlson [1982] for both lines (Fig. 2.8) and extended by Bevilacqua et al. [1985]. Furthermore, Clancy et al. [1982] detected mesospheric CO in absorption against the moon. These early studies were restricted to the measurement of some individual spectra. Nonetheless, they have proven the steep increase of the CO vmr in the mesosphere and have already indicated the high variability of CO in space and time. The first ground-based campaign of a few weeks duration was reported by Aellig et al. [1995]. They observed a seasonal change of CO as well as short-term variability, which was attributed to gravity wave breaking. More recently, Forkman et al. [2003] reported of continuous ground-based measurements in Onsala, Sweden (57.4° N), which were used for a model comparison. Furthermore, this dataset was used for a dynamical study in Forkman et al. [2005], in which descent rates of 300 m/d were calculated for fall; the authors state that CO is not significantly affected by other processes than vertical descent during this time. Moreover, campaigns performed in the Arctic (Thule, Greenland, 76.5° N) were reported by de Zafra and Muscari [2004] and Di Biagio et al. [2010]. The former study pronounces the complexity of the interpretation of CO data in terms of dynamics, whereas the latter presents descent rates of 200 m/d to 300 m/d after the SSW 2009 without elaborating on the applicability of the derivation method.

All previously mentioned studies employed ground-based microwave radiometry. Another ground-based observation technique, suitable for the measurement of middle atmospheric CO, is Fourier transform infrared spectroscopy (FTIR). The advantage of FTIR is that many trace gases are observed routinely at the same time and are analyzed later

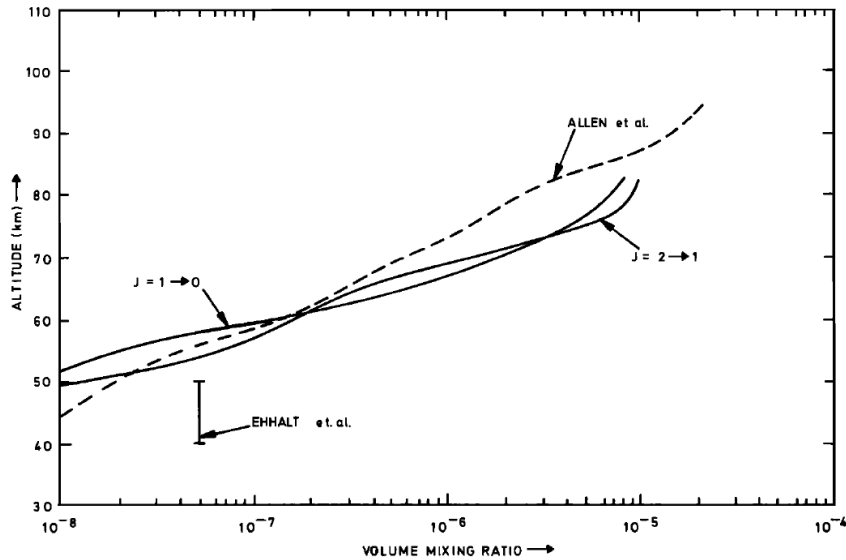


Figure 2.8: The first CO profiles obtained from ground-based microwave measurements of thermal emission lines for the 115 GHz transition ( $J = 1 \rightarrow 0$ ) and the 230 GHz transition ( $J = 2 \rightarrow 1$ ) presented by Künzi and Carlson [1982]. Furthermore, a modeled profile by Allen et al. [1981], as well as an in situ measurement by Ehhalt et al. [1975] are included. Figure adopted from Künzi and Carlson [1982].

application-oriented. Therefore, longterm time series of spectra including CO lines already exist and are continuously extended, so that they just have to be analyzed with respect to CO. Disadvantages are, first, the dependence on direct sunlight, so that the time series are irregular in time and the polar winter cannot be observed. Second, it is only possible to derive stratospheric partial columns. Kasai et al. [2005] presented the first CO columns derived from FTIR spectra, using data from an Arctic station (Poker Flat, Alaska,  $65^\circ$  N). Velasco et al. [2007] transferred this technique to data from different stations in Antarctica, the Arctic, and the mid-latitudes. Recently, time series of mid-latitude CO were presented by Borsdorff and Sussmann [2009].

Whereas all these ground-based measurements are limited to their particular measurement location, space-borne instruments allow for a horizontally resolved view. Therefore, the development of these instruments strongly improved the applicability of CO as tracer since the horizontal gradients became directly observable. However, although providing a nearly global picture, the data at one particular location are more sparse than for ground-based measurements. Furthermore, the lifetime of satellites is limited, whereas ground-based instruments can be operated for much longer periods, so that ground-based data have to be used to intercalibrate between several satellite generations. The first global determination of CO from space was performed by the instrument ISAMS on UARS [López-Valverde et al., 1996]. These data were used by Allen et al. [1999] to study Arctic dynamics and Allen et al. [2000] for dynamics in Antarctica. The latter includes the derivation of Antarctic descent rates of 250 m/d to 330 m/d. After ISAMS ceased operation in 1992, there were no satellite observations of CO in the middle atmosphere until the latest generation of satellite instruments was launched between 2001 and 2004.

In the meantime, a few measurement campaigns were conducted during Space Shuttle missions [Rinsland et al., 1999; Grossmann et al., 2006].

The first satellite instrument of the new generation was the Sub-Millimeter Radiometer (SMR) on ODIN, launched in 2001. CO data were presented in Dupuy et al. [2004] and used for intercomparisons with the instruments, which are introduced in the following. Although this instrument is still in operation, there are no CO observations available for the period of interest in the present study [personal communication with Joachim Urban (Chalmers University of Technology, Gothenburg, Sweden) at MIPAS data user meeting, 12-13 Mai 2011, Granada, Spain]. One year later, the Michelson Interferometer for Passive Atmospheric Sounding (MIPAS) on Envisat was launched. MIPAS works in different measurement modes with the following three being in principle relevant for the present work: MIPAS nominal mode (MIPAS NOM), MIPAS middle atmosphere mode (MIPAS MA), and MIPAS upper atmosphere mode (MIPAS UA), which differ in the covered altitude range and the frequency in which measurements are performed. CO data of the MIPAS NOM mode have been presented by Funke et al. [2009]. Descent rates of 350 m/d to 400 m/d have been derived for the fall descent in this study. After the SSW 2004, descent rates of 1200 m/d have been found. Measurements of the other two modes have not been published so far, but MIPAS MA observations have been made available for the present work. The next satellite instrument launched in 2003 was the Atmospheric Chemistry Experiment – Fourier Transform Spectrometer (ACE-FTS). The respective CO product was validated by Clerbaux et al. [2008] and then used in numerous publications. The last satellite instrument launched so far, measuring middle atmosphere CO, was the Microwave Limb Sounder (MLS) on Aura in 2004, which provides by far the largest number of measurements and was used in many studies based on the validation presented in Pumphrey et al. [2007]. Measurements of the latter three instruments, which currently provide CO data, MIPAS, ACE-FTS, and MLS, are incorporated in this study and will be described in more detail below (Sect. 5.2).



# 3 Microwave radiometry

The remote sensing technique used in this study, the ‘microwave<sup>1</sup> radiometry’, is based on the detection and, in most cases, the spectral decomposition of microwave radiation. In the present case, thermal radiation emitted by the atmospheric trace gas CO is received. One major advantage of this technique is the independence from sunlight, which makes it particularly suitable for observations during polar night. This chapter reviews the basic underlying principles; in particular, origin and transfer of the microwave radiation in the atmosphere, its detection, and the analysis of the obtained microwave spectra using inversion theory.

## 3.1 Microwave radiation in the atmosphere

### 3.1.1 Radiative transfer

The radiative transfer theory generally describes the propagation of radiation through any kind of media in which radiation is emitted, absorbed or scattered. Here, the main aspects of the theory are summarized specifically for the case of microwave radiation in the atmosphere according to Janssen [1993].

The major simplification in the microwave case is that scattering can be neglected, thus only emission and absorption are considered. However, the errors made by the neglect of scattering depend on the observation frequency and the size of the water droplets in the atmosphere. Whereas clouds can be neglected for frequencies up to approximately 300 GHz, rain can only be neglected up to 100 GHz [Janssen, 1993]. The spectral region of interest for this work is at 230 GHz, so that measurements are generally not performed during rainy and wet weather conditions. In turn, the spectra are obtained only during dry periods, so that the neglect of scattering is assumed to produce no significant error.

The frequency of the observed radiation is denoted with  $\nu$  in the following. Furthermore, the speed of light  $c$ , Planck’s constant  $h$ , and Boltzmann’s constant  $k_B$  are used.

#### 3.1.1.1 Transfer equation

The radiative transfer is expressed by the change of the specific intensity  $I_\nu$  along the light path in the atmosphere. The strength of local intensity loss by absorption is characterized by the absorption coefficient  $\alpha$ . Also a local intensity gain through emission can be expressed by  $\alpha$  assuming local thermodynamic equilibrium and using further Kirchhoff’s law and the Planck function  $B_\nu(T)$  at the local temperature  $T$ . This is put together in

---

<sup>1</sup>A more precise separation of the centimeter, millimeter, and submillimeter spectral regions is not applied here. Instead, the microwave region is used here as generic term following Janssen [1993].

the differential form of the transfer equation

$$\frac{dI_\nu}{ds} = -I_\nu\alpha + \alpha B_\nu(T), \quad (3.1)$$

where  $ds$  is a differential part of the light path. The first and second term on the right side are the loss and source terms, respectively.

### 3.1.1.2 Rayleigh-Jeans equivalent brightness temperature

The Planck function  $B_\nu(T)$ , which has the same units as the specific intensity  $I_\nu$ , can be inverted to provide a relation between temperature  $T$  and specific intensity  $I_\nu$ , which is nonlinear. For microwave remote sensing, however, the condition  $h\nu \ll k_B T$  for applying the Rayleigh-Jeans approximation to  $B_\nu(T)$ ,

$$B_\nu(T) \approx \frac{2\nu^2 k_B T}{c^2}, \quad (3.2)$$

is usually valid. This approximation is used for a linear transformation of the specific intensity to a quantity in temperature units, the ‘equivalent brightness temperature’  $T_b$

$$T_b(\nu) = \frac{c^2}{2\nu^2 k_B} I_\nu. \quad (3.3)$$

Microwave spectra are often given in units of the brightness temperature due to practical advantages in the calibration process.

### 3.1.1.3 Solution of the transfer equation

The transfer equation (Eq. 3.1) is a standard differential equation with a known solution, which is in brightness temperature units

$$T_b(\nu) = T_{b0} \exp^{-\tau(s_0)} + \int_0^{s_0} T(s) \exp^{-\tau(s)} \alpha ds \quad (3.4)$$

with  $s$  referring to the light path in the atmosphere. The receiver is considered to be located at  $s = 0$  and the light path is integrated up to a certain boundary  $s_0$ , where the intensity has a starting value equivalent to  $T_{b0}$ . The quantity  $\tau$  is the ‘optical depth’ defined as

$$\tau(s) = \int_0^s \alpha(s') ds'. \quad (3.5)$$

$T_b(\nu)$  in Eq. (3.4) is generally the mathematical representation of a microwave spectrum. Hence, it could in principle be used to calculate a spectrum for a known atmosphere, in particular for known temperature and absorption coefficient profiles along the line of sight. However, the goal of microwave radiometry is the opposite, namely the derivation of information on atmospheric properties from measured microwave spectra. Therefore, Eq. (3.4) has to be inverted, which is achieved by a numerical ‘retrieval’ process (Sect. 3.3). The desired information on trace gas abundances is thereby contained in the absorption coefficient  $\alpha$ , so that this quantity is discussed in more detail in the following (Sect. 3.1.2).

### 3.1.2 The absorption coefficient

The absorption coefficient  $\alpha_{\text{species}}$  for an individual species in the atmosphere can be written as follows [Janssen, 1993] (the dependence on the location  $s$  in the atmosphere is not explicitly expressed):

$$\alpha_{\text{species}}(\nu) = n \sum_{f,i} S_{fi}(T) F(\nu, \nu_{fi}). \quad (3.6)$$

The single parts of this equation directly reveal the different physical properties that constitute the absorption coefficient: the quantity  $n$  is the number density of the respective species and is therefore the key to the derivation of the species abundance profile. The sum runs over all possible transitions between excited states  $f$  and  $i$ , thus covers all the individual emission lines of the respective species.  $S_{fi}$  is the line intensity of a certain transition at a certain temperature. Finally,  $F(\nu, \nu_{fi})$  is the line shape function of a certain transition. It reflects that the emission lines are not ideal delta peaks at the transition frequency  $\nu_{fi}$  (more precisely: naturally broadened lines around  $\nu_{fi}$ ), but that the line intensity is distributed over a broader part of the spectrum by different processes as, e.g., interactions between the molecules in the air. This line broadening is the key for the retrieval of altitude resolved information from an emission line.

The terms of the absorption coefficient are explained in more detail following Janssen [1993] below.

The complete absorption coefficient is finally computed as the sum over the absorption coefficients of all relevant species and additional terms  $C$  representing the continuum absorption [Bühler et al., 2005]:

$$\alpha(\nu) = \sum_{\text{species}} \alpha_{\text{species}}(\nu) + \sum_{\text{cont. species}} C_{\text{cont. species}}(\nu) \quad (3.7)$$

#### 3.1.2.1 Rotational spectrum of CO

The theoretical derivation of a microwave spectrum for an isolated molecule is here directly adapted for the relatively simple case of CO, the species measured in this work. The starting point for this problem is the time-independent Schrödinger equation for the molecule's wave function  $\Psi$  with the Hamiltonian  $H$  and the energy level  $E$  of the wave function,  $H\Psi = E\Psi$ . Following the Born-Oppenheimer approximation, the problem can be split up into parts for electronic, vibrational and rotational transitions. Only the rotational transitions are relevant in the present case, so that applying only the rotational Hamiltonian is sufficient,

$$H_{\text{rot}} = \frac{P_x^2}{2I_x} + \frac{P_y^2}{2I_y} + \frac{P_z^2}{2I_z}, \quad (3.8)$$

with  $I_x$ ,  $I_y$ , and  $I_z$  denoting the moments of inertia along the principal axes of the molecule as well as  $P_x$ ,  $P_y$ , and  $P_z$  denoting the respective components of the angular momentum operator. Due to the symmetry of the CO molecule, two of the principal moments of inertia are considered to be equal (e.g.,  $I_x = I_y$  with  $z$  being the symmetry axis). Furthermore, the third principal moment of inertia approaches zero (here  $I_z \approx 0$ ) since CO has linear shape. The energy eigenvalues for such a problem are given by

$$E_{\text{rot}} = hBJ(J+1) \quad (3.9)$$

with the nonnegative integer quantum number  $J$  and the rotational constant  $B = \frac{h}{8\pi^2 I_x}$ . The frequencies of transitions between neighbor states are therefore

$$\nu_{J,J+1} = 2B(J+1), \quad (3.10)$$

so that the emission lines of CO are equally spaced with a distance of  $2B$  (115.3 GHz).

### 3.1.2.2 Line intensities

Although the line intensities  $S_{fi}$  are an important factor for the retrieval of trace species, it is not necessary to introduce the underlying theory here, since the used line intensities are taken as input values from a catalog based on measurements (Sect. 4.2.1). The only preprocessing done here is a scaling of the line intensities from the temperature at which the measurement was performed to the respective atmospheric temperature. The scaling approach is generally also described in Janssen [1993], the specific implementation used in this work is described in Bühler et al. [2005].

### 3.1.2.3 Line broadening

The rotational lines, derived above for CO, were so far considered to be delta peaks. In reality, however, the lines are broadened over a wider spectral area by different processes. The first broadening type, which can commonly be neglected in microwave radiometry, is the natural line broadening. It results directly from Heisenberg's uncertainty principle that relates the finite lifetime of an excited state to an uncertainty of the energy released during its decay. Relevant for atmospheric microwave remote sensing are two different broadening types, the 'thermal' or 'Doppler' broadening as well as the 'pressure' broadening.

The Doppler broadening originates from the translational motion of the molecules due to their temperature. This motion results in a Doppler-shift of the line frequency of each emitting molecule according to its velocity along the direction of the propagation of the electromagnetic wave. Doppler broadened lines are described with the Doppler line shape function [Janssen, 1993]

$$F_D(\nu, \nu_{fi}) = \pi^{-1/2} \beta_D^{-1} \exp \left[ - \left( \frac{\nu - \nu_{fi}}{\beta_D} \right)^2 \right] \quad (3.11)$$

with the Doppler broadening parameter

$$\beta_D = \sqrt{\frac{2k_B T}{m c^2}} \nu_{fi} \quad (3.12)$$

with the mass of the respective molecule  $m$ . The half width at half maximum (HWHM) of the Doppler broadened line is given by

$$\gamma_D = \sqrt{2 \ln 2} \beta_D. \quad (3.13)$$

The pressure broadening is generally caused by interactions of the molecules in a gas. The basic idea of this process is that collisions between molecules reduce the lifetime

of the excited states, which increases the energy uncertainty of the emitted radiation and therefore the linewidth. However, different kinds of interactions between the gas molecules exist, which cause different realizations of pressure broadening. Therefore, several approaches of the theoretical description including different approximations of pressure broadening are established. An overview is given by, e.g., Thorne [1974]. The representation of pressure broadening as a line shape function depends on the air density. For the relatively low density in the middle atmosphere, the line shape can be approximated by a Lorentz shape factor

$$F_L(\nu, \nu_{fi}) = \pi^{-1} \left( \frac{\nu}{\nu_{fi}} \right)^2 \frac{\gamma_c}{(\nu - \nu_{fi})^2 + \gamma_c^2} \quad (3.14)$$

with the ‘collisional half-width’  $\gamma_c$ . The collisional half-width is proportional to the number density of the air. Therefore, it is also related to air pressure and temperature, which is the key to the derivation of altitude resolved trace gas abundances. A simple expression for this relationship is given below using the air broadening parameter  $\gamma_a$ , which is derived empirically at the temperature  $T_{\gamma_a}$ , and its exponent  $n_a$ . These quantities are also taken from a catalog for the present purpose (Sect. 4.2.1).

$$\gamma_c = \gamma_a p \left( \frac{T_{\gamma_a}}{T} \right)^{n_a}. \quad (3.15)$$

A more sophisticated expression, considering also a self-broadening effect, is given by, e.g., Bühler et al. [2005].

Whereas the strength of the Doppler broadening is for a given frequency  $\nu_{fi}$  roughly constant with altitude, the strength of pressure broadening decreases exponentially with altitude. Both together leads to three distinct altitude regions: a region where pressure broadening dominates, a region of comparable strength of both effects and a region where the Doppler broadening dominates. As will be shown quantitatively below for the specific example of the CO line analyzed here (Sect. 4.2.5), the pressure broadening dominates generally in the stratosphere and the lower parts of the mesosphere. In the upper mesosphere, the Doppler broadening starts to dominate and no altitude information can be obtained anymore. In the limited region in between, where both effects are equally strong, the Voigt line shape function has to be applied, which is a convolution of  $F_D$  and  $F_L$ ,

$$F_V(\nu, \nu_{fi}) = \int_{-\infty}^{\infty} F_L(\nu, \nu') F_D(\nu', \nu_{fi}) d\nu'. \quad (3.16)$$

The HWHM of the Voigt line shape can be approximated using  $\beta_D$  and  $\gamma_c$  [Olivero and Longbothum, 1977]:

$$\gamma_v = 0.5346\gamma_c + \sqrt{0.2166\gamma_c^2 + \beta_D^2}. \quad (3.17)$$

## 3.2 Microwave radiometer

A microwave radiometer is the device for the measurement of the microwave spectra  $T_b(\nu)$  (Eq. 3.4), from which the vertical vmr profile of the respective species is extracted in the ‘retrieval’ process (Sect. 3.3). Since the present study is based on already obtained

spectra and starts with the latter, the analysis of these spectra, only the main aspects of the microwave radiometry technique are mentioned here. More details can be found in Janssen [1993] and Vowinkel [1988], which are also the basis for this section.

### 3.2.1 Requirements

The general aim of atmospheric microwave radiometry is the detection of atmospheric microwave emission and its spectral decomposition. For the latter, the atmospheric radiation has finally to be fed into a spectrometer, which transforms the incoming radiation to a digital spectrum that can be further processed. Different spectrometer techniques are commercially available. All these types have common limitations: they work only in a limited frequency range, the lower GHz range, and they have certain detection limits in terms of the incoming power. Both limitations constrain the incoming radiation that can be processed.

The other way around, the frequency and power of the atmospheric signal are also constrained by the emission process and the radiative transfer (Sect. 3.1); the emission frequencies are usually in the range of 20 GHz to 300 GHz, thus they are too high to be directly detected by a commercially available spectrometer. The power of the signal is often much lower than the detection limit of a spectrometer (about 8 orders of magnitude). In a microwave radiometer that incorporates a standard spectrometer, the atmospheric signal has therefore to be transformed first to match the spectrometer specifications. Overall, a microwave radiometer provides four major functionalities:

1. Receiving of the atmospheric microwave radiation in the respective frequency band. An antenna, which is usually a horn-antenna of an appropriate dimension, is specifically produced for this purpose in consideration of the signal frequency.
2. Transformation of the signal to a lower frequency. This is achieved by ‘mixing’ the signal frequency with a similar frequency produced by a local oscillator (LO). Commercially available special components, the ‘mixers’, generate the difference frequency from both superimposed frequencies, so that the signal is down-converted to any given frequency by choosing an appropriate LO frequency. Radiometers using this technique are called ‘superheterodyne’ receivers. The complete down-conversion is often split into two to three sub-steps, depending on the special application.
3. Amplification of the signal. Commercially available microwave amplifiers are used in several amplification stages. These stages are included in the individual frequency mixing steps and thus work at different frequencies. This avoids the problem of feedbacks which may appear when high amplifications are applied.
4. Detection and spectral decomposition of the transformed and amplified signal in a standard spectrometer.

Therefore, a radiometer basically consists of an antenna, followed by several mixing stages (each consisting of amplifiers, mixers and LOs, among others), and the spectrometer at the end. It cannot be avoided that these components create noise due to different processes and thus radiate themselves in the microwave region. The spectrometer detects

therefore the sum of the emissions by the atmosphere and by the instrument itself, whereby the instrument contributions usually even dominate. The measured quantity is therefore the ‘system temperature’  $T_{\text{sys}}(\nu)$

$$T_{\text{sys}}(\nu) = T_A(\nu) + T_{\text{rec}}(\nu). \quad (3.18)$$

$T_A$  denotes the ‘antenna temperature’, which measures the power entering the antenna from outside. It is basically equal to the sought atmospheric spectrum  $T_b(\nu)$  (Eq. 3.4) if the cosmic background radiation is neglected.  $T_{\text{rec}}$  is the ‘receiver temperature’, which measures the power that comes from the instrument itself. It corresponds to the temperature of a black body, which would generate the same power in the spectrometer if it had been placed in front of the antenna of an ideal, non-emitting, instrument.

The fact that the receiver contributes itself significantly to the measured signal demands for a facility to extract the atmospheric component. Furthermore, the spectrometer outputs the intensity of the spectrum usually in arbitrary units, so that it has to be calibrated to absolute units. Therefore the fifth main function of a microwave radiometer is

5. the calibration of the spectrum. This is done by the measurement of sources with a known spectrum. These sources are often black bodies with a known temperature, so that the spectrum is naturally calibrated to equivalent brightness temperature units (Eq. 3.3). Different calibration techniques are available and will be explained further in the following (Sect. 3.2.2).

## 3.2.2 Calibration

Due to the strong amplification of the atmospheric signal, only slight variations in the radiometer’s environment (lab temperature, power supply, etc.) are able to influence the measured spectrum by modifying the total amplification gain of the instrument. A radiometer has therefore not only to be calibrated once, but a calibration is usually only valid for periods in the order of minutes. Then a new calibration has to be performed. The two calibration techniques that are of relevance for this work are briefly discussed here. An extensive discussion of calibration issues in microwave radiometry can be found in, e.g., Krupa [1998].

### 3.2.2.1 Hot-cold calibration

It is often assumed that the receiver works linearly, which means that the system temperature  $T_{\text{sys}}(\nu)$  is related linearly to the uncalibrated ‘raw spectrum’  $M_{\text{atm}}(\nu)$  of an atmospheric measurement. In this case, two measurements of black bodies with different known temperatures are sufficient to establish this linear relationship, i.e., to calibrate the spectra. Usually, one black body at ambient temperature (‘hot’, index ‘h’) and one at the boiling point of liquid nitrogen at 77 K (‘cold’, index ‘c’) are used. Using Eq. (3.18) and the assumed linearity, the antenna temperature  $T_A(\nu)$  as well as the receiver temperature  $T_{\text{rec}}(\nu)$  can be derived from such a measurement:

$$T_A(\nu) = \frac{M_{\text{atm}}(\nu) - M_c(\nu)}{M_h(\nu) - M_c(\nu)} (T_h - T_c) + T_c \quad (3.19)$$

$$T_{\text{rec}}(\nu) = \frac{T_{\text{h}} - Y(\nu) T_{\text{c}}}{Y(\nu) - 1} \quad \text{with} \quad Y(\nu) = \frac{M_{\text{h}}(\nu)}{M_{\text{c}}(\nu)}. \quad (3.20)$$

This method has the advantage that it is comparatively simple to conduct. However, linearity of the receiver has to be assumed, although slight non-linearities are common for real receivers. This complication is tackled by the balanced calibration.

### 3.2.2.2 Balanced calibration

A strong influence of receiver non-linearities on the calibrated spectrum is avoided by the balanced calibration through basically a restriction of the calibration validity to one certain temperature, namely the system temperature  $T_{\text{sys}}$  of the particular measurement. This is achieved by measuring consecutively an atmospheric spectrum and a known spectrum of a reference source (index ‘r’). The temperature of this reference source,  $T_{\text{r}}$ , is adjusted such that the power detected during both measurements is equal. Note that this adjustment process is based on quantities integrated over the whole spectrum, so that the frequency dependency has been intentionally omitted in this paragraph so far. The spectral information is gained after the adjustment of the reference source by the measurement of the two raw spectra  $M_{\text{atm}}(\nu)$  and  $M_{\text{r}}(\nu)$ . The basic quantity is then the normalized difference  $\Delta M_{\text{atm,r}}(\nu)$  of both spectra,

$$\Delta M_{\text{atm,r}}(\nu) = \frac{M_{\text{atm}}(\nu) - M_{\text{r}}(\nu)}{M_{\text{r}}(\nu)}. \quad (3.21)$$

It is shown in, e.g., Krupa [1998] that the antenna temperature  $T_{\text{A}}(\nu)$  can be approximately derived from this quantity via

$$T_{\text{A}}(\nu) = \Delta M_{\text{atm,r}}(\nu) (T_{\text{r}} + T_{\text{rec}}(\nu)) + T_{\text{r}}. \quad (3.22)$$

It is therefore possible to obtain a calibrated spectrum with the balanced calibration, which is barely influenced by non-linearities by measuring only one additional source, thus 50 % of the measurement time is theoretically available for the atmospheric measurement. However, the receiver temperature  $T_{\text{rec}}(\nu)$  has to be known and the reference source has to be calibrated itself. For both, the hot-cold-calibration is still used, but less frequent.

Mainly two different realizations of the reference source needed for the balanced calibration are commonly used. Parrish et al. [1988] describe the ‘external beam switching’ method, which incorporates the atmosphere itself as reference. Alternatively, an internal adjustable reference source [e.g., Krupa et al., 1998] is used. This source contains basically two black bodies, similar to those of the hot-cold-calibration. The adjustability is achieved by superimposing appropriate fractions of the two beams of the hot and the cold source.

### 3.2.3 Critical hardware parameters

Aside from the calibration, two major hardware properties influence the quality of the obtained spectra and therefore the quality of the finally retrieved atmospheric properties. These are discussed below only briefly, but not without mentioning that the development of a microwave radiometer is still a much more complicated task in which many details

have to be considered to obtain high quality spectra of the weak atmospheric emission lines. For example, baseline disturbances like ‘standing waves’ and efforts to reduce nonlinearities are not discussed here. In addition to the literature that generally describes the microwave remote sensing technique [Janssen, 1993; Vowinkel, 1988], it is insightful to browse through the various PhD theses, which have been published in the last decades dealing with radiometry on hardware level, to get an impression of the complexity of these instruments (just to mention a few, Klein [1993] describes the development of a new radiometer, Krupa [1998] elaborates on the calibration, and Golchert [2009] characterizes artifacts in microwave raw spectra in order to deal with them in the retrieval).

### 3.2.3.1 Spectral resolution

The properties of the spectrometer generally determine the best quality of a spectrum that can be achieved. The basic quantities are the bandwidth and the spectral resolution  $\Delta\nu$ , since the altitude information is encoded spectrally in the broadening of the emission lines (Sect. 3.1.2.3). Lower altitudes are represented by comparatively broad emission lines, which might exceed the bandwidth of the spectrometer. In this case, no information on the respective altitudes is contained in the spectra. In the context of this work, however, a narrow line of mainly mesospheric emission is analyzed. Here, the achievable altitude resolution is determined by the smallest difference of linewidths, which can be spectrally resolved, thus by the spectral resolution (Quantitative considerations on an adequate spectral resolution particularly for the CO emission analyzed in the study are discussed in Sect. 4.3.3).

In the past decades, it was necessary to use different types of spectrometers for different applications (e.g., an acousto-optical spectrometer (AOS) for a high bandwidth, but only moderate spectral resolution or a chirp-transform spectrometer (CTS) for a high spectral resolution, but a lower bandwidth). A recent development, the fast Fourier transform spectrometer (FFTS) [Benz et al., 2005], combines both features sufficiently for atmospheric measurements [Müller et al., 2009]. With this technique, the analog electromagnetic signal is directly converted to a digital representation with a fast analog-to-digital converter (ADC). Afterwards, it is realtime fast Fourier transformed using a digital processor, the field programmable gate array (FPGA), to obtain the spectrum. The major invention of this technique is the fact that the spectrum is generated digitally, which promises a high level of stability and accuracy and at the same time a high spectral resolution combined with a sufficient bandwidth.

### 3.2.3.2 Detection limit

The detection limit represents the smallest change  $\Delta T_A$  of the antenna temperature  $T_A$  that can be unambiguously detected by a microwave receiver. This is closely linked to the well known signal-to-noise ratio (SNR), however, the focus in microwave radiometry is usually the reduction of noise. Since the signal is mainly determined by the atmospheric conditions, there are only few possibilities to optimize the signal. The SNR does not only control which line is generally detectable, but influences also the altitude resolution that can be achieved.

The only parameter influencing the input signal is the elevation angle, which controls the length of the optical path through the atmosphere and therefore the amount of emitting

and absorbing molecules in the line of sight. An optimal elevation angle is found for a given atmospheric state as a trade-off considering that a longer path length means more observed emission from the middle atmosphere but also more absorption by the atmosphere below.

The noise level of a spectrum defines  $\Delta T_A$ , so that the noise has to be reduced until the required SNR is reached for the respective signal. For a fixed bandwidth,  $\Delta T_A$  is given by the radiometer formula [Vowinkel, 1988]

$$\Delta T_A \propto \frac{T_{\text{sys}}}{\sqrt{\Delta\nu \cdot t_{\text{int}}}} \approx \frac{T_{\text{rec}}}{\sqrt{\Delta\nu \cdot t_{\text{int}}}} \quad (3.23)$$

with the integration time  $t_{\text{int}}$  of the spectrum. Here, the spectral resolution  $\Delta\nu$  is interpreted as the ‘bandwidth’ of one spectrometer channel. Hence,  $\Delta T_A$  is the detection limit per spectrometer channel; the coarser the resolution is, the broader the channels are and the more noise is averaged out. The equation has to be modified by a factor in the order of 2 to achieve equality, depending on the calibration approach and considered noise contributions.

Given that  $\Delta\nu$  is fixed by the application of the measurements, two possibilities of noise reduction are obvious. First, an extension of the integration time  $t_{\text{int}}$ . Unfortunately, this approach becomes less effective with longer integration times since the square root of the integration time is relevant. Second, the receiver noise temperature  $T_{\text{rec}}$  can be reduced, which is actually a major aspect for the development of microwave radiometers, but is not discussed here in detail. Vowinkel [1988] shows that the first components in the signal processing chain behind the antenna contribute most to  $T_{\text{rec}}$ . Furthermore, their noise contributions depend dominantly on their temperature. Therefore, these components are specially designed to produce low internal noise and are additionally cooled for a further reduction of the internal noise.

## 3.3 Retrieval of vmr profiles from microwave spectra

### 3.3.1 Inversion

The direct result of a microwave measurement is a calibrated spectrum, which contains at least one emission line of the respective atmospheric molecule. The ‘retrieval’ process aims at the extraction of the sought quantity from such a spectrum, here a vmr profile of the trace gas CO. The general relationship between the spectrum and the atmospheric information has been outlined in Sect. 3.1. In particular, the solution of the transfer equation (Eq. 3.4) expresses this relation. However, it works naturally in the opposite direction, i.e., it assigns a spectrum to a given atmospheric state. Hence, this equation has to be inverted, which is a non-trivial problem that is tackled with the numerical retrieval process.

The general idea is to evaluate Eq. (3.4) in its natural direction, thus to simulate a spectrum<sup>2</sup>  $\mathbf{y}$ , which would have been measured if the atmosphere had been in a given

<sup>2</sup>The notation in this section adopts the standard notation. Aside from the consistency with the standard literature, this indicates a higher level of generality in this section. Thus, the spectrum  $T_b(\nu)$  in Sect. 3.1 is a special instance of the spectrum  $\mathbf{y}$  in this section.

state  $\mathbf{x}$ . The assumed atmospheric state  $\mathbf{x}$  is then iteratively modified until the simulated spectrum fits the measured one under consideration of the measurement noise  $\boldsymbol{\epsilon}$ . The simulation is performed by the ‘forward model’  $\mathbf{F}$ , which basically implements the theory discussed in Sect. 3.1,

$$\mathbf{y} = \mathbf{F}(\mathbf{x}) + \boldsymbol{\epsilon}. \quad (3.24)$$

The inversion is, however, an ill-posed problem and does not necessarily have a unique solution, so that a regularization is necessary to find the appropriate solution.

In this study, the ‘optimal estimation (OE)’ method has been applied, so that the present discussion is restricted to this particular retrieval approach. OE has been described extensively in Rodgers [2000], which is also the basis for the present review. The regularization approach implemented by OE is the usage of ‘a priori’ knowledge, which characterizes the mean state of the retrieved quantity, to constrain the solution. In particular, the mean and the covariance of a Gaussian distribution are used as the a priori profile  $\mathbf{x}_a$  and the a priori covariance matrix  $\mathbf{S}_a$ , respectively. The noise  $\boldsymbol{\epsilon}$  on the measured spectrum  $\mathbf{y}$  is considered by the inclusion of the measurement noise covariance matrix  $\mathbf{S}_\epsilon$ . The best estimator  $\hat{\mathbf{x}}$  for the true atmospheric state in OE is then found by minimizing the cost function  $J_C$

$$J_C = [\mathbf{y} - \mathbf{F}(\mathbf{x})]^T \mathbf{S}_\epsilon^{-1} [\mathbf{y} - \mathbf{F}(\mathbf{x})] + [\mathbf{x} - \mathbf{x}_a]^T \mathbf{S}_a^{-1} [\mathbf{x} - \mathbf{x}_a]. \quad (3.25)$$

For this minimization, the Jacobian of the forward model  $\mathbf{F}$  is necessary, which is also an important quantity in the retrieval theory further on. It is often called ‘weighting function matrix’ and is identified by the symbol  $\mathbf{K}$ :

$$\mathbf{K} = \frac{\partial \mathbf{F}}{\partial \mathbf{x}}. \quad (3.26)$$

The derivative of  $J_C$  with respect to  $\mathbf{x}$  is set to zero to find the best estimator  $\hat{\mathbf{x}}$  as minimal value:

$$\left. \frac{dJ_C}{d\mathbf{x}} \right|_{\mathbf{x}=\hat{\mathbf{x}}} = -\mathbf{K}^T(\hat{\mathbf{x}}) \mathbf{S}_\epsilon^{-1} [\mathbf{y} - \mathbf{F}(\hat{\mathbf{x}})] + \mathbf{S}_a^{-1} [\hat{\mathbf{x}} - \mathbf{x}_a] = 0. \quad (3.27)$$

This equation has to be solved iteratively with a numerical approach, a problem for which several methods are available and well established. Here, the Levenberg-Marquardt approach is generally used, which works for the conditions of this study, however, close to the well known Gauss-Newton method [Rodgers, 2000]. With the definition of another important matrix, the ‘contribution function matrix’  $\mathbf{D}$ ,

$$\mathbf{D} = (\mathbf{K}^T \mathbf{S}_\epsilon^{-1} \mathbf{K} + \mathbf{S}_a^{-1})^{-1} \mathbf{K}^T \mathbf{S}_\epsilon^{-1}, \quad (3.28)$$

the best estimator  $\hat{\mathbf{x}}$  for the true atmospheric state  $\mathbf{x}$  can be expressed as follows after the iteration has converged

$$\hat{\mathbf{x}} = \mathbf{x}_a + \mathbf{D}(\mathbf{y} - \mathbf{K}\mathbf{x}_a). \quad (3.29)$$

### 3.3.2 Characterization of the retrieval results

It is recommended to turn over occasionally to Sect. 4.3 (p. 54), where the following theory is applied, which may be helpful as example.

An important quantity for the characterization of the information content of the retrieval results is the averaging kernel (AVK) matrix  $\mathbf{A}$ , which relates changes of the true state  $\mathbf{x}$  to changes of the retrieved state  $\hat{\mathbf{x}}$ . It can be expressed as the product of the matrices  $\mathbf{D}$  and  $\mathbf{K}$ :

$$\mathbf{A} = \frac{\partial \hat{\mathbf{x}}}{\partial \mathbf{x}} = \mathbf{D}\mathbf{K}. \quad (3.30)$$

The meaning of the AVKs is easier to understand if the retrieved state  $\hat{\mathbf{x}}$  is considered to be a trace gas profile only, although the theory is more general and  $\hat{\mathbf{x}}$  usually contains further quantities. In this case, a certain row  $A^i$  of the AVK matrix contains the AVK for the respective altitude  $z^i$ , the ‘target altitude’. This AVK is a measure for the sensitivity of the retrieved state  $\hat{x}^i$  at its target altitude to perturbations of the true state in any single altitude considered in the retrieval. Thus, dependencies between individual elements of the retrieved profile are explicitly considered in the non-diagonal elements of  $\mathbf{A}$  and express the limited altitude resolution of a non-ideal measurement. An ideal measurement would, in turn, result in  $\mathbf{A}$  being the unity matrix. However, the ideal case is not achievable in reality, since the retrieved state is not only governed by the atmospheric state, but is also affected by the measurement noise, the instrumental properties, and the a priori.  $\mathbf{A}$  deviates therefore always from the unity matrix, but it contains an estimation of the real information content of the retrieval results and the resulting limitations as described below.

The relationship of the retrieved state  $\hat{\mathbf{x}}$  and the real atmospheric state  $\mathbf{x}$ , under consideration of the influence of the a priori  $\mathbf{x}_a$  and the limitations expressed in  $\mathbf{A}$ , is given by the important transfer equation

$$\hat{\mathbf{x}} = \mathbf{x}_a + \mathbf{A}(\mathbf{x} - \mathbf{x}_a). \quad (3.31)$$

A major application of this equation is the comparison of the retrieved profiles with vertically better resolved data. As Eq. (3.31) expresses, the retrieval results do not represent the atmosphere as it is, but an atmosphere smoothed with the AVKs. Vertically better resolved data are therefore only comparable to the retrieved data if they undergo the same smoothing. For such comparisons as, e.g., the satellite comparisons in this work (Chap. 5), it is usually assumed that the vertically better resolved data represent the real atmosphere, so that they can be put into Eq. (3.31) in place of the true state  $\mathbf{x}$ .

### 3.3.2.1 Sensitivity

The retrieved value  $\hat{x}^i$  at a certain target altitude  $z^i$  is generally assumed to be sensitive to the true atmospheric state if the area under the corresponding AVK is close to unity. If the area is much smaller, which indicates a greater influence of the a priori on the retrieved state, the result is often meaningless or it has at least to be handled with care. A common threshold, above which the sensitivity is considered to be uncritical, is 0.8. The area of the AVK for a certain altitude is numerically calculated by summing up the respective row of the AVK matrix.

In microwave radiometry, the lower altitude limit of the sensitivity is physically either defined by the bandwidth of the spectrometer or by the noise of the spectrum. Both prevents the broad and flat part of the emission line from being included in the analysis. The upper limit is either defined by the transition from the pressure broadening regime

to the Doppler broadening regime or by the frequency resolution of the spectrometer if its channels are wider than the pressure broadened line above a certain altitude.

### 3.3.2.2 Vertical resolution

The AVKs are usually Gaussian-like peaked functions. The vertical resolution of the measurement in a certain altitude  $z^i$  is then indicated by the full width at half maximum (FWHM) of the respective AVK. However, the AVKs show occasionally a quite oscillatory shape, for which the FWHM concept is not adequate. The sensitivity of such AVKs is, however, often low, so that this problem usually occurs in irrelevant regions. In problematic cases, the degrees of freedom in the measurements can alternatively be calculated to obtain an indication of the information content.

### 3.3.2.3 Degrees of freedom

The number of independent pieces of information in a retrieved profile can on the one hand be estimated from the vertical range, in which the sensitivity is close to unity in relation to the vertical resolution. On the other hand, an alternative measure for the degrees of freedom of the observation is the trace of the AVK matrix, which can be employed if the vertical resolution is problematic to calculate. The degrees of freedom provide then together with the sensitive range a rough indication of the vertical resolution.

### 3.3.2.4 Center altitudes of the AVKs

Although each AVK is assigned to a certain target altitude  $z^i$ , it can occasionally be sensitive to a different altitude region. Therefore the ‘center’ of the AVK is calculated as a weighted mean over all altitudes considered in the retrieval, using the AVK entries as weighting factors. Ideally, the target and center altitudes are identical and possible differences may indicate deficiencies of the retrieval in the respective altitude. However, the differences have to be seen in relation to the respective vertical resolution, which is often coarse, such that the observed deviation from the target altitude is neglectable.

## 3.3.3 Error estimation

The realization of the error assessment is based on Palm et al. [2010], and thereby also follows the description in Rodgers [2000]. The deviation of the retrieved state  $\hat{\mathbf{x}}$  from the unknown true state  $\mathbf{x}$  can be expressed as the sum of certain error contributions, in particular the smoothing error (Eq. 3.32), the forward model error (Eq. 3.33), the errors of the forward model parameters (Eq. 3.34), and the noise error (Eq. 3.35):

$$\hat{\mathbf{x}} - \mathbf{x} = (\mathbf{A} - \mathbf{I})(\mathbf{x} - \mathbf{x}_a) \quad (3.32)$$

$$+ \mathbf{D} \Delta \mathbf{F}(\mathbf{x}, \mathbf{b}, \hat{\mathbf{b}}) \quad (3.33)$$

$$+ \mathbf{D} \mathbf{K}_b (\mathbf{b} - \hat{\mathbf{b}}) \quad (3.34)$$

$$+ \mathbf{D} \boldsymbol{\epsilon}, \quad (3.35)$$

with  $\mathbf{b}$  denoting the true forward model parameters,  $\hat{\mathbf{b}}$  the respective estimates used in the retrieval,  $\mathbf{K}_b = \frac{\partial \mathbf{F}}{\partial \mathbf{b}}$  the Jacobian of the forward model with respect to the parameters  $\mathbf{b}$ , and  $\Delta \mathbf{F}$  the deviation of the forward model implementation from the true forward model.

The first two error sources are not examined for the retrieval presented in this study since an estimate is difficult and in the present context not necessary. The smoothing error denotes that the retrieved profile is inexact due to the limited vertical resolution. For the estimation of this error, a precise statistical description of the true state is necessary [Rodgers, 2000], which is not available. However, since information about the vertical resolution is stored in the AVKs, another way of dealing with this error source is to provide the AVKs and the a priori together with the profiles. Following this approach, the retrieved profiles cannot be interpreted as an estimate of the real atmosphere with an error contribution due to the smoothing, but only as an estimate of the smoothed atmosphere. Comparisons are then only meaningful if data representing the real atmosphere are also smoothed with the AVKs (Sect. 3.3.2) using Eq. (3.31), which addresses the smoothing error indirectly. This interpretation implies that the full set of retrieval results includes the AVKs as well as the a priori aside from the actual profiles.

The other error not examined in the present study is caused by possible deficiencies of the forward model. It can only be estimated in comparison with other models and the performance of the forward model used in this study has already been examined by Melsheimer et al. [2005]. Moreover, a comparison of the retrieval results to independent datasets, as conducted here in Chap. 5, indicates error margins independent from the estimated—and not estimated—error contributions.

For the calculation of the third contribution, meaning the errors  $\sigma_{\text{fp}}$  caused by the uncertainties of the forward model parameters, the expression  $\mathbf{D} \mathbf{K}_b$  in Eq. (3.34) is identified as an AVK matrix  $\mathbf{A}_b$  with respect to these parameters. It is derived from a numerical calculation of the respective derivatives,

$$\mathbf{D} \mathbf{K}_b = \mathbf{A}_b = \frac{\partial \hat{\mathbf{x}}}{\partial \mathbf{b}}. \quad (3.36)$$

With an estimated covariance matrix of the forward model parameters  $\mathbf{S}_b$ , the respective covariance matrix of the retrieved profile  $\mathbf{S}_{\text{fp}}$  is derived using

$$\mathbf{S}_{\text{fp}} = \mathbf{A}_b \mathbf{S}_b \mathbf{A}_b^T. \quad (3.37)$$

Finally, the standard deviation of a retrieved profile, caused by the uncertainties of the forward model parameters, is given by

$$\sigma_{\text{fp}}^i = \sqrt{S_{\text{fp}}^{ii}}, \quad (3.38)$$

without consideration of off-diagonal entries.

The fourth error contribution  $\sigma_\eta$ , caused by the noise on the spectrum, is calculated using the noise covariance matrix  $\mathbf{S}_\epsilon$  via

$$\mathbf{S}_\eta = \mathbf{D} \mathbf{S}_\epsilon \mathbf{D}^T \quad (3.39)$$

and

$$\sigma_\eta^i = \sqrt{S_\eta^{ii}}. \quad (3.40)$$

# 4 Retrieval of CO profiles from the Kiruna Microwave Radiometer data

Large parts of this chapter have been published by Hoffmann et al. [2011].

The basis for the studies in the following chapters is a time series of CO profiles from Kiruna, northern Sweden. These CO profiles have to be retrieved at first from the microwave spectra measured with the Kiruna microwave radiometer (KIMRA). This retrieval as well as the retrieved CO time series are presented in this chapter. Aside from being the basis for the present thesis, the developed retrieval setup also serves as the basis for future analyses of the ongoing observations.

The analyzed spectra have been provided by the Swedish Institute of Space Physics (IRF), which operates KIMRA.

## 4.1 Properties of the KIMRA CO measurements

### 4.1.1 Measurement location

The observations are carried out in Kiruna, northern Sweden (67.8° N, 20.4° E, 425 m elevation; see Fig. 4.1). The state of the middle atmosphere above this location is during winter usually given by polar vortex conditions. Since Kiruna is, however, close to the Arctic circle, the vortex boundary passes occasionally over the instrument and CO poor air from the mid-latitudes is measured [Raffalski et al., 2005]. This provides the opportunity of a comparison of vortex and mid-latitude air masses in a continuous dataset, as well as the investigation of the timing of the overpasses in models. In turn, this fact requires the separation of these periods if only inner vortex air should be analyzed.

### 4.1.2 Instrument

Since this work deals with the retrieval and interpretation of already obtained spectra, the instrument KIMRA is described here only in so far as it is necessary to understand the following sections; details can be found in Raffalski et al. [2002, 2005]. KIMRA was developed by the Institute for Meteorology and Climate Research (IMK) at the Karlsruhe Institute of Technology (KIT) and is operated in Kiruna by the Swedish Institute of Space Physics (IRF).

In principle, the instrument covers the relatively broad frequency range from 195 GHz to 234 GHz, in which emission lines of different species are located. In a first period of operation, however, only O<sub>3</sub> measurements have been performed [Raffalski et al., 2005] using a wide-band AOS with a bandwidth of 1.2 GHz distributed over 2048 channels. Data of this period were used for the validation of the instruments Global Ozone Monitoring by Occultation of Stars (GOMOS) [Meijer et al., 2004] and MIPAS [Steck et al., 2007] on

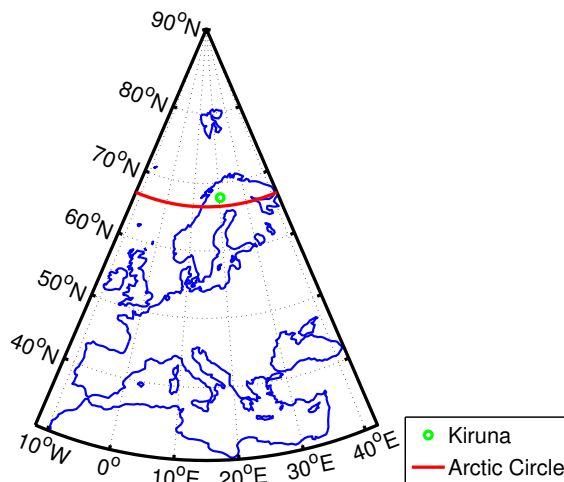


Figure 4.1: Map of Europe showing the location of the KIMRA instrument in Kiruna, northern Sweden, close to the Arctic Circle.

board the satellite Envisat. In 2007, KIMRA was extended to be capable of measuring CO in the middle atmosphere by the integration of a high-resolution FFTS. This spectrometer provides a frequency resolution of 107 kHz (bandwidth of 110 MHz distributed over 1024 channels), which matches the order of the the narrow CO emission line at 230 GHz (Sect. 4.3.3). Since then, KIMRA has been routinely operated with both spectrometers, thus it measures CO simultaneously with  $O_3$ ; a sketch of the respective spectral region is shown in Fig. 4.2. The present work is, however, focused on the CO data obtained with the FFTS.

KIMRA works with a cryogenically cooled Schottky diode mixer and has a receiver noise temperature of about 1800 K in single side band (SSB) mode. The spectra are calibrated according to the balanced calibration method (Sect. 3.2.2.2) using an internal adjustable reference load [Berg et al., 1998]. The viewing direction is adjusted with a periscope-like mirror system, which allows for observations in the complete hemisphere (azimuth angle between  $0^\circ$  and  $360^\circ$ , elevation angle between  $0^\circ$  and  $90^\circ$ ). Whereas the azimuth angles of all the observations in this work are either  $0^\circ$  or  $180^\circ$ , the optimal elevation angle is automatically chosen according to the tropospheric transmissivity (Sect. 3.2.3.2). In case of a significant change of the tropospheric conditions demanding a different elevation angle during a measurement, the ongoing observation is stopped and a new measurement is automatically started, using the a new optimal elevation angle. Therefore, the integration time per spectrum is not constant, but varies between 30 min and 360 min. All spectra obtained are generally saved without any further quality check at the time of the measurement and are sorted later in the retrieval process according to the particular requirements.

### 4.1.3 Dataset

The CO spectra obtained so far generally cover the three winters 2007/2008 to 2009/2010. However, during the first winter of CO measurements, the instrument was still in an

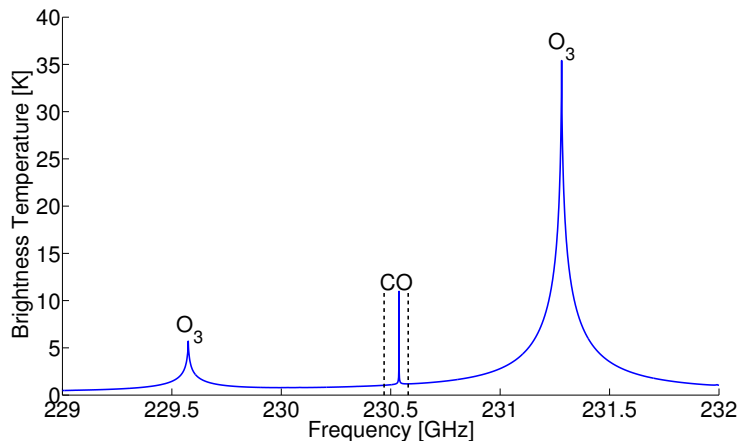


Figure 4.2: Sketch of the emission lines in the spectral region close to the CO emission line at 230 GHz simulated with the forward model ARTS. The black dashed lines indicate the spectral region covered by the FFTS. Continuum emission has been omitted in the calculation of this plot since it only serves as visualization of the line positions. Figure adopted from Hoffmann et al. [2011].

experimental state and the spectra turned out not to have the desired calibration quality. Reliable CO measurements are available from December 2008 on, so that this work deals with the analysis of the periods December 2008 to April 2009 (‘winter 08/09’) and September 2009 to April 2010 (‘winter 09/10’). During these periods, measurement gaps of several days to weeks exist due to instrument maintenance and bad weather conditions. Furthermore, measurements from the summer months are generally not analyzed since the increased humidity causes the background radiation to be too high for reasonable CO retrievals.

The SNR is not constant throughout the complete set of spectra due to both changes in the atmosphere (humidity and CO itself) and changes of instrument parameters (elevation angle, azimuth angle, and the integration time; Sect. 4.1.2). A quality check is applied before retrieving the spectra, which was adjusted in tests under consideration of different criteria (total integration time, ratio of atmospheric and calibration integration time, spikes in the spectra, noise). A disadvantage of the elevation angle change between single measurements is that spectra cannot be averaged to produce data with a uniform integration time. This is only possible if the light path through the troposphere and the related attenuation of the middle atmosphere signal are known. The spectra are therefore retrieved as they are and the profiles have to be averaged afterwards if necessary. Consequential, the retrieval quality also varies strongly, so that it is characterized in the following either by averages over all results or by typical examples that correspond to the mean values. In contrast, the change of the azimuth angle is not relevant for the retrieval but may be considered in analyses of the obtained profiles if this is of interest.

The finally retrieved dataset contains 1497 spectra, which are distributed over 309 days in the measurement period and have a mean atmospheric integration time of 1 h. Further basic properties of the retrieved dataset are compiled in Table 4.1.

Table 4.1: Basic characteristics of the retrieved dataset.

Period	Dec. 2008–Apr. 2009 Sep. 2009–Apr. 2010
Days covered	309 of 393
Total number of spectra	1497
Mean number of measurements per day	3.8
Mean integration time per spectrum	$59 \pm 20$ min
Mean noise on spectra	$0.20 \pm 0.04$ K
Mean elevation angle	$30^\circ \pm 15^\circ$
Min/Max elevation angle	$5^\circ/90^\circ$
Number of spectra with azimuth $180^\circ$	802
Number of spectra with azimuth $0^\circ$	695

## 4.2 Retrieval setup

The retrieval setup has not been modified since its publication by Hoffmann et al. [2011], so that the retrieval version described here, ‘KIMRA CO version 1.1’, is identical.

### 4.2.1 Forward model and inversion software

The forward model (Sect. 3.3.1) for the radiative transfer calculations employed here, is the atmospheric radiative transfer simulator (ARTS), version 1.0.216 [Bühler et al., 2005]. Besides the CO emission line of interest at 230 GHz, ozone lines in this spectral region are also modeled to account for their influence on the baseline (Fig. 4.2). The continuum absorption of  $\text{H}_2\text{O}$ ,  $\text{O}_2$ , and  $\text{N}_2$  is accounted by the inclusion of the MPM93 absorption model [Bühler et al., 2005, and references therein]. The line parameters as input for the forward model are taken from the high-resolution transmission molecular absorption database (HITRAN), version of 2004 [Rothman et al., 2005].

The inversion according to the OE approach (Sect. 3.3.1) is performed using the package Qpack, version 1.0.93 [Eriksson et al., 2005], which is specifically designed to work together with the forward model ARTS.

### 4.2.2 Numerical setup

The retrieval is performed on a pressure grid that corresponds to fixed altitudes with 1 km spacing between 0.5 km and 130.5 km, which is much more narrow than the actual vertical resolution of the measurement. Such a narrow grid is used to gain numerical stability of the retrieval although it may cause spurious structures of smaller vertical extent in the retrieved profile, which do not have a representation in the real atmosphere (Sect. 4.4.1). However, this is unproblematic since the real vertical information content is given by the AVK functions (Sect. 3.3.2, Sect. 4.3).

The vertical extent of the retrieval reaches higher than it is commonly the case for middle atmosphere retrievals, which usually end at about 100 km altitude [e.g., Palm et al., 2010; Bevilacqua et al., 1985]. The extension is necessary for CO because of the strong

increase of the CO vmr with altitude towards the thermosphere (Sect. 2.4), which causes the detection of a residual signal from this altitude region. This has to be considered in the retrieval, although no independent information can be derived from this region. This extension demands for new sources of the meteorological input data (Sect. 4.2.3) and additional considerations on the Doppler broadening in this region (Sect. 4.2.5).

In order to deal with the strong vertical gradient in the CO vmr (Sect. 2.4), the retrieved quantity is the profile  $\hat{\mathbf{x}}_{\text{norm}}$  normalized with the a priori  $\hat{\mathbf{x}}_{\text{a}}$ , instead of the vmr profile  $\hat{\mathbf{x}}_{\text{vmr}}$  itself:

$$\hat{x}^i = \hat{x}_{\text{norm}}^i = \frac{\hat{x}_{\text{vmr}}^i}{x_{\text{a}}^i}. \quad (4.1)$$

The gained AVK matrix also corresponds to the normalized profiles ( $\mathbf{A} = \mathbf{A}_{\text{norm}}$ ) and has to be converted to be representative for the vmr profile

$$A_{\text{vmr}}^{ij} = x_{\text{a}}^i \cdot A_{\text{norm}}^{ij} / x_{\text{a}}^j. \quad (4.2)$$

In the following, the short terms ‘normalized AVK’ matrix and ‘vmr AVK’ matrix are used to refer to  $\mathbf{A}_{\text{norm}}$  and  $\mathbf{A}_{\text{vmr}}$  respectively, although both representations are dimensionless.

### 4.2.3 Input data

Pressure- and temperature profiles, needed as input for the retrieval, have generally been taken from the satellite instrument Sounding of the Atmosphere using Broadband Emission Radiometry (SABER) [Remsberg et al., 2008] due to its high vertical coverage. Only the lower part up to 17 km altitude comes from European Centre for Medium-Range Weather Forecasts (ECMWF) Operational Analyses data. Usually, ECMWF data are used in the complete available vertical range for retrievals performed in the group ‘radiometer for atmospheric measurements (RAM)’ at the University of Bremen. Missing data up to the common retrieval limit at 100 km are thereby filled with a static extension [Palm et al., 2010]. However, due to the greater importance of this region for the CO signal (Sect. 4.2.2) and the higher retrieval limit at 130 km altitude, a static extension turned out to be insufficient for the CO retrieval, so that the SABER measurements are used.

Whereas SABER data have the additional advantage of being measured and not modeled data, a disadvantage is the certain discontinuity of the SABER time series when the satellite ceases operation. This discontinuity will necessarily result in a discontinuity of the intended KIMRA long-term time series. Furthermore, the relevant satellite data have to be selected using particular collocation criteria, which is especially difficult for SABER in the latitudes around Kiruna. A collocation box from 50° N to 75° N latitude and 15° E to 25° E longitude has been chosen and the respective profiles are averaged daily prior to the use in the retrieval. The collocation box extends so far south because the northern edge of the SABER coverage changes from 83° N (north viewing mode) to 52° N (south viewing mode) approximately every 60 days [Remsberg et al., 2008]. Thus, during periods with usage of the south viewing mode, only the southernmost part of the chosen collocation box contains profiles. A possible bias caused by this fact has been considered in the error assessment (Sect. 4.5).

The a priori profiles of CO (Fig. 4.8), as well as of O<sub>3</sub>, O<sub>2</sub>, and H<sub>2</sub>O, are based on a simulation of SD-WACCM4 (a previous model version is described in Garcia et al. [2007];

a description of this particular simulation is included in Chap. 6 of this work). An average profile over a complete modeled winter is constantly used as a priori for the whole retrieved time series. This gives, in addition to the detailed retrieval characterization (Sect. 4.3), the confidence that all retrieved temporal variations of the CO vmr (Sect. 4.4.2) come from the measurement alone and are not induced artificially by changes of the a priori. The used  $N_2$  abundance is taken from the Fast Atmospheric Signature Code (FASCOD) subarctic winter scenario [Anderson et al., 1986]. The a priori covariance matrix  $\mathbf{S}_a$  has initially been based on the respective SD-WACCM4 CO standard deviation, but was then empirically modified to give the retrieval enough freedom to fit the spectra of the whole course of the winter sufficiently. Major changes have thereby been made above 80 km altitude, where the available information on the CO statistics is least certain. Non-diagonal elements are zero, thus possible correlations between vertical layers are not considered. Like the a priori profiles,  $\mathbf{S}_a$  is also left constant for the complete retrieval run. It is defined in fractions of the a priori on the retrieval grid. To visualize the final a priori covariance matrix, the diagonal elements converted to absolute vmr,  $\sqrt{S_a^{ii}} \cdot x_a^i$ , are shown in Fig. 4.8, red dashed curve. The noise covariance matrix  $\mathbf{S}_\epsilon$  is calculated for each spectrum from the noise in a region that only contains the background signal.

#### 4.2.4 Inclusion of instrumental properties

The retrieval does not only account for the radiative transfer in the atmosphere, but also for the preprocessing of the radiation in the receiver, following an approach developed by Eriksson et al. [2005, 2006]. Particularly, the frequency conversion by the signal processing chain, as well as the resolution function of the spectrometer (sinc-function according to a boxcar apodization) are considered straightforwardly by recalculating the overall effect on the originally observed frequencies.

Furthermore, the retrieval accounts for instrumental artifacts, which cannot completely be suppressed during the measurements. In particular, the magnitude of standing waves is fitted, which are undulations of the spectrum baseline that arise from minor reflections in the instrument optics [e.g., Berg, 2000; Golchert, 2009]. Generally, accounting for these artifacts can be challenging since it is often difficult to distinguish these standing waves from the actual emission line. In the present case, however, the emission line is much smaller than the spectral bandwidth, so that large parts of the spectrum directly show the disturbed baseline and can be used to identify the standing waves. Additionally, the standing waves have in the present case relatively large wavelengths, so that they are distinguishable from the emission line. Fits of standing waves with three different wavelengths (55 MHz, 36.6 MHz, and 27.5 MHz) are part of each retrieval result. The fitted amplitudes are of the order of 0.1 K. Likewise, a baseline offset of the order of about 1 K is fitted. An example of a measured spectrum, as well as the same spectrum corrected for these instrumental artifacts, is shown in Fig. 4.3.

#### 4.2.5 A remark about the line broadening of thermal CO emission

Pressure broadening can roughly be considered to decrease exponentially with altitude in the atmosphere, whereas Doppler broadening is roughly constant with altitude (Sect. 3.1.2.3). The region where pressure and Doppler broadening are equally strong is

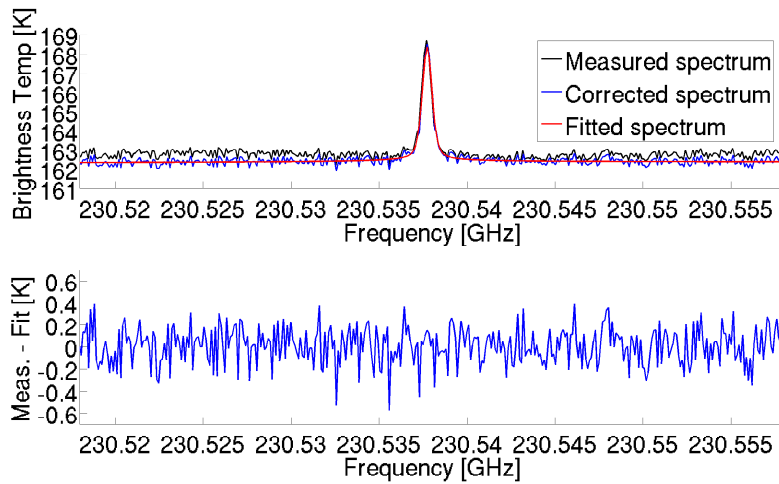


Figure 4.3: **Top:** spectrum measured on 29 October 2009, 06:52 h (black) and the same spectrum corrected for standing waves (blue), together with the fit calculated by the retrieval process (red). **Bottom:** the corresponding residuum (difference of the corrected spectrum and the fitted spectrum), which contains only noise contributions, showing that the CO line was fitted adequately. Figure adopted from Hoffmann et al. [2011].

located in the mesosphere, so that both effects have to be considered for measurements with mesospheric interest. Above, the Doppler broadening dominates completely and no altitude information can be retrieved anymore. Commonly, the linewidth above this altitude is considered to be constant up to the end of the retrieval range, so that the highest altitude which can be resolved is defined by the transition from pressure to Doppler broadening (Sect. 3.1.2.3).

However, it has become evident in the context of this work that this assumption does not hold for CO anymore since the CO spectra contain residual contributions from the thermosphere, which is a result of the relatively large CO vmr in this region. Because the temperature of the thermosphere increases strongly with altitude, it is expected that also the Doppler broadening is not constant with altitude anymore, but that it increases with altitude. This leads to an ambiguity of the linewidths from thermospheric contributions and contributions from below.

This is confirmed by a calculation of the half widths of the contributions from single altitudes (Fig. 4.4). This calculation is based on the Eqs. (3.13), (3.15), and (3.17) used with meteorological data of an example retrieval run (discussed in more detail as typical retrieval result in Sect. 4.4.1). With a common retrieval setup ending at 100 km the linewidth would decrease monotonically in the complete vertical range. The highest resolvable altitude would be about 80 km, above which the Voigt linewidth equals the Doppler linewidth. However, due to the increasing linewidth above 100 km, the ambiguity of linewidths is introduced and the highest altitude level that is certainly resolved unambiguously is only about 62 km. Emissions from this altitude contribute with the same linewidth as emissions from 130 km altitude (Fig. 4.4, dashed lines). Since the increase of the linewidth is broader than the spectrometer resolution (Fig. 4.4, black lines), the effect

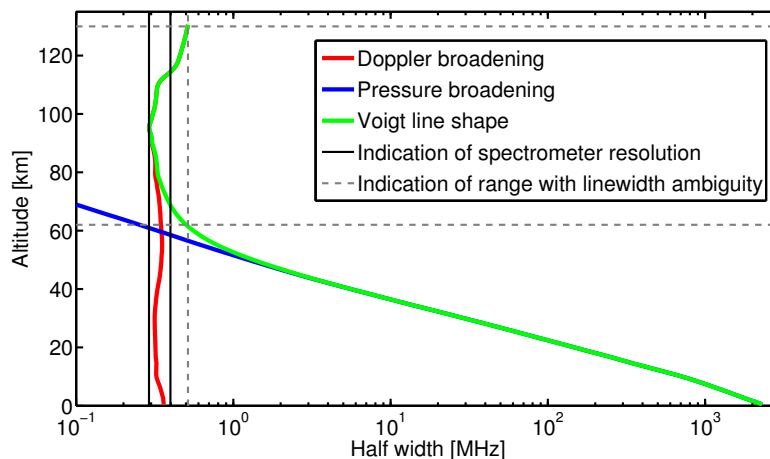


Figure 4.4: Half widths of the individual CO emission lines at 230 GHz originating from different altitudes. The Voigt line shape includes the combined effects of pressure and Doppler broadening; additionally, the individual contributions from pressure and Doppler broadening are shown separately. The linewidth decreases monotonically with altitude up to about 100 km, whereas it increases above due to the increasing temperatures in the thermosphere. This causes an ambiguity of the linewidths originating from the region between 62 km and 130 km altitude, as indicated by the gray dashed lines. The black lines indicate the frequency resolution of the FFTS. The linewidths were computed using the Eqs. (3.13), (3.15), and (3.17) with meteorological data of the standard retrieval example of 29 October 2009 (Sect. 4.4.1).

should also be relevant if the limited spectrometer resolution is considered. However, the actual relevance of this ambiguity for the application is also determined by the individual strengths of the signals from the respective altitudes and has to be revealed in the retrieval characterization below (Sect. 4.3).

### 4.3 Characterization of the retrieval results

The performance of the retrieval is specified by examining particular properties of the AVK matrix (Eq. 3.30) according to Sect. 3.3.2. The diagnostics directly linked to the retrieval output is the normalized AVK matrix  $\mathbf{A}_{\text{norm}}$  (Sect. 4.2.2). However, since the vmr AVK matrix  $\mathbf{A}_{\text{vmr}}$  is mainly used for comparisons to other measurements, this representation is also discussed here.

Since the SNR, which determines the information content, is not constant (Sect. 4.1.3), the retrieval quality is also not uniform for the complete set of spectra. Therefore, general properties of the AVKs, calculated as averages over the whole dataset, are discussed first (Sect. 4.3.1). Then a typical set of AVKs is shown (Sect. 4.3.2).

Note that the retrieval performance is not compared here to the previous ground-based CO measurements summarized before (Sect. 2.4.3). Generally, this might be an additional indication for the functioning of the developed retrieval setup. However, such

a comparison is not expected to be conclusive since many properties (integration time, receiver noise temperature, measured CO transition, spectral resolution) of the underlying measured spectra differ significantly, which influences the retrieval characteristics. To give a rough idea, sensitive vertical ranges between 50 km and 85 km altitude and vertical resolutions between about 7 km and 20 km have been reported in previous studies.

### 4.3.1 Average characteristics

#### 4.3.1.1 Sensitivity

Assuming that an AVK with an area greater than 0.8 contains enough information from the measurement, we find general sensitivity (Fig. 4.5a) in a range of 27 km to 83 km for the normalized retrieval and a range of 34 km to 87 km for the retrieval converted to vmr. This range matches the maximum expectations, but is narrowed by considering further criteria in the following.

The already mentioned fact that the instrument receives a residual signal from altitudes up to 130 km, which is due to the comparatively high amount of CO in the thermosphere, manifests itself here in a sensitivity greater than zero up to this altitude. This gave rise to the consideration of these altitudes in the retrieval, although the signal is not strong enough to derive independent information.

#### 4.3.1.2 Center altitudes of the AVKs

The center of a certain AVK should ideally be located at the respective target altitude. The part of the center vs. target altitude relation that is close to the line of origin (Fig. 4.5b) indicates therefore the altitude range where the retrieval works reasonably. A deviation from the line of origin has, however, to be seen in relation to the respective vertical resolution, which is discussed below (Sect. 4.3.1.3). For this purpose, the difference between corresponding center and target altitudes is shown normalized with the FWHM of the AVK in Fig. 4.5d.

For the normalized retrieval, this criterion is fulfilled between approximately 40 km and 80 km altitude, which defines the reasonable range in the normalized representation. The respective curve (Fig. 4.5b) for the vmr representation is, however, shifted to lower altitudes by about 4 km to 10 km up to an altitude of about 70 km and even more so at higher altitudes. This behavior is the result of an amplification of negative overshoots of the vmr AVKs and will be discussed further in Sect. 4.3.2. The deviation from the line of origin has to be considered in data analyses using the vmr representation; the altitude of observed features does not directly correspond to the geometric altitude in the atmosphere, but is shifted by a few kilometers to higher altitudes. This corresponds to 25 % to 50 % of the FWHM between 40 km and 60 km altitude (where the FWHM of the vmr representation is meaningful; Sect. 4.3.1.3) and is therefore still below the order of the vertical resolution. Above 70 km, however, the center altitude does not further increase with the target altitude so that the inclusion of this region in the vmr representation should be considered with care.

This behavior is connected to a special shape of the center vs. target altitude relation, in which the expected ambiguity of the linewidths (Sect. 4.2.5) emerges. This effect is

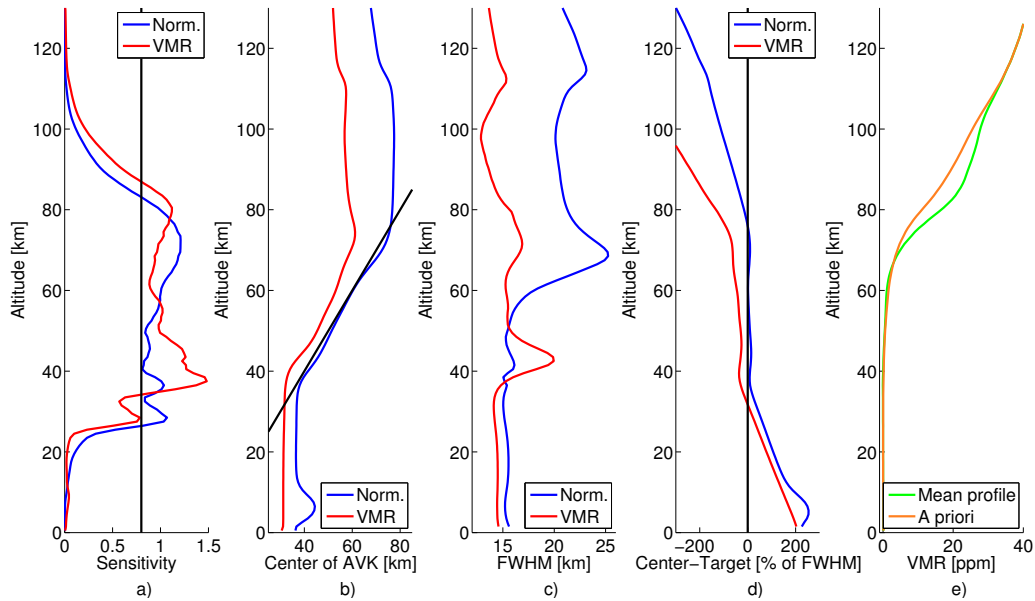


Figure 4.5: Retrieval characteristics averaged over the complete dataset shown for the normalized retrieval (blue) and the retrieval converted to vmr (red). **(a)** Sensitivity; the black solid line marks the threshold of 0.8, under which data are not considered to be reliable. **(b)** Altitude of the center of the AVKs. The black solid line marks the line of origin. **(c)** FWHM of the AVKs as a measure for the vertical resolution. Values for the vmr AVKs are not reasonable in all altitudes (see text for details). **(d)** The deviation of the curves in (b) from the line of origin normalized with the FWHM. **(e)** Mean profile of all retrieval results and the constant a priori. Figure adapted from Hoffmann et al. [2011].

also present in the normalized representation, but is there only relevant above 80 km altitude (Fig. 4.5b). First, the centers of the AVKs with target altitudes between 80 km and 110 km are constant at 80 km. Second, above 110 km the centers of the AVKs even decrease again down to about 68 km (normalized retrieval). The latter is actually explained by the ambiguity of the linewidths, causing the contributions from the highest considered altitudes to be attributed to the 70 km altitude range. In principle, this effect should also be present between 80 km and 110 km, but it is superimposed by the limited frequency resolution of the spectrometer. The relatively small change of the linewidth with altitude in this region cannot be resolved, so that all the contributions are attributed to a single altitude. Additionally, the slight deviation from the line of origin below 80 km in the normalized representation (Fig. 4.5b, blue line) can also be attributed to the ambiguity of the linewidths as counterpart of the resolved 110 km to 130 km region. In conclusion, the behavior of the center vs. target altitude relation is consistent with the expectations regarding the ambiguity of the linewidths (Sect. 4.2.5) under consideration of the spectral resolution of the instrument and the limited vertical resolution of the measurement. This finding is important as confirmation of a complete understanding of the retrieval properties. The influence on the actual retrieval results is, however, expected to be limited

to the upper few kilometers of the sensitive range. This aspect is taken up again in the comparison to satellite data (Chap. 5).

### 4.3.1.3 Vertical resolution

The FWHMs of the normalized retrieval are about 16 km between altitudes of 40 km and 57 km. They increase between altitudes of 57 km and 80 km with an average FWHM of 22 km. This suggests that the measurements provide two (and a fraction of a third) independent layers of information in the range of maximum sensitivity between 40 km and 80 km altitude. This is consistent with the degrees of freedom given by the trace of the AVK matrix (3.17 on average), considering that there is some remaining information outside of the 40 km to 80 km range.

Two maxima of the vertical resolution are found at 70 km and 115 km respectively, which can again be attributed to the expected ambiguity of the linewidths in this region (Sect. 4.2.5). The higher FWHMs at these altitudes represent the difficulty of attributing the contributions to a particular altitude since two options are possible. The comparatively lower FWHMs between the two maxima correspond again to the region in which the limited frequency resolution of the spectrometer overlays this effect.

The FWHMs for the vmr AVKs  $\mathbf{A}_{\text{vmr}}$  have to be handled with care since some AVKs show an oscillating shape for which the FWHM-concept is not appropriate. Whereas the FWHM values of 15 km to 20 km between 40 km and 60 km altitude can be regarded as a good indication for the real vertical resolution, the values above are not meaningful (Sect. 4.3.2). However, the trace of the AVK matrix does not depend on the particular realization of the AVKs. Hence it is also valid for the vmr representation  $\mathbf{A}_{\text{vmr}}$  and suggests independently from the FWHM concept that the vertical resolutions of both representations are comparable.

## 4.3.2 Individual AVK functions

The findings based on the average characteristics (Sect. 4.3.1) are exemplified and elaborated further with an individual set of AVKs. These AVKs correspond to the example retrieval result, which is discussed below (Sect. 4.4.1).

Figure 4.6 (left) shows a subset of normalized AVKs  $\mathbf{A}_{\text{norm}}$ , in which all interesting altitude ranges are represented:

- The range below the main sensitivity (below 40 km; black): the area of the AVKs increases with altitude, whereas all AVKs peak at the same altitude of 37 km.
- The range of main sensitivity (between 40 km and 80 km; green): the area of the AVKs is comparable and the AVKs peak at their respective target altitude, whereas the widths of the AVKs increase with altitude.
- The range above the main sensitivity where the spectrometer cannot resolve altitude information (between 80 km and 110 km; red): the area of the AVKs decreases with altitude, whereas all AVKs peak at about 80 km.

- The range above the main sensitivity where the spectrometer resolves the ambiguity of the linewidths (above 110 km; blue): the area of the AVKs is comparatively small. The peak altitude actually decreases with increasing target altitudes.

The normalized AVKs of all altitudes have slight negative overshoots, which is common for such retrievals.

Figure 4.6 (right) shows the corresponding vmr AVKs  $\mathbf{A}_{\text{vmr}}$ , converted using Eq. (4.2). It is obvious that the negative overshoots are much more pronounced here, giving particularly the upper vmr AVKs an oscillatory shape. This is explained by the shape of the CO profile that goes into the conversion: the calculation of the pure conversion factors (evaluation of Eq. (4.2) with the matrix of ones in place of  $\mathbf{A}_{\text{norm}}$ ; results shown in Fig. 4.7) reveals that all entries below the target altitude are amplified for each AVK, whereas the entries above the target altitude are diminished. As a result, the vmr AVKs with high target altitudes are strongly amplified by the conversion and formerly small negative overshoots get pronounced. This, in turn, affects partly the average AVK diagnostics (Sect. 4.3.1); the entries below the target altitude gain more weight, which shifts the centers of the AVKs downward. Furthermore, the FWHM-concept is partly not applicable anymore due to the stronger oscillatory shape of some vmr AVKs.

As a result, the overall appearance of the vmr AVKs does not look reasonable at first glance. This may cast doubts on the general retrieval performance, although the retrieval works adequately: first, the diagnostics directly related to the normalized retrieval result,  $\mathbf{A}_{\text{norm}}$ , are reasonable. Thus, particular data analyses and comparisons can be performed on the basis of normalized quantities, completely without consideration of the vmr AVKs. Second, a closer look at the vmr AVKs,  $\mathbf{A}_{\text{vmr}}$ , reveals that those AVKs in the range of 40 km to at least 70 km altitude are reasonable, although their center is shifted downwards by a few kilometers due to the stronger negative overshoot. Third, the impact of the pronounced oscillations of the vmr AVKs,  $\mathbf{A}_{\text{vmr}}$ , with higher target altitudes is mostly weak. Considering a vmr AVK that has a second (negative) peak below the main peak of similar absolute strength, the meaning of such an AVK is that a change of 1 ppmv in the true atmosphere at either the one or the other peak altitude has a similar influence on the retrieved value. However, looking at the CO profile, a change of 1 ppmv would be a much bigger relative change at the lower altitude in comparison to the higher altitude, and is much more unlikely.

### 4.3.3 A remark about the spectral resolution of the instrument

Although being in the right order of magnitude, the spectral resolution of the KIMRA FFTS (107 kHz) is theoretically not high enough to resolve the line differences of the emissions from altitudes between 70 km and 115 km as can be seen in Fig. 4.4. Since pressure broadening contributes significantly up to 80 km and it is technically possible to achieve higher frequency resolutions (e.g., with the FFTS described in Benz et al. [2005], which has a resolution of 60 kHz and better), the integration of such a spectrometer might be of interest to resolve the complete domain of pressure broadening.

It is, however, questionable if such an improvement of the instrument would actually lead to an improvement of the retrieval results in the particular case of CO since it is probably eliminated by the ambiguity of the linewidth (Sect. 4.2.5 and Sect. 4.3.1). The

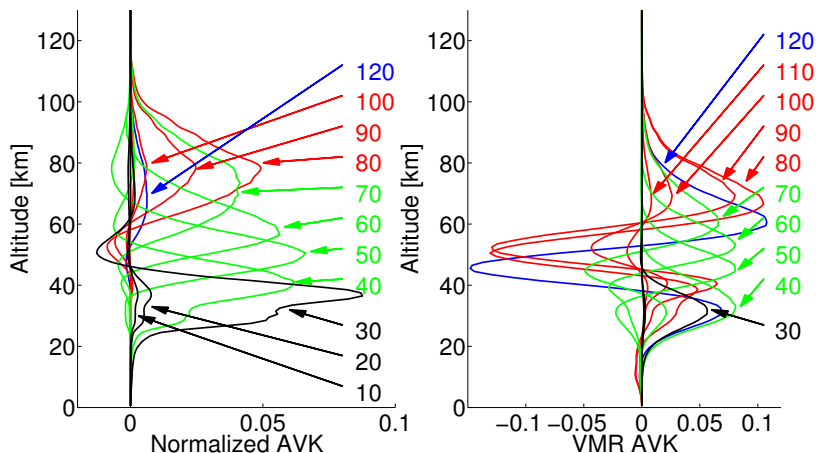


Figure 4.6: Selected AVK functions for the measurement of 29 October 2009, 06:52 h, for several altitudes. Different colors represent vertical ranges with different measurement characteristics. The target altitudes in km of the respective kernels are imprinted with arrows. The 120 km kernel (blue) was multiplied by a factor of 50 to make it visible in the given scale. **Left:** normalized AVKs. The 110 km AVK has been omitted since it is too small. **Right:** vmr AVKs. The 10 km and 20 km AVKs have been omitted for the same reason. Figure adapted from Hoffmann et al. [2011].

ambiguous counterpart of the 70 km altitude is located at about 115 km (Fig. 4.4) and has accordingly low sensitivity (Fig. 4.5a). However, the counterparts of the altitudes, which might be improved by a better spectral resolution, are located lower down (e.g., the 80 km altitude has its counterpart at approximately 100 km), such that their sensitivity has not dropped so much and may be still relevant.

On the one hand, it is therefore possible that the retrieval characteristics at the top of the sensitive range are slightly improved by a better frequency resolution. For example, the altitude at which the center vs. target altitude relation starts being a straight vertical line (Fig. 4.5b) might be shifted upwards by a few kilometers. On the other hand, the existence and value of such an improvement should be checked carefully in advance. In a first stage, a forward modeling study based on a better frequency resolution could be performed to examine if the retrieval relays the improvement to the result. After this, actual experiments still have to reveal if the improvement appears in the data measured under real conditions.

#### 4.3.4 Summary of retrieval performance

Since the presented retrieval characterization is comprehensive, it is concluded with the basic information, which is necessary to work with the retrieved dataset. The KIMRA CO retrieval works reasonably between 40 km and 80 km. At least two independent layers are retrieved in this region, corresponding to a vertical resolution of 16 km to 22 km. It is emphasized that this limited resolution has to be taken into account in the use and interpretation of the data (e.g., comparisons to other datasets) by considering the AVKs.

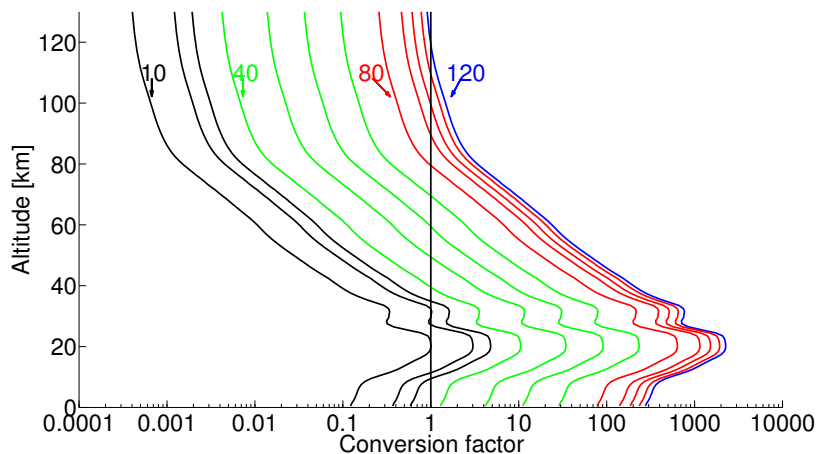


Figure 4.7: Selected altitude-dependent factors for the conversion from normalized AVKs to vmr AVKs. Single curves, the labeling, and the coloring correspond to the ones in Fig. 4.6. Hence, the curves belong to AVKs with target altitudes between 10 km and 120 km in 10 km steps from left to right. It is obvious that AVKs with high target altitudes are mainly amplified, whereas AVKs with low target altitudes are mainly diminished. Figure adopted from Hoffmann et al. [2011].

The AVKs together with the a priori are therefore an essential part of the dataset.

Note that two realizations of the AVKs exist,  $\mathbf{A}_{\text{norm}}$  corresponding to the normalized retrieval results and  $\mathbf{A}_{\text{vmr}}$  corresponding to the retrieval results transformed to vmr. Both realizations of the AVKs are generally equivalent as long as all quantities are consistently either normalized or not normalized. Mostly, the vmr representation,  $\mathbf{A}_{\text{vmr}}$ , appears more intuitive and natural, however, the region between 70 km and 80 km has to be handled with care in this representation.

## 4.4 Retrieval Results

### 4.4.1 A typical KIMRA CO retrieval result

The result retrieved from the spectrum measured on 29 October 2009, 06:52 h, is a typical example of the retrieved dataset in the sense that the values for the integration time and the elevation angle are close to the mean values of the complete dataset. This measurement serves consistently as an example in different parts of this work; the contributions to the line broadening are shown in Fig. 4.4, the respective AVKs in Fig. 4.6, and an error estimation in Fig. 4.11 (top).

The spectrum, which has been corrected for standing waves (Fig. 4.3, top), is fitted adequately by the retrieval process so that the residuum (Fig. 4.3, bottom) contains only noise contributions. The respective profile and the constant a priori together with two more example profiles are shown in Fig. 4.8. The profiles are plotted on the retrieval grid and over the full altitude range for a complete demonstration of the retrieval result, albeit the sensitive vertical range and the vertical resolution are restricted (Sect. 4.3). It is

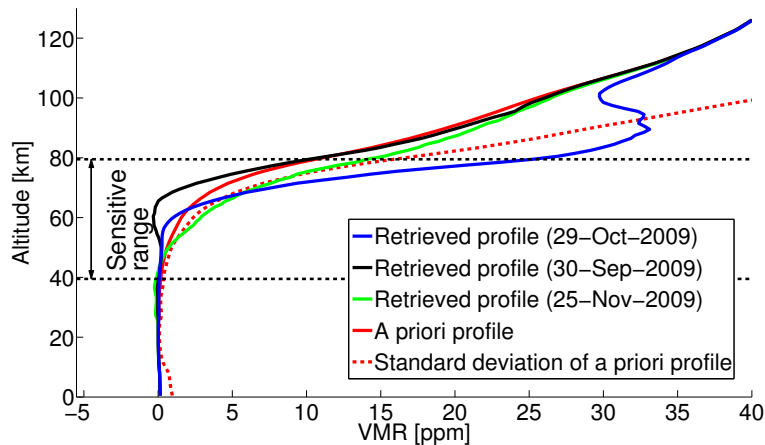


Figure 4.8: Retrieved CO profiles (selected to cover the complete range of the CO change during a winter), as well as the constant a priori profile and its assumed standard deviation represented by  $\sqrt{S_a^{ii} \cdot x_a^i}$ . The range of sensitivity of the KIMRA CO measurements (Sect. 4.3) is marked with black dashed lines. Outside this range, the profiles are not reliable, but are shown here for a complete demonstration of the retrieval results. Figure adopted from Hoffmann et al. [2011]

evident that the interesting part of the profile, the steep increase of CO in the mesosphere, is covered by the sensitive range. As expected, the retrieved profiles tend toward the a priori as the sensitivity above the meaningful range decreases.

Note that a small negative overshoot may be retrieved at the location of the transition from low CO to the steep increase (Fig. 4.8, black profile of 30 September 2009 at about 60 km). Although being apparently an unphysical result, this behavior is unproblematic since the vertical extent of the negative vmr is smaller than the vertical resolution of the measurement. Thus, it is an example for possible artifacts produced by the narrow retrieval grid as mentioned in Sect. 4.2.2.

#### 4.4.2 Complete retrieved KIMRA CO time series

The complete retrieved time series of KIMRA CO profiles, which constitutes the basis of the following chapters, is shown in Fig. 4.9. Note that it is shown on the retrieval grid for illustrative purposes, although the real vertical resolution is coarser (Sect. 4.3).

The descent of mesospheric air is easily identified qualitatively in fall 2009; the location of the strong vertical gradient is shifted downward by about 20 km (e.g., 75 km to 55 km for the 4 ppmv level) from mid September to mid November. The average descent velocity is therefore roughly estimated 300 m/d, which is in general agreement with previous studies (Sect. 2.4.3). It is elaborated further on the descent rate derivation in Chap. 7.

SSWs lead to a rapid decrease of the CO vmr (Sect. 2.4.2.3). The retrieved CO time series shows this behavior expectedly for two SSWs that occurred during the KIMRA measurement period at the end of January 2009 and 2010, respectively. The 2009 SSW has been analyzed in detail by Manney et al. [2009] and the KIMRA dataset, particularly

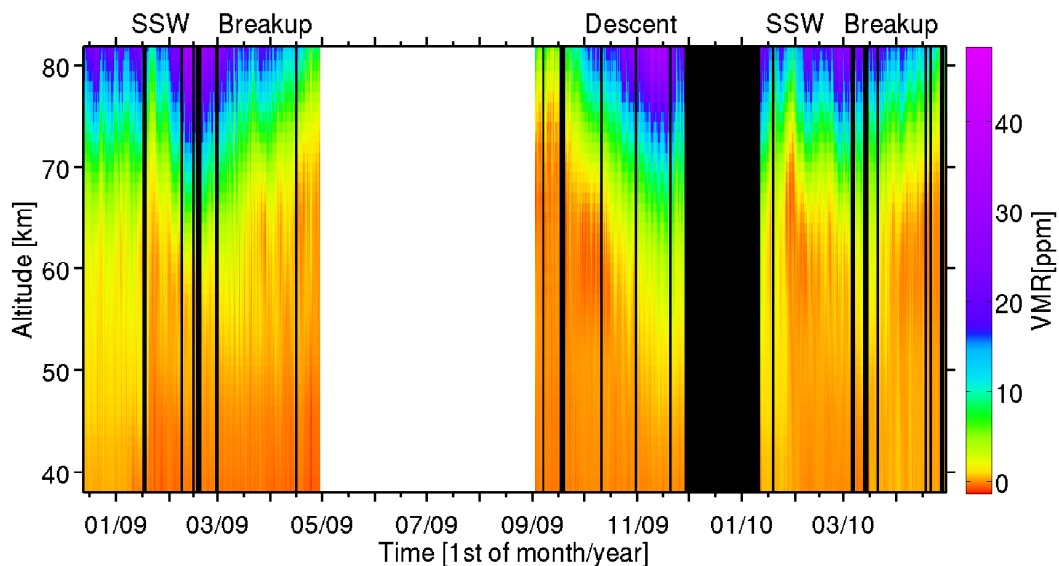


Figure 4.9: Time series of the retrieved KIMRA CO profiles, covering the complete analyzed period. All major features of the polar winter middle atmosphere dynamics are covered: the descent of air in fall 2009, the two SSWs in 2009 and 2010, respectively, as well as the breakups of the vortex in both winters. The black areas mark periods without measurements due to rainy weather or maintenance of the instrument. The white area marks the summer period from which CO measurements can generally not be retrieved reasonably. Note that the use of a logarithmic color scale is not appropriate here since the dataset contains slightly negative values (Sect. 4.4.1). Figure adapted from Hoffmann et al. [2011].

the timing of the SSW, is consistent with this study. The evolution of the 2010 SSW is generally consistent with a study by Pitts et al. [2011], which is, however, focused on the lower stratosphere. After the SSWs, when the vortex is reestablished, downwelling of air masses is observed again at the higher altitudes. The breakup, or final warming, of the vortex leads also to a decrease of the CO vmr (Sect. 2.4.2.3). This feature is clearly identified in the presented time series during spring 2009 and spring 2010.

To allow for a qualitative consistency check between independent measurements, the corresponding time series of the satellite instrument MLS is shown in Fig. 4.10. A detailed satellite comparison of time-averaged profiles, including a brief instrument description of MLS, is presented in Chap. 5. Additionally, the MLS dataset is also included in a time series analysis in Chap. 6. Here, the main intention is to visualize that all the major features described above are consistently measured by both instruments. Furthermore, the KIMRA dataset shows more variability on short timescales, whereas the MLS time series looks smoother. This is explained by the averaging, which has to be applied to the collocated MLS profiles; all MLS profiles within a distance of 500 km around Kiruna were selected, convolved with the KIMRA AVK functions using Eq. (3.31), and then averaged daily.

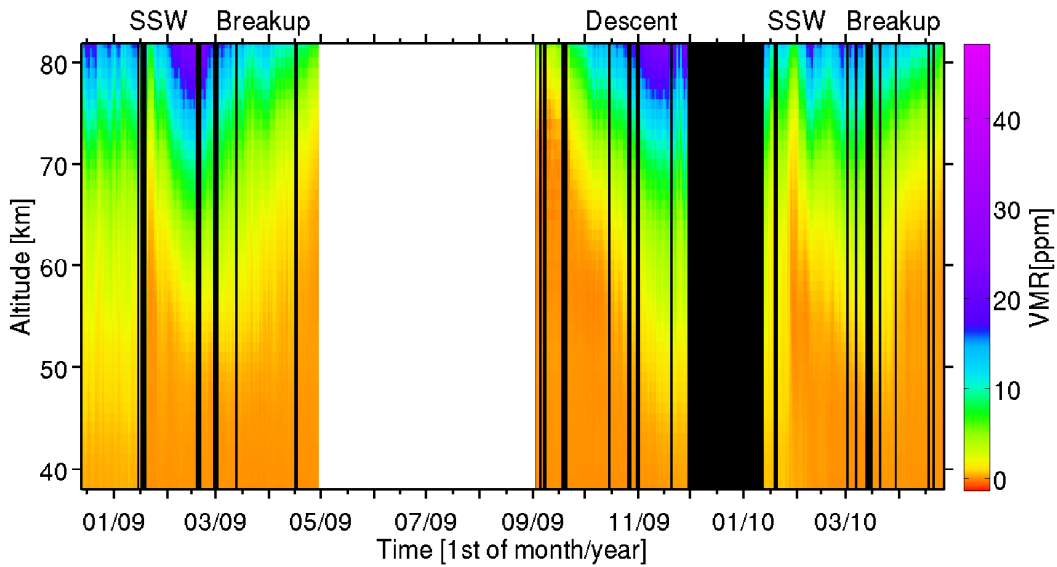


Figure 4.10: Time series corresponding to Fig. 4.9, but measured by the MLS satellite instrument, showing that all major features are contained similarly in both datasets. To improve the visual comparability, similar measurement gaps as for the KIMRA dataset are indicated, although MLS may provide measurements during these periods. Collocated profiles within a distance of 500 km around Kiruna were selected, convolved with the KIMRA AVKs and averaged daily. Figure adapted from Hoffmann et al. [2011].

## 4.5 Error estimation

### 4.5.1 Setup of the error estimation

The error of a retrieved profile has been estimated according to Sect. 3.3.3, considering contributions from five different forward model parameters. The first three ( $\sigma_{S_{fi}}$ ,  $\sigma_{\gamma_a}$ , and  $\sigma_{n_a}$ ) belong to the main spectroscopic parameters, specifically the line intensity  $S_{fi}$ , the pressure broadening parameter  $\gamma_a$  and its temperature dependency parameter  $n_a$  (Sect. 3.1.2; see Bühler et al. [2005] and references therein for exact definitions and the implementation in the forward model). Furthermore, the contribution  $\sigma_T$  from the uncertainty of the used temperature profiles as well as the contribution  $\sigma_{T_C}$  from a possible calibration error of the absolute spectrum have been included. Considering also the error caused by the measurement noise  $\sigma_\eta$  (Sect. 3.3.3), the total error is given by

$$\sigma_{\text{tot}}^i = \sqrt{(\sigma_{\gamma_a}^i)^2 + (\sigma_{n_a}^i)^2 + (\sigma_{S_{fi}}^i)^2 + (\sigma_T^i)^2 + (\sigma_{T_C}^i)^2 + (\sigma_\eta^i)^2}. \quad (4.3)$$

The derivation of the underlying uncertainty values is explained in the following; the values are summarized in Table 4.2.

The HITRAN catalog is generally used for estimates of the uncertainties of the spectroscopic parameters. The uncertainty for the line intensity  $S_{fi}$  is given with a value lower than 1%. However, a comparison with the respective value in the Jet Propulsion Laboratory (JPL) catalog [Pearson et al., 2010] reveals a discrepancy of about 2%, so

Table 4.2: Considered error contributions from forward model parameters. See text for further justification.

Quantity	Used uncertainty	Reason	Reference
Line intensity $S_{fi}$	2%	Deviation of quantities in catalogs HITRAN and JPL	Rothman et al. [2005]; Pearson et al. [2010]
Pressure broadening $\gamma_a$	2%	Maximum error given in HITRAN	Rothman et al. [2005]
Temperature dependency $n_a$	5%	Maximum error given in HITRAN	Rothman et al. [2005]
Temperature profile $T$ below 80 km	5%	Mismatch of measurement locations	
Temperature profile $T$ above 100 km	10%	Mismatch of measurement locations	
Temperature profile $T$ in between	interpolated from 5% to 10%	Mismatch of measurement locations	
Calibration error	2K	Conservative estimation including possible side effects	

that this value is used instead. The other spectroscopic parameters are not covered by the JPL catalog.

For the error on the used SABER temperature profiles (Sect. 4.2.3), it is not enough to consider the given uncertainty for a single profile since the effect of the locational mismatch of the satellite measurements has to be included. This could be addressed by taking the standard deviation of the averaged collocated profiles into account. However, another complication comes from the fact that this box is filled only at the southern edge every 60 days (Sect. 4.2.3), which may introduce an additional systematic error. The maximum uncertainty, which has to be expected from the temperature profiles, has therefore been estimated by checking several configurations of collocated profiles (comparison of a complete box during the north-viewing mode phase with a subset of these profiles south of  $52^\circ$  N, a comparison of a north viewing mode phase (October 2009) with a real south-viewing mode phase (December 2009), as well as the standard deviations in these boxes). The individual tests showed uncertainties of a similar order of magnitude and a rough estimation of the maximum errors has been derived from these values.

A conservative estimate of the calibration error of the absolute spectrum is in the order of 2 K. The tolerance of the adjustable reference load is about one order of magnitude lower. In the sense of a rough estimation of the maximum uncertainty, however, side effects like, e.g., a possible temperature drift, were included in this larger error.

## 4.5.2 Results of the error estimation

The single contributions to the total error may differ from spectrum to spectrum, which is expected because of the varying SNR (Sect. 4.1.3). However, the following general statements can be made (examples are shown in Fig. 4.11):

- According to the shape of the CO profile, the total error  $\sigma_{\text{tot}}$  increases strongly with altitude. It is approximately 0.1 ppmv at 50 km and approximately 3 ppmv at 80 km altitude.
- The dominating contributions to the total uncertainty  $\sigma_{\text{tot}}$  are the noise error  $\sigma_\eta$  and the temperature error  $\sigma_T$ .
- Frequently, the spectroscopic contribution  $\sigma_{S_{fi}}$  shows a peak of a few tenths of a

ppmv at approximately 60 km altitude, which is strong enough to dominate the total uncertainty  $\sigma_{\text{tot}}$  in this altitude (Fig. 4.11, bottom).

- The other spectroscopic contributions as well as the calibration error are negligible.
- The error  $\sigma_{S_{\text{fi}}}$  is systematic and also  $\sigma_{\text{T}}$  may have a systematic nature since it can be caused by a southward bias of the collocated SABER temperature profiles. This means that a reduction of the total error  $\sigma_{\text{tot}}$  by averaging over a subset of KIMRA profiles can only be achieved as long as the noise error  $\sigma_{\eta}$  dominates. In this sense, these systematic contributions define the lower limit of the total error, which can be achieved by the averaging of KIMRA profiles.

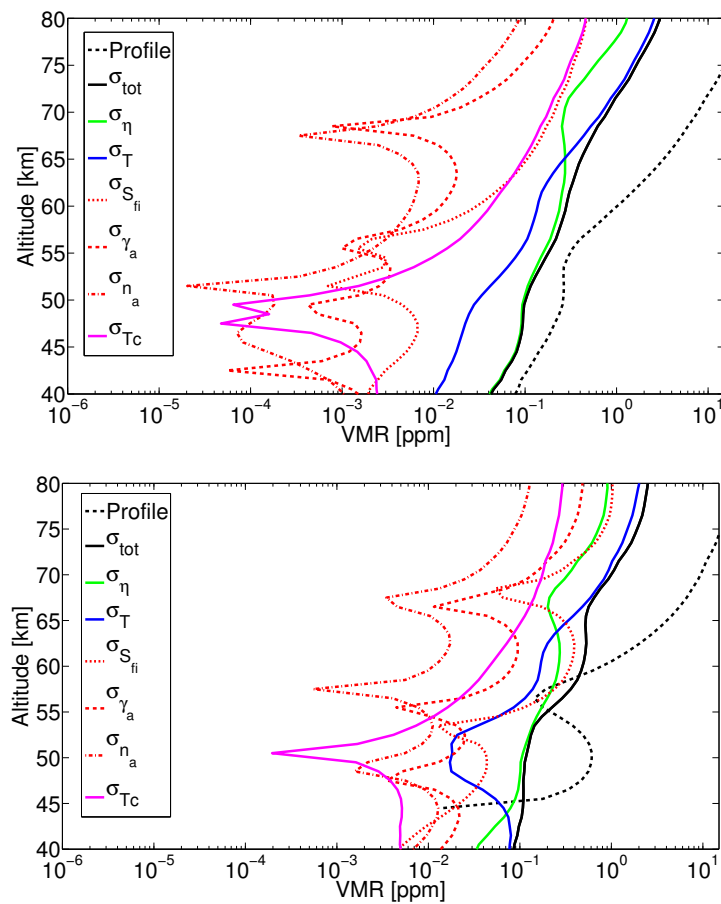


Figure 4.11: Typical examples of error contributions. The dominating contributions to the total error  $\sigma_{\text{tot}}$  come from the measurement noise error  $\sigma_{\eta}$ , from the temperature error  $\sigma_{\text{T}}$ , and frequently from the spectroscopic error  $\sigma_{S_{\text{fi}}}$ . For comparison, the corresponding vmr profiles are also included (black dashed lines). **Top:** standard example of 29 October 2009 (Sect. 4.4.1), which has no dominating spectroscopic contribution. **Bottom:** example of 4 February 2009, which shows a pronounced spectroscopic contribution at 60 km. Figure adapted from Hoffmann et al. [2011].

### 4.5.3 Variation of the a priori

In addition to the error analysis based on the standard retrieval theory, an experiment with different CO a priori profiles was carried out to investigate the influence of the a priori on the retrieval result independently from the AVK discussion (Sect. 4.3). For this purpose, the standard a priori (Sect. 4.2.3) was reduced (alternatively raised) by 50 % constantly over the full altitude range, whereas the a priori covariance  $\mathbf{S}_a$  in absolute units was kept constant. The complete dataset was retrieved with these modified setups. For the identification of systematic effects, total average profiles over the three different datasets (Fig. 4.12, top) together with the deviations from the standard results (Fig. 4.12, bottom) were calculated. In addition, the partial columns of CO between 40 km and 80 km were compared.

The results from the modified setups slightly oscillate around the standard profile in the range of the main sensitivity. Outside this range, the deviation approaches the original magnitude of 50 %, as expected. In conclusion, an alternative choice of the a priori may introduce a systematic bias of about 6 % on average (for details see Table 4.3) in the range of main sensitivity on the basis of a 50 % change of the a priori.

Table 4.3: Details of the a priori influence experiment, valid for the vertical range of the main sensitivity between 40 km and 80 km altitude.

Modification of a priori	+50 %	-50 %
Min. deviation	-12 %	-8 %
Max. deviation	+13 %	+10 %
Mean abs. deviation	8 %	4 %
Mean deviation	1 %	1 %
Partial col. deviation	4 %	-0.3 %

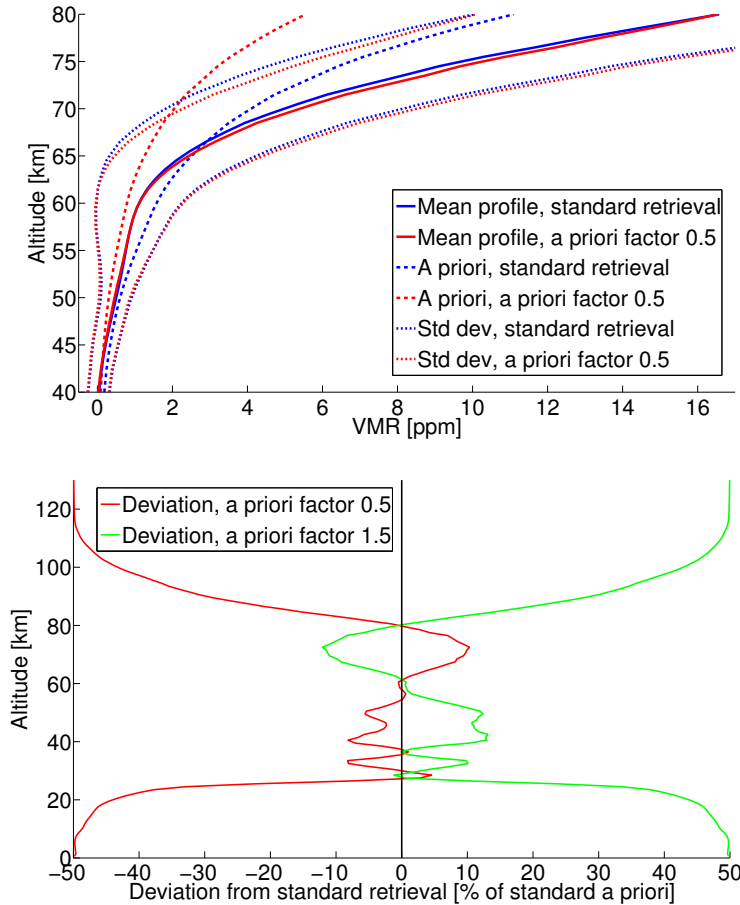


Figure 4.12: Test of the retrieval stability when the a priori is modified by a factor of 0.5 or 1.5 respectively. **Top:** mean profiles, associated standard deviations, and a priori profiles for the standard retrieval and one modified retrieval setup (factor 0.5) in the range of sensitivity between 40 km and 80 km. It is obvious that the change of the mean profile introduced by an a priori change is much smaller than the standard deviation, which is mainly produced by the annual variability. Profiles of the factor 1.5 case behave similarly and are not shown. **Bottom:** deviation of the mean profiles of both modified cases from the standard retrieval profile, plotted for the complete vertical range and normalized with the standard a priori. The deviation is small in the range of sensitivity between 40 km and 80 km and approaches, as expected, 50% where the sensitivity vanishes completely. Figure adopted from Hoffmann et al. [2011].

## 4.6 Summary

The retrieval of vertical CO profiles from microwave spectra obtained with the ground-based instrument KIMRA has been presented. This instrument is located in Kiruna, northern Sweden (67.8° N, 20.4° E). It measures the CO emission line at 230 GHz continuously from September to April during each winter. Here, spectra of the first two winters (2008/2009 and 2009/2010) with operational measurements have been retrieved. This dataset includes approximately 1500 spectra with a mean integration time of 1 h.

The CO vmr profiles have been retrieved using the OE approach. The a priori profile as well as the a priori covariance matrix needed for this approach have been kept constant for the complete period, so that the variations with time of the retrieved profiles come certainly from the measurements.

A detailed analysis of the AVK functions has revealed that the KIMRA CO retrieval provides information between 40 km and 80 km. At least two independent layers are retrieved in this region, corresponding to a vertical resolution of 16 km to 22 km. It is emphasized that this limited resolution has to be taken into account in the use and interpretation of the data by considering the AVKs. The AVKs together with the a priori are therefore an essential part of the dataset.

Furthermore, the AVKs show contributions in the received signal from up to 130 km altitude. The reason for this is the special shape of the CO vmr profile, which steeply increases toward the thermosphere. It was shown that this residual thermospheric signal leads to a complication of the retrieval; the strongly increasing temperature in the thermosphere leads to a stronger Doppler broadening of the line contributions from these altitudes. This results finally in an ambiguity of mesospheric and thermospheric linewidths. The effect of this behavior has been identified in the AVK characteristics and it has been emphasized that the absolute vmr values from the 70 km to 80 km altitude range have to be handled with care. However, this complication is not expected to significantly affect the analyses of temporal CO variability, which is of major interest for the investigation of dynamics.

Potential errors of the retrieved profiles arising from different sources in the measurement and retrieval process have been assessed. It has been found that the total error increases with altitude from approximately 0.1 ppmv at 50 km altitude to approximately 3 ppmv at 80 km altitude. The main contributions to the total error arise from the noise on the spectra and the uncertainty of the used temperature profiles. Frequently, the error at about 60 km altitude is dominated by the uncertainty of the line intensity used for the forward model calculation.

It has been shown qualitatively that the retrieved time series of CO profiles contains all dynamical features, which are of major interest in the polar winter middle atmosphere: the descent of mesospheric air in fall 2009, the SSWs in 2009 and 2010, as well as the breakups of the vortex in both years. These features are, furthermore, qualitatively consistent with observations from the satellite instrument MLS.

In conclusion, the retrieval of the KIMRA CO time series performed in this work provides an independent set of observations related to the polar winter middle atmosphere dynamics, which is available for atmospheric analyses. It is particularly the basis for the following studies in the present thesis: a comparison of time-averaged profiles with satellite datasets (Chap. 5), a validation of the polar dynamics in state-of-the-art model (Chap. 6),

and the derivation of the descent rates of mesospheric air (Chap. 7).

Aside from the direct application of the presented CO time series, the developed retrieval setup will be used to retrieve CO from the continued KIMRA measurements. Furthermore, the gained experience will be beneficial for the intended development of a further CO microwave radiometer, for which large parts of the developed retrieval setup will be reused [personal communication with Mathias Palm, University of Bremen].



# 5 Comparison of time-averaged CO profiles from KIMRA and satellites

Large parts of this chapter are based on Hoffmann et al. [2011].

One important application of ground-based observations is the intercomparison with satellite data to investigate the agreement between independent observation techniques in certain regions. A basic approach is the comparison of profiles averaged over a longer time period. Whereas this approach examines the general consistency of the derived profiles under a low noise influence, an additional time-resolved comparison of CO variations is directly related to the questions concerning dynamical variability (Chap. 2). The CO time series will be applied in this respect below and a time dependent satellite comparison is implicitly included in the conducted model validation (Chap. 6). However, the general agreement of the temporal CO evolution observed by KIMRA and the satellite instrument MLS was already qualitatively demonstrated in Sect. 4.4.2 (Fig. 4.9 and Fig. 4.10).

Despite both the importance of consistency checks between independent observations techniques and the number of CO observations previously performed (Sect. 2.4.3), the satellite comparison conducted in this study (which was initially published by Hoffmann et al. [2011]), is the first such comparison incorporating the ground-based microwave technique, particularly in polar regions. The only exception is the satellite validation of the ACE-FTS CO product [Clerbaux et al., 2008], in which data of one ground-based microwave radiometer, located in the mid-latitudes, was considered. However, only two collocated profiles were found in this study. Indeed, properties of both the polar region and the microwave technique cause special difficulties in such a comparison of polar CO:

- The CO vmr in this region shows strong horizontal gradients (Sect. 2.4.2.2), so that the choice of tight collocation criteria is expected to be particularly important.
- In contrast to the first point, the polar coverage of some satellite instruments is, especially during polar night, sparse, which demands for relaxed collocation criteria.
- Although the upper limit of reasonable information of the KIMRA measurements is approximately 80 km, there is some residual sensitivity up to 130 km (Sect. 4.3.1.1), where also the available satellite datasets cannot provide reasonable information anymore. Due to the limited vertical resolution of the KIMRA measurements (considered by smoothing with the KIMRA AVKs), however, the profile parts of this region may also affect the comparison in the range of interest below 80 km.

Nevertheless, the KIMRA dataset is related here to the datasets of all three satellite instruments that provide data for the period of KIMRA measurements. Large parts of this chapter are based on Hoffmann et al. [2011]. However, the comparison method has been slightly modified (Sect. 5.1). Thus, the results presented in this work represent an update of those published before.

Note that all three satellite instruments use different measurement techniques. Although being not the main motivation, another outcome of this study is a rough comparison of the satellite instruments with each other. Therefore, it is an addition to the satellite intercomparisons included in the extensive validation studies [e.g., Pumphrey et al., 2007; Clerbaux et al., 2008] in the sense that this comparison is focused spatially on an area around Kiruna. However, it is also restricted to the coarse vertical resolution of the KIMRA instrument, so that smaller vertical structures cannot be compared.

## 5.1 Computation of time-averaged profiles

The procedure with which comparable time-mean profiles of the individual datasets are derived is described in the following. First, the original satellite profiles are sorted according to the following collocation criteria:

- Area: circle around Kiruna with the radius  $r_{\text{coll}}$ .
- Period: profiles have to be measured on the same day to be considered comparable throughout this study.
- Deviation of PV: it is ensured with this criterion that only measurements of similar air masses are considered (Sect. 2.2.3). The PV is calculated from ECMWF Operational Analysis wind fields in 40 km, 50 km, and 60 km altitude. The deviation

$$\Delta P(z) = \frac{P_{\text{Kiruna}}(z) - P_{\text{Sat}}(z)}{P_{\text{Kiruna}}(z)} \quad (5.1)$$

may not exceed a given threshold in any of the altitudes for the profile to be considered. A similar approach has been applied before by Clerbaux et al. [2008].

The selected profiles are interpolated to the KIMRA retrieval grid, on which the analysis is performed.

As explained above, information from the unreasonable parts of the satellite profiles may affect the comparison in the interesting vertical range. To avoid that physically implausible values are considered, the upper parts of the satellite profiles are replaced with the KIMRA a priori before the convolution with the KIMRA AVKs. This may, in turn, artificially improve the mutual agreement between the satellite datasets in the upper part, so that the considered altitude range has still to be restricted to a lower top altitude than it would nominally be possible (Table 5.1). The modified satellite profiles are convolved with the respective KIMRA AVK functions (Eq. 3.31) using the vmr AVK functions  $\mathbf{A}_{\text{vmr}}$  of the closest KIMRA measurement for each satellite profile.

The next step, in which daily averages from the convolved profiles are computed, results in a time series of one profile per day and dataset. However, individual datasets may still have gaps due to the collocation criteria or a lack of measurements. Such periods with a gap in at least one of the datasets are removed from all other datasets. Hence, the resulting time series contains only days with at least one measurement in every single dataset, which minimizes a possible bias due to different periods in the average. In contrast to the comparison by Hoffmann et al. [2011], the averages are computed using a standard mean instead of a weighted mean with inverse standard deviations as weights. Although the

weighted mean should in theory result in a more precise average profile, its use turned out to be disadvantageous; the estimated standard deviations of the individual datasets are noisy and the weighted mean transfers this noise to the average profile, actually reducing its conclusiveness.

In the last step, these preprocessed time series are averaged to produce the final mean profiles  $\overline{\chi}_{\text{CO}}^{\text{Sat}}$  and  $\overline{\chi}_{\text{CO}}^{\text{KIMRA}}$ , with ‘Sat’ referring to the respective satellite dataset. Aside from these profiles themselves also the deviation

$$\Delta\chi_{\text{CO}} = \overline{\chi}_{\text{CO}}^{\text{Sat}} - \overline{\chi}_{\text{CO}}^{\text{KIMRA}} \quad (5.2)$$

is evaluated. Note that a possible normalization of this deviation with the KIMRA profile  $\overline{\chi}_{\text{CO}}^{\text{KIMRA}}$  is not insightful. The strong gradient of the CO profile as well as profile values close to zero (Sect. 4.4.1) produce large values and thus a bumpy curve, which is difficult to interpret. Note further that the standard deviation of the time-averaged profiles is dominated by the strong temporal variability of the CO vmr during winter and thus represents not a useful measure for the measurement uncertainty of the respective datasets.

## 5.2 Satellite datasets

All three satellite instruments, which provide CO data for the evaluated KIMRA period, MLS, ACE-FTS, and MIPAS (Sect. 2.4.3), are considered in this comparison; basic properties are summarized in Table 5.1.

MLS (Microwave Limb Sounder) flies on the Aura satellite in a sun synchronous polar orbit and measures microwave emission in limb viewing geometry [Waters et al., 2006]. The CO dataset [Pumphrey et al., 2007] provides by far the largest numbers of possible coincidences. Therefore, the tightest collocation criteria are applied for MLS and, furthermore, the influence of relaxing these criteria is studied using MLS. However, the reasonable vertical range after the AVK convolution (upper limit 70 km) does not cover the full KIMRA range (Sect. 5.1).

ACE-FTS (Atmospheric Chemistry Experiment – Fourier Transform Spectrometer) is an infrared Fourier transform spectrometer, measuring atmospheric absorption in solar occultation mode [Clerbaux et al., 2008]. This technique produces high quality profiles, but only a small number of possible coincidences, so that relaxed collocation criteria have to be used. Nevertheless, the ACE-FTS comparison is interesting because of the good vertical coverage, which includes the full KIMRA range also after the convolution with the KIMRA AVKs.

MIPAS (Michelson Interferometer for Passive Atmospheric Sounding) onboard the Envisat satellite is also a Fourier transform spectrometer but measures atmospheric infrared emission in limb viewing geometry. Relevant measurements are generally performed in three different modes, covering different vertical ranges. CO data of the MIPAS nominal mode (MIPAS NOM) and the MIPAS middle atmosphere mode (MIPAS MA) have been made available for the present work by Bernd Funke (Instituto de Astrofísica de Andalucía (IAA), CSIC, Granada, Spain). MIPAS upper atmosphere mode (MIPAS UA) CO data are generally unavailable so far. The MIPAS NOM dataset provides more possible collocations, but allows for reasonable comparisons only up to 60 km altitude. MIPAS

MA observations are only conducted every 10th day, so that the dataset provides a limited number of collocations, but with full vertical coverage, similar to ACE-FTS. MIPAS CO data versions used in this study (V4O\_CO\_200 and V4O\_CO\_501 for MIPAS NOM and MIPAS MA observations, respectively, generated by IMK/IAA) are based on version V3O\_CO\_9+10 [Funke et al., 2009] with some minor modifications related to a changed spectral resolution of the instrument since 2005.

### 5.3 Comparison with MLS

The dense MLS dataset allows for the tightest collocation criteria in this study ( $r_{\text{coll}} = 50$  km,  $\Delta P = 5\%$ ) for which 29 days with coincidences are found (Fig. 5.1, red dashed curve; see Table 5.2 for an overview of all experiments). Generally, KIMRA shows lower values than MLS below 67 km. This bias is smaller than 0.2 ppmv below 55 km and maximal at 62 km with 0.5 ppmv, which partly exceeds the estimated systematic error contributions for the KIMRA dataset (Sect. 4.5.2). Contrarily, above 67 km the deviation turns into an increasing high bias for KIMRA with a maximum deviation of  $-0.3$  ppmv at 70 km altitude.

The shape of the deviation shows an oscillatory structure between 40 km and 65 km, representing a systematic difference of the profile shapes of KIMRA and MLS; the MLS profile is more curved, whereas the KIMRA profile shows a weaker increase of CO with altitude up to about 65 km and a stronger increase above, which then results in the high bias towards 70 km altitude. This difference of the profile shapes can be recognized more or less pronounced in all comparisons in the following.

#### 5.3.1 Influence of the collocation criteria

Figure 5.1 also shows averages of MLS profiles, collocated in circles with different radii  $r_{\text{coll}}$  around Kiruna. First, no PV criterion was applied (solid curves), whereas second, only profiles in the respective area with  $\Delta P < 5\%$  were selected (dashed curves). Generally, the profile shape deviation is obvious for all cases. Applying the area criterion alone reveals that the difference between KIMRA and MLS is increased between 45 km and 65 km by relaxing  $r_{\text{coll}}$ . This behavior appears plausible since CO increases non-linearly toward the winter pole in the vicinity of the horizontal CO gradient associated with the

Table 5.1: Properties of the satellite datasets considered in this study.

Dataset	Technique	Version	Nominal limit [km]	Used limit [km]	No. of profiles	Reference
MLS	microwave, limb	3.3	$\approx 85$	70	24682	Pumphrey et al. [2007]; Livesey et al. [2011]
ACE-FTS	infrared, solar occul.	3.0	$\approx 95$	80	168	Clerbaux et al. [2011]
MIPAS NOM	infrared, limb	V4O_CO_200 (IMK/IAA)	$\approx 70$	60	2451	Funke et al. [2009]
MIPAS MA	infrared, limb	V4O_CO_501 (IMK/IAA)	$\approx 95$	80	72	unpublished data

Table 5.2: Summary of the satellite comparison experiments.

Experiment	$r_{\text{coll}}$ [km]	$\Delta P$ [%]	Period	Days	Figure
<b>Area (MLS)</b>					Fig. 5.1
	50		complete	40	
	200		complete	215	
	1000		complete	300	
	50	5	complete	29	
	200	5	complete	101	
	1000	5	complete	157	
<b>PV (MLS)</b>					Fig. 5.2
	1000	5	complete	157	
	1000	10	complete	270	
	1000	20	complete	293	
	1000	50	complete	300	
<b>Period (MLS)</b>					Fig. 5.3
High CO 2008	200	5	15 Dec 2008–15 Jan 2009	6	
High CO 2009	200	5	1 Nov 2009–30 Nov 2009	9	
Low CO 2009	200	5	1 Apr 2009–30 Apr 2009	14	
Low CO 2010 (SSW)	200	5	29 Jan 2010–28 Feb 2010	7	
Low CO 2010	200	5	1 Apr 2010–30 Apr 2010	9	
<b>Multi Instrument</b>					
MIPAS NOM, MLS	250	20	complete	42	Fig. 5.4
ACE-FTS, MLS	1000	20	complete	22	Fig. 5.5
MIPAS MA, MLS	1000	20	Jan 2009–Apr 2009	9	Fig. 5.6
ACE-FTS, MIPAS MA, MLS	1000	50	18 Mar 2009	1	Fig. 5.7

vortex boundary (Sect. 2.4.2). A widening of the collocation area in meridional direction puts therefore more weight on higher CO values and leads to an increasing average MLS profile.

If the allowed PV deviation is additionally restricted, this relation is not clearly identified anymore. It is still valid below 57 km, but actually reversed above. For example, the agreement above this altitude is better for  $r_{\text{coll}} = 1000$  km and  $\Delta P < 5\%$  than for  $r_{\text{coll}} = 50$  km and  $\Delta P < 5\%$ . The reason for this is unclear, but it might be connected to the altitude dependence of both the horizontal CO gradient and the mixing barrier at the vortex edge (Sect. 2.2.3). However, applying the PV criterion reduces strongly the number of coincidences. This particular finding might therefore not be robust, although the comparatively dense MLS dataset was used here. Nevertheless, it is obvious that the profile shape deviation of KIMRA dominates over the influence of the collocation criteria above about 55 km altitude.

Figure 5.2 shows the resulting profiles and deviations of a similar experiment. Here, the PV criterion was varied, whereas the area criterion was held constant on its maximum level with  $r_{\text{coll}} = 1000$  km. Again, the deviation of the profile shape is similar. The high bias for MLS is also increased by relaxing the  $\Delta P$  threshold from 5%, but only between 55 km and 65 km altitude, whereas the other altitudes are hardly affected. Furthermore, a  $\Delta P$  threshold of more than 10% rejects only a small number of profiles in the collocation area. Hence, the results obtained for different values of  $\Delta P$  greater than or equal to 10% do not differ much, whereas the 5% threshold reduces the deviation between KIMRA and MLS. The reason for the altitude-dependence of this influence is also unclear, but might similarly be connected to the altitude-dependence of the mixing barrier at the vortex edge.

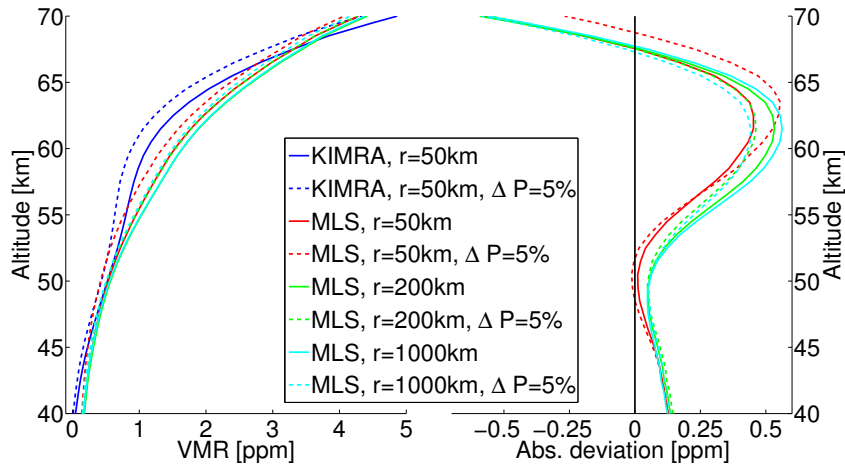


Figure 5.1: Comparison of KIMRA and MLS using the tightest collocation criteria throughout this study (blue and red dashed curves) and, moreover, the investigation of the influence of the collocation area using the MLS dataset. In the first case (solid lines) only the area criterion with different  $r_{\text{coll}}$  was applied. In the second case (dashed lines) a PV threshold of  $\Delta P = 5\%$  was additionally applied. **Left:** mean profiles. KIMRA profiles are only shown for the tightest collocation criteria since their sensitivity to a criterion change is low (a dependency only exists if the averaged period changes as result of a criterion change). **Right:** deviation  $\Delta\chi_{\text{CO}}$  between the KIMRA and the satellite profiles.

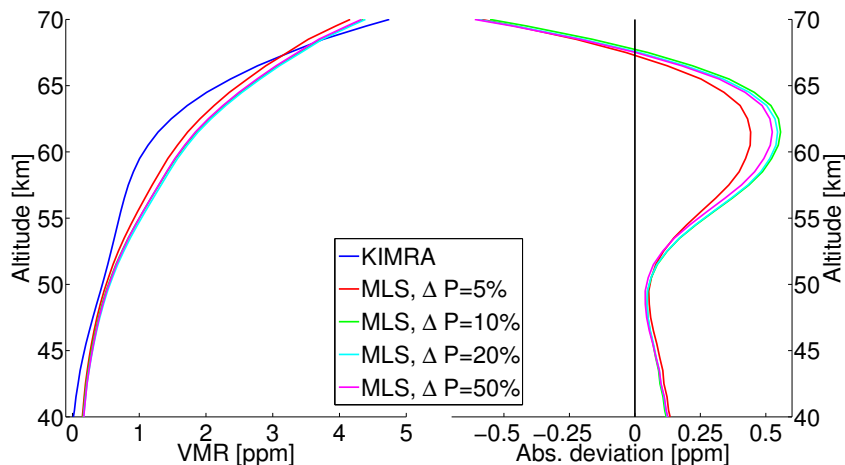


Figure 5.2: Investigation of the influence of the PV collocation criterion using the MLS dataset in a constant radius of  $r_{\text{coll}} = 1000$  km. **Left:** mean profiles. **Right:** deviation  $\Delta\chi_{\text{CO}}$  between the KIMRA and the satellite profiles.

### 5.3.2 Influence of the measurement period

It was checked with this experiment if the observed deviation of the KIMRA profile shape depends on the evaluated period, i.e., on the amount of CO during the measurements. In addition to the collocation criteria  $r_{\text{coll}} = 200$  km and  $\Delta P < 5\%$ , five periods were chosen, for which average profiles were calculated: two periods of high CO after the fall descent in both winters, as well as three periods with low CO after the final warmings in both winters and after the SSW 2010 (Table 5.2).

Although the numbers of coincidences for the single cases are small, the profile shape deviation is by tendency common to all periods (Fig. 5.3). The experiment indicates additionally that the oscillatory pattern is vertically shifted by a few km between high and low CO periods. This can be seen by looking at the individual maximum of the deviation, which is below 63 km for the high CO cases and above this altitude for the low CO cases. This behavior appears plausible since the high CO scenarios are produced by a downward transport of CO, which roughly also shifts the CO profile and its properties to lower altitudes. However, this shift is of minor importance when taking the vertical resolution of the KIMRA observations into account (about 17 km in this region, Sect. 4.3.1).

## 5.4 Multi-instrument comparison

The extension of the comparison to the other satellite datasets is difficult since relaxed collocation criteria have to be chosen (Table 5.2). According to the findings of the collocation experiments, this should not be problematic for the identification of the profile shape deviation with respect to other datasets. However, it could complicate the identification of slighter biases apart from the profile shape deviation. Furthermore, despite this relaxation the number of days with coincidences still remains low, so that effects of the small sample size cannot be excluded. Since the dense MLS dataset does not restrict the number of days with coincidences, it is included the following comparisons as reference.

After MLS, the MIPAS NOM dataset provides the most collocations with moderate collocation criteria. The comparison is, however, restricted to 40 km to 60 km altitude (Fig. 5.4). In this region, MIPAS NOM shows, first, the same oscillating deviation from KIMRA as MLS. Thus, the profile shape is consistent among both satellite datasets and similarly different from KIMRA. Second, the deviation with respect to MIPAS NOM oscillates around zero, whereas the deviation with respect to MLS is generally positive, showing that the absolute values in a vertical mean sense of KIMRA and MIPAS NOM agree better than KIMRA and MLS.

Taking also ACE-FTS and MIPAS MA into account (Figs. 5.5, 5.6, and 5.7), which cover the complete KIMRA altitude range, it is obvious that KIMRA shows a high bias above 70 km, which was already indicated by the comparison to MLS alone (Sect. 5.3). Here, it can additionally be seen that this bias increases strongly with altitude. Furthermore, the profile shape deviation of KIMRA is also apparent with respect to these datasets. Apart from this shape deviation, the KIMRA CO vmr is consistent with the vmr of the satellite datasets below 65 km altitude in the following sense: differences between KIMRA and the individual satellite datasets are, first, of similar order as the mutual differences among the satellite datasets themselves (this is seen most easily by regarding the profiles themselves, thus the left panels of the respective figures). Second, the differences between KIMRA

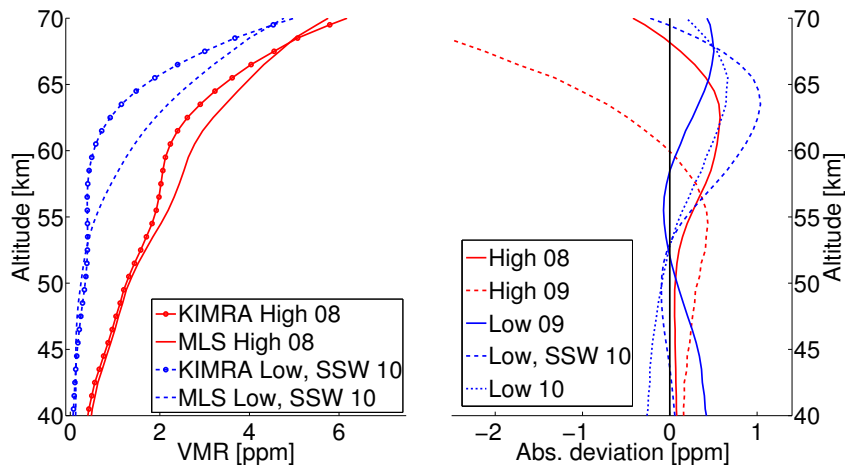


Figure 5.3: Investigation of the influence of the averaged period using the MLS dataset with the collocation criteria  $r_{\text{coll}} = 200 \text{ km}$  and  $\Delta P < 5\%$ . For details see Table 5.2. **Left:** mean profiles. Only two cases with comparatively high (red) or low (blue) CO values are shown for clarity of the figure. **Right:** deviation  $\Delta\chi_{\text{CO}}$  between the KIMRA and the satellite profiles. All analyzed cases are shown.

and the satellites are in the order of the influence of the wide collocation criteria.

A comment on particularly the MIPAS MA dataset is in order since this dataset has not been published and validated before. Concerning the profile shape, it appears here to be generally consistent with MLS (Fig. 5.6), but it shows slightly lower values. However, the comparison is limited by the small number of coincidences. This is even more the case for the comparison of MIPAS MA with ACE-FTS (Fig. 5.7), where only one day with coincidences was found with very relaxed collocation criteria. In this case, ACE-FTS deviates strongly, demonstrating that also the satellite datasets show a large scatter when evaluated on a single profile basis.

## 5.5 Discussion of the KIMRA profile shape deviation

The reason for the profile shape deviation of the KIMRA dataset is speculative. It is, however, likely that the general error source has to be sought in the KIMRA measurements since the deviation appears consistently in the comparisons to all the satellite datasets. Oscillatory deviations were previously also found for ozone profiles in ground-based microwave vs. satellite comparisons by Boyd et al. [2007] and Palm et al. [2010], who also attribute the reason to the ground-based microwave measurements. The error assessment (Figure 4.11, bottom) suggests that oscillatory systematic deviations may arise from uncertainties in the spectroscopic parameters. However, this can also be a result of a complex interplay of many instrumental and retrieval parameters.

In the particular context of CO, the present study has revealed another possible error source; it was shown that the retrieval performance in the vmr representation is imperfect above 70 km altitude (Sect. 4.3; Fig. 4.5b). This is connected to the ambiguity of the

emission linewidths, as discussed earlier (Sects. 4.2.5 and 4.3). This altitude range matches the location of the strong high bias for KIMRA in comparison to the satellites, so that both findings appear to be connected. Furthermore, dependencies between this altitude range and the lower profile parts exist (as indicated by the vertical resolution of the KIMRA dataset and characterized in detail by the individual AVK functions; Sect. 4.3). It can therefore not be excluded that the effect of the linewidths ambiguity also leads to deviations in the lower altitude range. Note that the smoothing of the satellite profiles with the KIMRA AVKs means that the established deviation is also smoothed by the AVKs and does not directly correspond to real atmospheric altitudes.

For the further application of the KIMRA dataset in this work the profile shape deviation is not expected to have a strong impact. The main application of this dataset is the use of CO as tracer for dynamics. Hence, only the CO variability in time is of direct importance and not the CO vmr itself. Since the time dependence of the profile shape deviation is not large (Sect. 5.3.2), this variability is expected to be consistently represented in the whole dataset over the full range of sensitivity. This is supported by, first, the general range of sensitivity of the KIMRA measurements (Figs. 4.5a and 4.12), showing that the retrieval results are dominated by information from the spectra well up to 80 km altitude. Second, this is supported by the visual comparison of the CO evolutions as measured by KIMRA and MLS (Figs. 4.9 and 4.10), showing similar temporal variability in the full altitude range. Third, this will also be shown quantitatively by the correlations of KIMRA and MLS presented in Chap. 6.

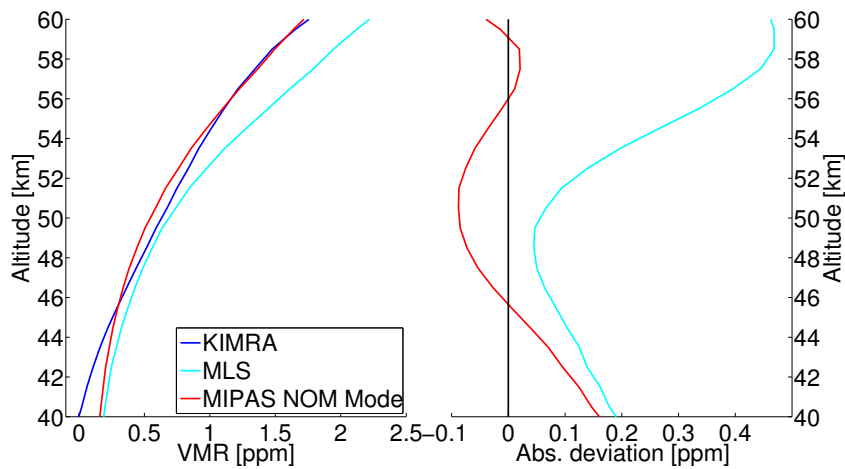


Figure 5.4: Comparison of KIMRA with MIPAS NOM and MLS using the collocation criteria  $r_{\text{coll}} = 250$  km and  $\Delta P < 20\%$ . 42 days with coincidences were found. **Left:** mean profiles. **Right:** deviation  $\Delta\chi_{\text{CO}}$  between the KIMRA and the satellite profiles.

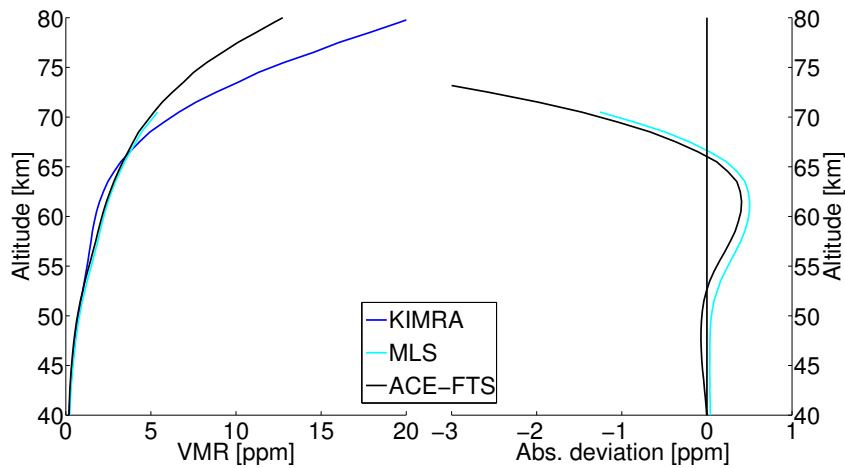


Figure 5.5: Comparison of KIMRA with ACE-FTS and MLS using the collocation criteria  $r_{\text{coll}} = 1000$  km and  $\Delta P < 20\%$ . 22 days with coincidences were found. **Left:** mean profiles. **Right:** deviation  $\Delta\chi_{\text{CO}}$  between the KIMRA and the satellite profiles.

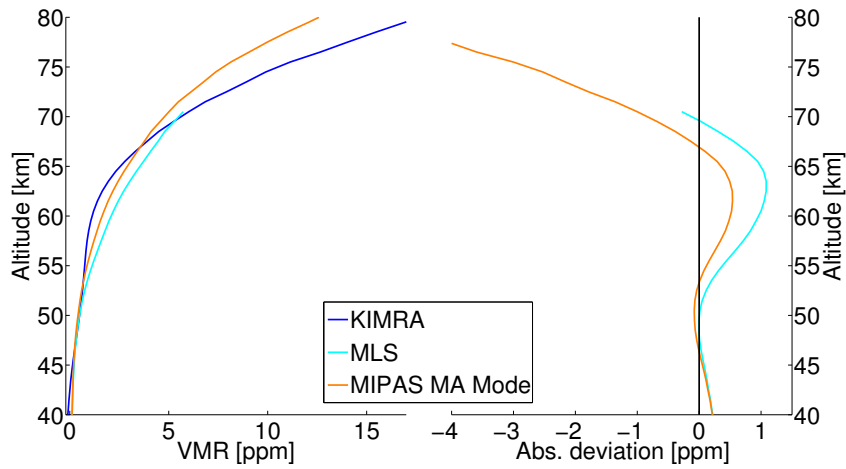


Figure 5.6: Comparison of KIMRA with MIPAS MA and MLS using the collocation criteria  $r_{\text{coll}} = 1000 \text{ km}$  and  $\Delta P < 20 \%$ . 9 days with coincidences were found. **Left:** mean profiles. **Right:** deviation  $\Delta\chi_{\text{CO}}$  between the KIMRA and the satellite profiles.

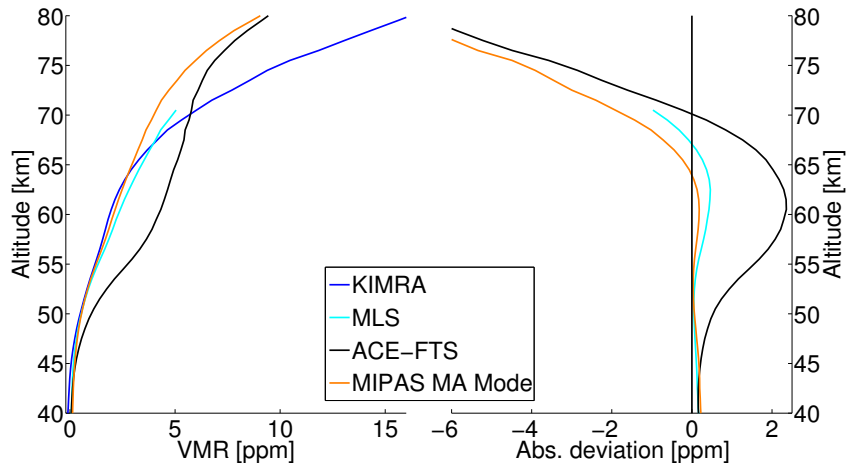


Figure 5.7: Comparison of KIMRA with ACE-FTS, MIPAS MA, and MLS using the collocation criteria  $r_{\text{coll}} = 1000 \text{ km}$  and  $\Delta P < 50 \%$ . 1 day with coincidences was found. **Left:** mean profiles. **Right:** deviation  $\Delta\chi_{\text{CO}}$  between the KIMRA and the satellite profiles.

## 5.6 Summary

The presented comparison of time-averaged CO profiles from the KIMRA ground-based microwave observations and satellites is the first such comparison, despite the number of ground-based CO datasets published before (Sect. 2.4.3). All three recent satellite instruments that provide data for the respective period and region have been considered, namely MLS, ACE-FTS, and MIPAS. In case of MIPAS, two different datasets, MIPAS NOM and MIPAS MA, have been included. Generally, such a comparison is difficult in the polar region due to the strong horizontal gradients of CO (Sect. 2.4.2.2) and the partly sparse coverage of satellite instruments. Therefore, the comparison was complicated by the partly small number of coincidences and to some extent by the influence of the relaxed collocation criteria. Furthermore, an estimation of the KIMRA data quality is complicated by the differences among the satellite datasets themselves.

In spite of this, it is evident that, first, the KIMRA CO vmr values generally agree with the satellites below about 65 km in the following sense; differences between KIMRA and individual satellite datasets are in the order of the differences among the satellite datasets. Second, the KIMRA profile shape deviates consistently from all satellite profiles in a way that the satellite profiles are more curved. Contrarily, the KIMRA profile shows a weaker increase of CO with altitude up to about 65 km and a stronger increase above. Third, this leads to a high bias for KIMRA above 70 km altitude, which increases strongly with altitude and exceeds the estimated errors (Sect. 4.5.2).

The reason for the profile shape deviation of KIMRA remains speculative. However, particularly the strong deviation above 70 km altitude is probably connected to the ambiguity of the linewidths identified before (Sect. 4.2.5 and Sect. 4.3), which is caused by thermospheric contributions to the received CO emission line. Therefore, this behavior could be an inherent property of ground-based microwave CO observations. However, the profile shape deviation is not expected to have a strong influence on the following analyses since not the CO vmr itself is of interest, but only its temporal variability. It has been indicated that the latter is expected to be consistently represented in the KIMRA dataset.

## 6 CO-based validation of the polar dynamics in the model SD-WACCM4

Large parts of this chapter have been published by Hoffmann et al. [2012].

Although CO is a tracer for dynamics in the polar winter middle atmosphere, the unique separation of the individual dynamical processes controlling the observed CO is complex; all dynamical processes can only lead to either an increase or a decrease of CO in a certain region (Sect. 2.4.2). For the examination of the dynamics in a comprehensive atmospheric model, however, a separation of these processes is not necessary since the temporal CO evolution can be compared directly. This validates the entire representation of processes influencing CO in the model, including residual influences of the CO chemistry in fall and spring. However, due to the tracer property, a successful comparison of CO gives primarily strong confidence in a good representation of the dynamics in the model.

Here, the specified dynamics (SD) version of the Whole Atmosphere Community Climate Model, version 4 (WACCM4), referred to as SD-WACCM4, is evaluated using the KIMRA CO time series (Chap. 4). WACCM4 and SD-WACCM4 are developed by the National Center for Atmospheric Research (NCAR) in Boulder, USA. In contrast to the ‘free-running’ model WACCM4, the temporal behavior of the atmosphere simulated with the SD version can directly be compared to measurements (see Sect. 6.1 for details). The presented comparison is among the first, which makes use of this recently developed feature; further comparisons have recently been published by Funke et al. [2011] and Marsh [2011]. Whereas these comparisons are mainly built on satellite data using either zonal or monthly means, the present study benefits from the particular advantage of ground-based measurements. These measurements provide a consistent time series for one particular location with a high temporal resolution. Hence, the representation of CO in the global model SD-WACCM4 is examined on the smallest space and time scales currently simulated; model output is taken from a single grid point, which is closest to Kiruna, and on each model day of the analyzed period.

Furthermore, satellite data from MLS were included in this analyses for two purposes. First, a quantitative comparison of the temporal CO behavior as observed by KIMRA and MLS is an important addition to the intercomparisons between the observed datasets presented above (Sect. 4.4.2 and Chap. 5). Second, this measurement–measurement comparison of ground-based and spatially distributed observations serves as a guide to what can be expected from such a comparison and helps to interpret the measurement–model comparison.

Note that a comparison of time-averaged CO profiles, similar to the one presented above for observational datasets (Chap. 5), has also been performed with SD-WACCM4 model data (Appendix A). The major outcome of this comparison is that the SD-WACCM4 mean profile is consistent with MLS. The KIMRA profile shape shows a deviation compared to MLS and SD-WACCM4, consistently with the findings of Chap. 5.

## 6.1 The Whole Atmosphere Community Climate Model (WACCM)

### 6.1.1 Context: Community Earth System Model

At NCAR, a whole family of models, representing several parts of the climate system, has been developed. In addition to this model family, a framework to couple these models is available, which altogether constitutes the Community Earth System Model (CESM). The CESM is one of the comprehensive climate models, which contribute to the assessment reports of the Intergovernmental Panel on Climate Change (IPCC) [Randall et al., 2007b] (precisely, a former version has contributed to the IPCC reports so far, the Community Climate System Model (CCSM) [Gent et al., 2011]). Note that this model family, the ‘community models’, are freely available to the climate science community.<sup>1</sup>

The standard atmosphere component of the CESM is the Community Atmosphere Model (CAM) [Neale et al., 2011], which roughly covers the troposphere and the stratosphere in its standard configuration. WACCM4 is an extension of CAM that covers the whole atmosphere from the surface up to the lower thermosphere (Sect. 6.1.2). It can be run in place of CAM as atmospheric component of the CESM to simulate couplings of the middle and upper atmosphere with other climate components, as long as the computational resources allow for this. However, WACCM4 can also be used stand-alone. In the present study, data of a specialized stand-alone version of WACCM4, the specified dynamics version SD-WACCM4 (Sect. 6.1.3), will be examined.

### 6.1.2 Description of WACCM4

WACCM4 is a comprehensive atmospheric chemistry-climate model (CCM), which means that the simulated chemistry and dynamics are fully interactive. The radiatively active gases therefore affect heating and cooling rates and with that dynamics. CCMs are basically composed of two major modules: a general circulation model (GCM), which simulates the atmospheric dynamics by solving the primitive equations (Sect. 2.2.5), and a chemistry-transport model (CTM), which simulates the atmospheric chemistry for given dynamics by essentially solving the continuity equations for all considered species. Originally, GCMs and CTMs have been designed to be run stand-alone, which is still commonly done. However, technical advances regarding the computational capacities allow for running both types coupled as CCM to achieve most comprehensive simulations of the atmosphere.

WACCM4 is typically used as a free-running CCM. Such models represent the true atmosphere only in a climatological, or statistical, sense. Even if the model is initialized with an observed atmospheric state, the simulated atmospheric evolution on short time scales quickly diverges from the true atmosphere. This is caused by the chaotic nature of atmospheric dynamics, i.e., by the high sensitivity to small errors of the initial state. Free running CCMs therefore produce arbitrary conditions on shorter time scales (e.g., weather), whereas the behavior averaged over longer time scales matches the climatological conditions of the real atmosphere. This fact limits the feasibility of validations by

---

<sup>1</sup>Further information, documentation, and source codes can be obtained from <http://www.cesm.ucar.edu/models/cesm1.0>, last access on 27 November 2011.

observations since only statistical quantities can be compared. This problem is tackled by ‘nudging’ a free running CCM with observed meteorological data, as implemented in SD-WACCM4 (Sect. 6.1.3).

WACCM4 is based upon an earlier version, documented by Garcia et al. [2007]. The model domain extends from the surface to the lower thermosphere (about 140 km geometric altitude). There are 66 levels in the vertical, with resolution of a little over 1 km in the troposphere and lower stratosphere, increasing to about 3.5 km in the lower thermosphere. The horizontal resolution is  $1.9^\circ \times 2.5^\circ$  in latitude and longitude.

The chemical module of WACCM4 is based upon the three dimensional CTM ‘model for ozone and related chemical tracers (MOZART)’, version 3 [Kinnison et al., 2007]. It includes a detailed representation of the chemical and physical processes in the troposphere through the lower thermosphere. The species included within this mechanism are contained within the  $O_x$ ,  $NO_x$ ,  $HO_x$ ,  $ClO_x$ , and  $BrO_x$  chemical families, along with  $CH_4$  and its degradation products. In addition, fourteen primary non-methane hydrocarbons and related oxygenated organic compounds are included [Emmons et al., 2010]. This mechanism contains 122 species, more than 220 gas-phase reactions, 71 photolytic processes, and 18 heterogeneous reactions on multiple aerosol types.

The implementation of WACCM4 is here not discussed in more detail. However, the representation of gravity waves in the model has to be outlined since it is relevant for the interpretation of the model–measurement comparison (Sect. 6.2.4). Since gravity wave breaking plays a major role in the momentum and constituent budgets of the mesosphere (Sect. 2.2.2 and, e.g., Garcia and Solomon [1985]), comprehensive models as WACCM4 must take into account the effects of dissipating mesoscale gravity waves. However, these mesoscale gravity waves have typical horizontal wavelengths of about 100 km, so that they cannot be resolved in WACCM4. Instead, their effects are parameterized following the work of, e.g., Lindzen [1981]. In practice, a ‘source’ spectrum of gravity waves is launched at model grid points in the troposphere, and its propagation and dissipation are calculated as functions of altitude. To simulate the ‘filtering of waves’ (Sect. 2.2.2), the spectrum is modified as it propagates through the stratosphere according to the winds in that region. These modifications condition the timing and intensity of wave breaking at higher altitudes, which drives the circulation in the mesosphere and lower thermosphere (Sect. 2.2.1.2). The results of this calculation are therefore used to estimate the acceleration of the resolved winds, as well as mixing due to induced vertical diffusion (see Garcia et al. [2007] for details). The source spectrum used in the gravity wave parameterization is based on observational estimates of the momentum flux due to vertically-propagating, mesoscale gravity waves in the troposphere. It is important to note that this spectrum is also only realistic in a statistical sense.

### 6.1.3 Description of SD-WACCM4

Recently, a specified dynamics version of WACCM4, referred to as SD-WACCM4, has been developed. The benefit of this extension is that the simulated atmosphere develops also on short time scales close to the real atmosphere. This is achieved by ‘nudging’ the model with analyzed meteorological fields, thus, with data based on observations (i.e., temperature, zonal and meridional winds, and surface pressure). However, the model dynamics is not totally forced by the external datasets, as it is the case for CTMs. Instead,

the model dynamics is only slightly constrained by replacing the model-predicted fields  $\mathbf{y}$  at each time step with a combination of these fields and the external data  $\mathbf{y}'$  according to:

$$\mathbf{y}(t) = 0.99 \mathbf{y}(t) + 0.01 \mathbf{y}'(t) \quad (6.1)$$

This nudging with only 1% of the external data corresponds to a relaxation of the model fields to the external fields with a time constant of approximately 2 days.<sup>2</sup> The nudging approach is described in more detail in Lamarque et al. [2011] for a related model.

In addition to the fact that the external fields are only considered in a small fraction, the nudging is only applied up to an altitude of 50 km. Above 60 km, SD-WACCM4 runs also completely freely; in the region between 50 km and 60 km altitude, the nudging is linearly decreased. Nevertheless, the simulated atmosphere above 60 km altitude is also expected to develop close to the real atmosphere; due to the wave driving (Sect. 2.2.2), the constrained domain below 50 km has a strong influence on the behavior in the unconstrained domain, in the mesosphere and lower thermosphere. This expectation is confirmed by the present study (Sect. 6.2.4).

The advantage of the nudging approach in SD-WACCM4 is that the model output can be compared meaningfully to a specific set of observations, also on shorter time scales. The benefit of such a comparison is twofold: first, the performance of SD-WACCM4 itself is examined, which is essential for future studies that are directly built upon this SD version. Second, a successful comparison based on SD-WACCM4 also helps to validate the overall quality of WACCM4 since the free-running and SD versions of the model use essentially the same numerics.

Note that SD-WACCM4 can, of course, not be used for predictive purposes since it depends on observations of the real atmosphere. Aside from its importance for the WACCM4 validation, SD-WACCM4 is intended to be a diagnostic tool for the understanding of atmospheric features observed in the past. Since SD-WACCM4 inherits all properties of the comprehensive CCM WACCM4, it is expected to be particularly powerful for this purpose.

For the present study, the used meteorological fields are taken from the Goddard Earth Observing System Model, version 5 (GEOS-5) of NASA's Global Modeling and Assimilation Office (GMAO). The SD-WACCM4 simulation employed here covers the period from 1 December 2004 through 1 January 2011. For these simulations the model was 'spun up' from 1980 to the end of 2003 in fully interactive mode, i.e., without specified dynamics. On 1 January 2004 the model was switched to the SD-WACCM4 configuration.

## 6.2 Comparison of the CO time evolution

### 6.2.1 Datasets and preprocessing

The time evolution of CO simulated by SD-WACCM4 has been compared to the KIMRA CO time series as well as to observations of the satellite instrument MLS. As for KIMRA, the complete retrieved dataset has been used (Chap. 4); for MLS the current data version 3.3 has been employed, which has already been described in the context of the

---

<sup>2</sup>An accumulated influence of 100% of the external fields is reached after 100 model time steps. This corresponds to 50 h in the simulation on the basis of the model time step of 0.5 h.

time-averaged profile comparison (Chap. 5). SD-WACCM4 data have been taken from a model run<sup>3</sup> performed at NCAR by Douglas Kinnison (Sect. 6.1.3).

During the preprocessing, collocated subsets of the spatially distributed datasets, MLS and SD-WACCM4, have been generated first. MLS profiles within a circle around Kiruna with radius  $r_{\text{coll}} = 200$  km have been selected. For SD-WACCM4, two different subsets have been created. The first one, referred to as ‘SDWACCM’, simply considers the closest grid-box ( $67.3^\circ$  N,  $20.0^\circ$  E) to Kiruna and corresponds therefore to the ground-based measurement approach. The second SD-WACCM4 subset, referred to as ‘SDWACCM AREA’, represents the satellite measurement approach. Hence, the same collocation criteria as for MLS have been applied.

The subsets of SD-WACCM4 and MLS have been interpolated vertically onto the KIMRA retrieval grid (Sect. 4.2.2). Afterwards, they have been convolved with the KIMRA AVKs,  $\mathbf{A}_{\text{vmr}}$ , using Eq. (3.31), so that the originally better-resolved profiles of SD-WACCM4 and MLS are directly comparable to the KIMRA measurements. The temporal grid has been unified by averaging the collocated profiles daily, so that the resulting time series contain one profile per day and dataset. However, the observational datasets may still have gaps due to a lack of measurements or the application of the collocation criteria.

The individual preprocessed time series have, furthermore, been split up into the long term variations, ‘low-frequency’ variability (LF), and the short term variations, ‘high-frequency’ variability (HF). To extract the LF part, the complete time series was Fourier transformed and the higher frequency contributions were removed by eliminating all Fourier components of periods less than 20 d. The LF part of the time series was then obtained via a reverse Fourier transformation of the modified spectrum. The HF changes in CO were calculated as the difference between the complete time series and the LF part. Note that gaps in the individual datasets were linearly interpolated before the separation to achieve an equidistant spacing of the time grid.

Major parts of the following analysis are based on correlation coefficients, which have been calculated at all relevant altitudes for the following pairs of time series: KIMRA–MLS, KIMRA–SDWACCM, and KIMRA–SDWACCM AREA. Precisely, the correlation coefficients for the complete time series as well as the for the LF and HF parts alone have been calculated. Periods during which at least one dataset of the respective pair was interpolated have been excluded from the computation.

Note that the use of the MLS profiles was restricted to a top-altitude of 70 km for the time-averaged profile comparison (Chap. 5). This was necessitated by the replacement of upper parts of the satellite profiles with the KIMRA a priori (Sect. 5.1). This was, however, only motivated by the properties of the other satellite datasets employed in the former context, and thus was applied to MLS only for reasons of consistency. Therefore, MLS data can be used here in the full analyzed altitude range of 40 km to 80 km.

## 6.2.2 Visual inspection of the time series

Fig. 6.1 shows the CO vmr time series of all datasets at 60 km altitude for both winters with KIMRA observations. Aside from the complete time series, the LF components alone

<sup>3</sup>NCAR’s internal identification is ‘sim140f’.

are also shown. Overall, the agreement of the two measurements and the model is very good. In particular, the LF part of all time series is generally consistent during the whole period. In addition, many features of the HF behavior are similar in all datasets, e.g., the rapid drop of the CO vmr due to SSWs at the end of January in both winters. KIMRA was not operational during the ‘disturbed period’ with strong CO variations in December 2009, but these variations are consistent for MLS and SDWACCM (the evolution of the polar vortex in the lower stratosphere during this period has been described by Pitts et al. [2011]). However, not all of the smaller variations are well matched among the different datasets. This is expected because of the high spatial and temporal variability, which is introduced by wave activity in this region (cf. Sect. 6.2.4).

Not only the variations in CO are consistent among the datasets, but so are generally the absolute CO vmr values. Exceptions are only apparent during distinct periods. KIMRA shows three of these periods with values lower than the other datasets, namely at the end of 2008, during February 2010, and during April 2010. These deviations can be attributed to the KIMRA dataset since the comparison of the mean profiles (Chap. 5 and Appendix A) has revealed that the KIMRA profile shape deviates systematically from other CO datasets. This leads, particularly at the 60 km level, to a negative bias for KIMRA (Fig. A.1 and several figures in Chap. 5). Furthermore, it has been shown that the altitude of this deviation varies slightly in time (Sect. 5.3.2). This has also been confirmed directly for the KIMRA–SDWACCM comparison (not shown). Thus, it is expected that the absolute KIMRA CO vmr considered at a particular altitude level will show a time-dependent offset. It has additionally been confirmed that this offset is not evident in the time series at altitudes where the mean profile shape deviation is small (e.g., at 50 km and 67 km altitude, not shown). In February 2009, MLS shows higher values, whereas KIMRA and SDWACCM are consistent. The reason for this deviation could not be established. However, it can be stated conclusively that the simulated CO of SD-WACCM4 during the complete period is as consistent with the measurements as the measurements are with each other.

### 6.2.3 Correlation analysis

Vertical profiles of the correlation coefficients for the pairs KIMRA–MLS, KIMRA–SDWACCM, and KIMRA–SDWACCM AREA are discussed in this section. As before, the complete time series, as well as the separated LF and HF parts are considered.

#### 6.2.3.1 KIMRA–MLS comparison

The correlations KIMRA–MLS (Fig. 6.2, red curves) have been calculated at first as a guide to what can be expected from a comparison of a single-point measurement with collocated data from a spatially distributed dataset. Additionally, this comparison serves as an extension to the comparison of CO measured with different observation techniques discussed earlier (Chap. 5).

The LF correlation is expectedly largest, with values higher than 0.95 above 50 km. The correlation coefficients for the complete time series are comparable to those for the LF part, since the complete time series is dominated by the LF variability. The correlation of the HF part displays lower values of about 0.6.

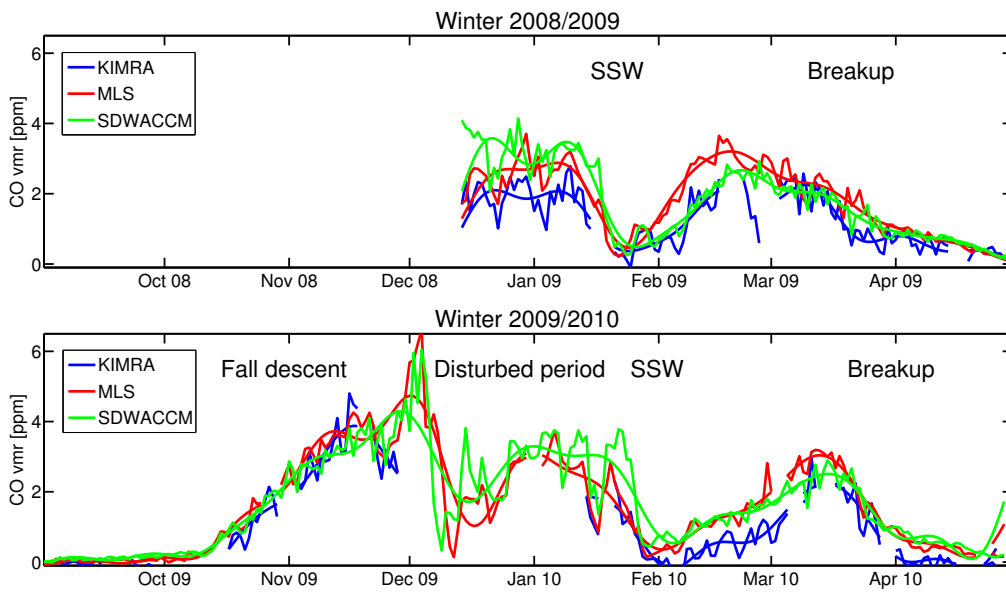


Figure 6.1: Evolution of the CO vmr at 60 km altitude as measured by KIMRA and MLS and as simulated by SD-WACCM4 during the full KIMRA period. The figure indicates the good agreement of all datasets. In particular, the low frequency variations (smooth curves; time scales  $> 20$  d; see Sect. 6.2.1 for details) are reproduced very well by SD-WACCM4, but also many features of the high frequency variability are matched well (e.g., the SSWs). See Sect. 4.4.2 for a description of the individual phases of the CO evolution and additionally Pitts et al. [2011] for a description of the ‘disturbed period’. Figure adapted from Hoffmann et al. [2012].

All correlation profiles show a common shape, which is most pronounced below 50 km altitude, where the correlation drops to values of about 0.7 at 40 km. In the range above 50 km, the correlation coefficients vary also slightly with altitude, showing maxima at approximately 53 km and 73 km and a minimum at approximately 60 km. This shape is connected to the characteristics of the KIMRA sensitivity. Fig. 6.3 (left) shows the area of the AVKs in this region (discussed earlier in Sect. 4.3.1). Here, it is emphasized that the sensitivity usually deviates also in the reliable region from the optimal value one, which is a common behavior for these retrievals. This deviation of the sensitivity from one (Fig. 6.3, right) exhibits a shape with two minima (at about 52 km and 72 km altitude) and three maxima (at approximately 40 km, 60 km, and 80 km altitude). Hence, it is evident that the altitudes of maximum correlation correspond to the altitudes where the sensitivity of KIMRA is closest to one and vice-versa. This suggests that the overall shape of the correlation profiles is governed by the KIMRA sensitivity. This causes, in particular, the relatively low values of the correlation coefficients below 50 km.

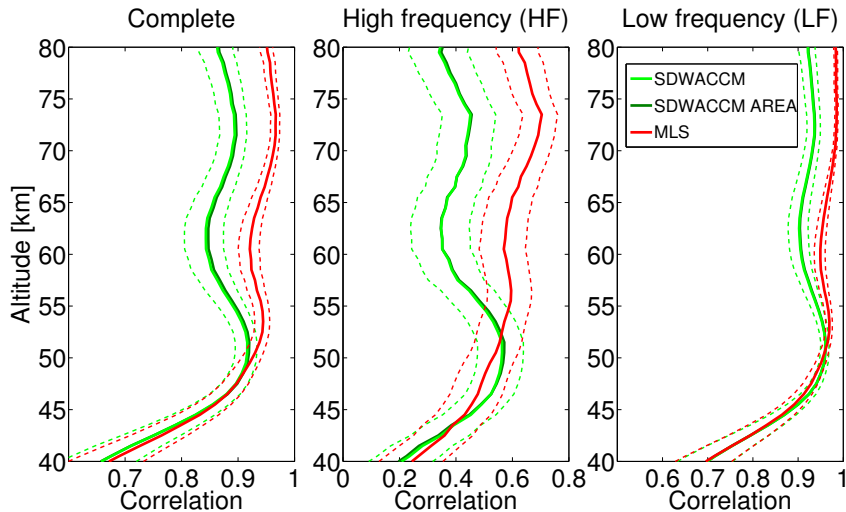


Figure 6.2: Altitude profiles of the correlation coefficients of the KIMRA–SDWACCM, KIMRA–SDWACCM AREA, and KIMRA–MLS comparison for the complete time series (**left panel**), for the HF part alone (**middle panel**, time scales  $< 20$  d, see Sect. 6.2.1 for details), and for the LF part alone (**right panel**, time scales  $> 20$  d). The KIMRA–SDWACCM AREA correlations can hardly be seen, as they are almost identical with the KIMRA–SDWACCM correlations. The dashed lines indicate the 95 % confidence interval of the correlation coefficients. Here, the comparison results indicated by the visual inspection (Sect. 6.2.2, Fig. 6.1) are quantitatively confirmed in the complete considered altitude range; the LF model–measurement correlation is with values of 0.9 in the order of the measurement–measurement correlation, demonstrating the good representation of slow CO variations in SD-WACCM4. The HF model–measurement correlation decreases with altitude in contrast to the measurement–measurement correlation; this is elaborated further in Fig. 6.4. The overall shape of the correlation profiles, particularly the low values between 40 km and 50 km, is explained by the KIMRA sensitivity (Fig. 6.3). Figure adopted from Hoffmann et al. [2012].

### 6.2.3.2 KIMRA–SD-WACCM4 comparison

The correlations of the pairs KIMRA–SDWACCM (Fig. 6.2, light green curves) and KIMRA–SDWACCM AREA (Fig. 6.2, dark green curves) are almost identical. This suggests that the correlation analysis is not affected by sampling errors within the limits of the collocation distance. Therefore, only the KIMRA–SDWACCM correlation is discussed here in detail.

Although being slightly lower than the KIMRA–MLS correlation coefficients, the KIMRA–SDWACCM correlation is still high, and shows values close to 0.9 for the complete time series. It is therefore evident that the measurement–model correlation is comparable to the measurement–measurement correlation. This is remarkable, considering that the global model is evaluated only at one model grid point to be compared to the single point measurement.

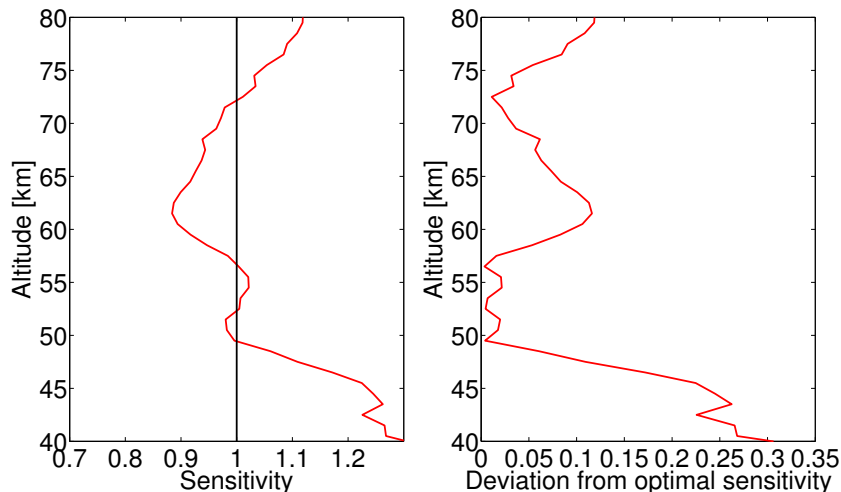


Figure 6.3: **Left:** Sensitivity of the KIMRA measurements as given by the area under the vmr AVK functions,  $\mathbf{A}_{\text{vmr}}$ . Curve corresponds to a detail (altitude range restricted to 40 km to 80 km) of Fig. 4.5a, red curve. The major point emphasized here is that the retrieval sensitivity deviates also in the reliable altitude range from the optimal value one, which is common for such retrievals. **Right:** Absolute deviation of the sensitivity from the optimal value one. The structure of this curve corresponds to the shape of the correlation profiles (Fig. 6.2, see Sect. 6.2.3.1 for details). Figure adopted from Hoffmann et al. [2012].

The overall shape of the KIMRA–SDWACCM correlation is also similar to that of KIMRA–MLS. Thus, this shape is also attributed to the KIMRA sensitivity characteristic and not to model behavior. However, the HF part of the KIMRA–SDWACCM correlation shows an additional feature; whereas this correlation profile is still similar to KIMRA–MLS below approximately 53 km, it decreases more rapidly with altitude to values of about 0.3 at 80 km altitude. This is much smaller than the roughly constant value of 0.6 found for KIMRA–MLS.

The differences between the measurement–measurement correlation and the model–measurement correlation in the HF and LF behavior are contrasted further in Fig. 6.4, in which these differences ( $\text{Corr}_{\text{KIMRA-MLS}} - \text{Corr}_{\text{KIMRA-SDWACCM}}$ ) are shown. On the one hand, the differences increase with altitude above 50 km for all cases, meaning that the KIMRA–SDWACCM correlation degrades with altitude compared to the KIMRA–MLS correlation. On the other hand, this effect is much more pronounced for the HF part alone. This shows that particularly the CO short term variability observed by KIMRA is not as well reproduced by SD-WACCM4 as it is in principle possible (i.e., not as good as the agreement of KIMRA and MLS). The HF variability is therefore the only aspect in which the model exhibits an imperfect behavior, whereas it reproduces the measurements very well in all other aspects. The reason for this is discussed below (Sect. 6.2.4).

One might argue that the correlation profiles are influenced by the coarse vertical resolution of the KIMRA dataset. To show that the main findings of this analysis are also valid when SD-WACCM4 is examined at higher vertical resolution, it has been verified that the correlation between SDWACCM and MLS (vertical resolution is approximately

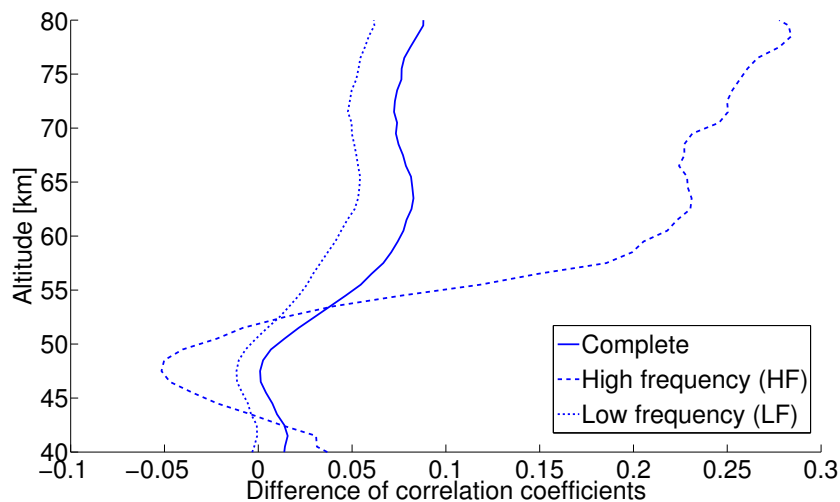


Figure 6.4: Differences between the correlation coefficients of KIMRA–MLS and KIMRA–SDWACCM for the complete time series as well as for the HF and LF parts. This figure is based on the correlation coefficients shown in Fig. 6.2. It emphasizes the differences of the LF and HF model behavior. The correlation coefficient differences of the LF part and the complete time series are close to zero and increase only slightly with altitude. This shows that the model reproduces the slow CO variations very well in the complete altitude range. Contrarily, the correlation coefficient differences for the HF variations increase above 50 km stronger with altitude. This shows that the short term behavior produced by the model deviates from the real atmosphere above 50 km and that this deviation becomes stronger with increasing altitude. This is explained by the gravity wave parametrization in SD-WACCM4, which is based on a generic gravity wave spectrum (Sect. 6.2.4). Figure adopted from Hoffmann et al. [2012].

5 km [Livesey et al., 2011]) exhibits a similar behavior (Fig. 6.5). Note that the most precise direct comparison with MLS requires convolving the SD-WACCM4 dataset with the MLS AVKs, which has not been done for this rough supplementary check.

#### 6.2.4 Interpretation of the correlation analysis

The KIMRA–SDWACCM comparison is almost as good as the KIMRA–MLS comparison for the complete time series as well as for the LF part. This demonstrates that the polar winter middle atmosphere dynamics is very well represented in SD-WACCM4. Evidently, the assumption that the nudging has only to be applied below approximately 50 km (Sect. 6.1.3) is reasonable. The relaxation to analyzed meteorological fields below this altitude constrains sufficiently the behavior of the simulated atmosphere, so that the free-running part of the simulation is also close to the measurements. This is particularly true for the effect of the nudged stratospheric winds on the parameterized gravity wave spectrum (i.e., the filtering of gravity waves; Sect. 2.2.2.1). Therefore, the mesospheric residual circulation and the corresponding transport of CO, which is driven by gravity

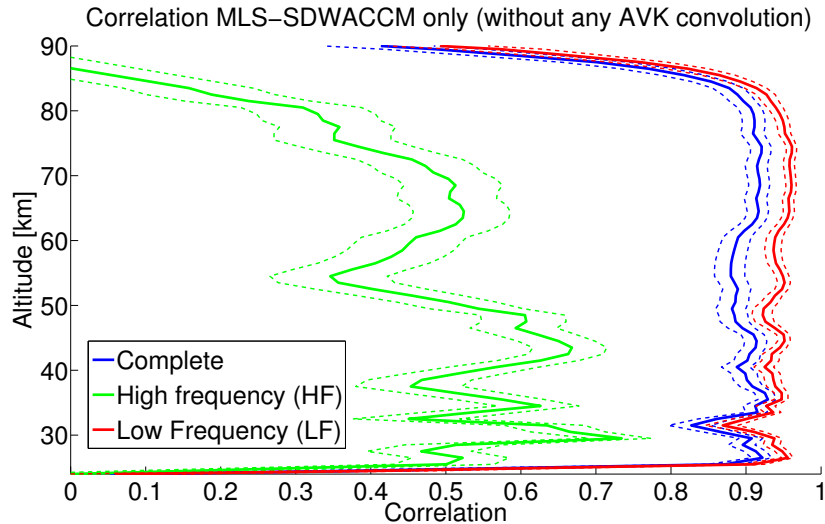


Figure 6.5: Altitude profiles of the MLS–SDWACCM correlation coefficients for the complete time series, for the HF part alone (time scales  $< 20$  d), and for the LF part alone (time scales  $> 20$  d). MLS and SDWACCM data have not been convolved with the KIMRA AVKs, so that these correlation coefficients are not restricted to the coarse KIMRA resolution. The general behavior between 40 km and 80 km is similar; the correlations of the complete time series and the LF part are of similar magnitude and roughly constant with altitude, whereas the HF correlation shows lower values and is degraded with altitude. This strongly supports the conclusion that all findings of this chapter are also valid when analyzed at higher vertical resolution. The dashed lines indicate the 95% confidence interval of the correlation coefficients. Figure adopted from Hoffmann et al. [2012, supplementary material].

wave breaking, are simulated close to the observations although not being nudged directly.

However, there is still a difference in the correlation coefficients between KIMRA–SDWACCM and KIMRA–MLS, which is particularly pronounced for the HF variability and increases with altitude. This finding has probably to be attributed to the gravity wave parametrization in SD-WACCM4. Therefore, the statement made above, regarding the good representation of gravity wave breaking in the model, has to be refined. The generic gravity wave spectrum launched in the troposphere (Sect. 6.1.2) is itself not improved by the nudging, i.e., it remains a generic spectrum, which is only realistic in a statistical sense. The latter, being realistic in a statistical sense, allows for the fact that the LF behavior of the simulated middle atmosphere is close to the real world evolution, in agreement with the statement made above. However, the detailed HF behavior of the actual gravity waves, which are present in the atmosphere at the respective observation time, cannot be represented by the generic gravity wave spectrum included in the model. Therefore, HF variability associated with gravity waves is not captured by SD-WACCM4, even though the model is driven by observed winds. This is consistent with the finding that particularly the HF model–measurement correlations are degraded with altitude, thus with increasing gravity wave influence.

One might wonder whether the crossover point from the nudged part to the free-running part provides an alternative explanation for the decreasing HF correlations between SD-WACCM4 and the observations above 50 km since the crossover occurs in this region (between 50 km and 60 km, Sect. 6.1.3). To investigate this point further, an additional model run<sup>4</sup> with the same setup, but with a transition to free-running mode between 40 km and 50 km, was performed and analyzed in the same way (Fig. 6.6). Note that the alternative crossover point was still chosen to be within the KIMRA range of sensitivity. For this alternative run the correlations are slightly different, but the differences are insignificant with respect to the 95 % confidence interval. Therefore, a significant impact of the crossover point on the HF correlations is not evident.

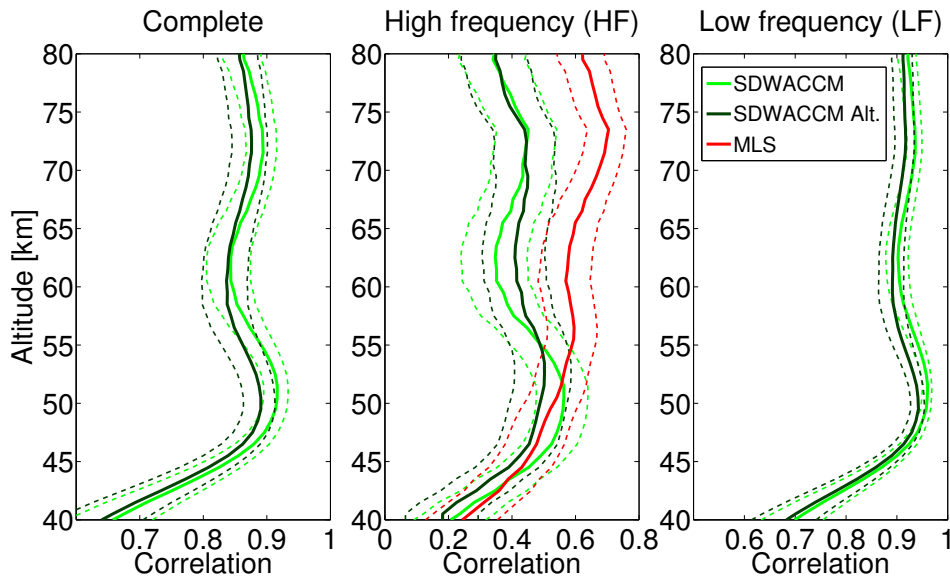


Figure 6.6: Altitude profiles of the correlation coefficients as in Fig. 6.2, but for the alternative KIMRA–SDWACCM comparison, which is based on a crossover point that is lower (between 40 km and 50 km) than for all other SD-WACCM4 data shown in this study. The original correlations for KIMRA–SDWACCM (as well as KIMRA–MLS for the HF part) are shown here only for comparison and are the same as in Fig. 6.2. The dashed lines indicate the 95 % confidence interval of the correlation coefficients. The differences between both model runs are insignificant with respect to the confidence interval. Particularly, they do not explain the drop of the HF measurement–model correlation in comparison to the measurement–measurement correlation. This finding excludes a significant influence of the crossover point. It therefore supports the conclusion that the differences in the HF behavior are explained by the gravity wave parametrization (Sect. 6.2.4). Figure adopted from Hoffmann et al. [2012].

<sup>4</sup>NCAR’s internal identification is ‘sim140fc’.

## 6.3 Summary and future perspectives

The representation of polar middle atmospheric CO in the model SD-WACCM4 has been validated using the KIMRA and MLS CO observations. Since CO is a tracer for dynamics in this region, the representation of polar dynamics in the model is evaluated indirectly with this approach.

SD-WACCM4 is a special version of NCAR's comprehensive CCM WACCM4 and is therefore part of NCAR's climate system model CESM. The particular benefit of SD-WACCM4 is that this version is directly comparable to measurements since it is nudged with external meteorological data in contrast to the free-running WACCM4. It is thereby assumed that a slight nudging (the nudging considers only 1% of the external meteorological data per time step and is only applied up to an altitude of approximately 50 km) is sufficient for the model to be close to the real atmosphere in the complete altitude range. This assumption and, moreover, the model performance in general have still to be validated with observations since SD-WACCM4 has recently been developed.

The presented validation of SD-WACCM4 is one of the first and, furthermore, it is a particular challenge for the model. It has been made use of the particular advantage of ground-based measurements to provide a consistent time series with a high temporal resolution for a certain location. Therefore, the global model has been evaluated at only one grid point and not in, e.g., a zonal mean sense. This grid point is closest to the measurement location in Kiruna, a location that is expected to exhibit particularly strong CO variability since the polar vortex boundary passes occasionally over this region (Sect. 4.1.1).

The validation is mainly based on altitude-resolved correlation coefficients between KIMRA and the subset of collocated SD-WACCM4 profiles. The correlation coefficients have been calculated for the complete time series, as well as for 'low-frequency' variability (LF) and 'high-frequency' variability (HF) parts alone (time scale threshold is 20 d). As a guide to what can be expected from such a comparison of a spatially distributed dataset to a ground-based observation, the same comparison has been repeated for KIMRA and the spatially distributed measurements of MLS. Differences between the measurement–measurement correlations KIMRA–MLS and the measurement–model correlations KIMRA–SDWACCM shed thereby light on the pure model characteristics.

The presented comparison of CO shows that the model is almost as consistent with the measurements as the measurements are with each other. The analysis reveals correlation coefficients as high as 0.9 between SD-WACCM4 and the observations for the complete time series and the LF contributions over large parts of the analyzed altitude range between 40 km and 80 km. This high agreement is remarkable considering both the only slight nudging and the examination at only one grid point. The only exception is the HF variability at higher altitudes. It exhibits lower model–measurement correlation coefficients, which degrade with altitude to a value of 0.3 at 80 km. The measurement–measurement correlation coefficients are, contrarily, constant with a value of approximately 0.6. This model behavior has been attributed to the gravity wave parametrization in WACCM4, which is based on a generic gravity wave spectrum.

Regarding dynamics, the presented validation indirectly demonstrates that the polar winter middle atmosphere dynamics is very well represented in SD-WACCM4. This shows, first, that the relaxation to analyzed meteorological fields below 50 km altitude constrains

the behavior of the simulation sufficiently, so that the free-running part above is also close to the measurements. Second, this result, transferred to the real atmosphere, suggests that the upper atmosphere can indeed be regarded as a driven system, which responds to the state at lower altitudes (cf. Sect. 2.2).

Since SD-WACCM4 inherits all features of the comprehensive, state-of-the-art CCM WACCM4 and since it is, moreover, able to simulate the detailed time evolution of the real atmosphere due to the nudging, SD-WACCM4 is expected to be a powerful new tool for the diagnosis of atmospheric processes in future research. The present validation strongly supports this expectation particularly for the polar middle atmosphere dynamics. It demonstrates that all the features of major interest (the descent of mesospheric air, the SSWs, and the breakup of the vortex) are well reproduced by SD-WACCM4. The model can and should therefore be employed to gain further insights into these features as well as into their interactions with the ozone layer and climate change (Chap. 1).

In the following of this thesis, it will also be built on these results; SD-WACCM4 is used to elaborate on the interpretation of the descent rates derived from CO time series (Chap. 7).

## 7 On the essence of descent rates derived from CO time series

It has been shown that a measured time series of CO can itself be used to indirectly examine the dynamics of a comprehensive model (Chap. 6). This is the most robust application of a CO dataset as tracer, considering the complexity of attributing variations in CO to the underlying dynamical processes (Sect. 2.4.2.3). However, particular circumstances demand for the direct knowledge of dynamical quantities, and thus in the present context for a derivation of these quantities from the measured CO time series. This is, for example, the case if a model with a particular focus on dynamics is examined, which does not have a comprehensive representation of the atmospheric chemistry including CO.

The timing of abrupt events, particularly the onset of SSWs, can be determined straightforwardly by identifying the associated rapid change of CO in the time series. A feature of major interest is, however, the descent of mesospheric air into the stratosphere during the course of the winter (Chap. 1). The corresponding ‘descent rates’ cannot be measured directly and the analysis of CO time series is a promising approach for the indirect derivation (Sect. 2.4.2.4). However, in contrast to the investigation of abrupt events, the derivation of descent rates demands for a consideration of longer periods of the CO time series. For these periods, it has to be assumed that the descent has continuously the dominating influence on the CO vmr, despite the strong variability of the polar dynamics and the possible influence of competing processes. These processes, which are mostly related to horizontal transport and mixing (Sect. 2.4.2.3) as well as more rarely to chemistry (Sect. 2.4.2.1), will be simply referred to as ‘other processes’ in the following discussion, opposed to the ‘descent’ of mesospheric air.

Nevertheless, descent rates derived from CO time series have previously been presented in a few studies (Table. 7.1, Sect. 2.4.3). In all of these studies, the straightforward derivation method described above (Sect. 2.4.2.4) is basically employed. The periods for which descent rates have been derived are mostly restricted to either the fall season or to a few weeks after an SSW. For both cases, a relatively strong polar vortex is at least more likely than for other periods. Therefore, the domination of the descent over the other processes is more likely during these periods. The justification of this assumption for the particular published cases is, however, only briefly discussed [e.g., Forkman et al., 2005] or even left unmentioned [e.g., Di Biagio et al., 2010].

Furthermore, the definition of the estimated ‘descent quantity’ is not clear. The two terms ‘descent rate’ and ‘vertical velocity’ are apparently used arbitrarily and interchangeably. Whereas the term ‘descent rate’ is not precisely connected to the theoretical framework (Chap. 2), the term ‘vertical velocity’ suggests a direct connection to the vertical wind, but either to the local wind  $w$  or to the TEM wind  $\bar{w}^*$  (Sect. 2.2.5). The latter apparent ambiguity is only clearly resolved for satellite measurements since satellite observations of CO are evaluated as a zonal mean for this purpose. The corresponding vertical

velocity is therefore the TEM wind  $\bar{w}^*$ , in agreement with its definition of being the quantity that characterizes the vertical tracer transport by the mean meridional circulation. Ground-based approaches, however, measure local CO, which can strictly speaking not be described with the TEM framework. It is therefore not clear whether the TEM  $\bar{w}^*$  or the local  $w$  is estimated by analyzing a CO time series that was measured at one location.

In the following, the term ‘descent rate’ will be used to refer to the quantity  $w_{\text{CO}}$ , which is derived from a CO time series according to Sect. 2.4.2.4. A connection to the vertical winds  $w$  and  $\bar{w}^*$  is intentionally left open at first and will be discussed later (Sect. 7.3).

In conclusion, the aim of the present chapter is to shed more light on an adequate interpretation of the descent rates derived in the mentioned studies, as well as in the present study below (Sect. 7.1). Particularly, it is elaborated on two issues: first, what is the interpretation of the descent rates  $w_{\text{CO}}$  derived from a CO time series measured at one particular location, as for ground-based measurements? Second, is there a significant influence of other processes than the descent and does it affect the attribution of the descent rates to the vertical winds? These issues are addressed by analyzing simulations of CO time series.

## 7.1 Descent rates derived from KIMRA CO and SD-WACCM4 CO

### 7.1.1 Numerical implementation

The method that is commonly used to derive descent rates from CO time series has been described in Sect. 2.4.2.4. It has been shown that generally two expressions can be used to derive an estimation of descent rates,  $w_{\text{CO}}$ , depending on whether the calculations are performed on constant CO levels or constant altitude levels. Both expressions, which are analytically equivalent (Eq. 2.17), have been implemented numerically:

$$w_{\text{CO}}(z, t) = -\frac{\Delta z}{\Delta \chi_{\text{CO}}} \bigg|_t \frac{\Delta \chi_{\text{CO}}}{\Delta t} \bigg|_z \quad \text{and} \quad w_{\text{CO}}(z, t) = \frac{\Delta z}{\Delta t} \bigg|_{\chi_{\text{CO}}}. \quad (7.1)$$

The finite differences are calculated as centered differences, e.g.,

$$\frac{\Delta \chi_{\text{CO}}}{\Delta t} \bigg|_z (z_i, t_j) = \frac{\chi_{\text{CO}}(z_i, t_{j+1}) - \chi_{\text{CO}}(z_i, t_{j-1})}{t_{j+1} - t_{j-1}}, \quad (7.2)$$

except for the boundaries of the calculation grid, where forward or backward differences are evaluated, respectively. Although the descent rates derived with both methods from the same CO time series exhibit differences under certain conditions, both expressions can be regarded as numerically equivalent for the present purpose, i.e., the differences do not affect the presented analysis and the inferred conclusions.

Note that the definition of  $w_{\text{CO}}$  is made to produce a sign that is consistent with the vertical velocity. Hence, negative values of  $w_{\text{CO}}$  represent descending air.

### 7.1.2 Derived descent rates of the winter 2009/2010

Descent rates,  $w_{\text{CO}}$ , from the KIMRA CO time series (Sect. 4.4.2, Fig. 4.9) have been derived for the winter 2009/2010. The KIMRA data have been averaged daily prior to

Table 7.1: Details on publications dealing with the investigation of the descent of mesospheric air based on CO observations (list does not claim to be exhaustive).

Reference	Region	Technique	Descent rates [m/d]	Period	used term
Allen et al. [2000]	Antarctica	satellite	-250 to -330	fall	'descent rate'
Forkman et al. [2005]	northern mid-latitudes	ground-based	up to -300	fall	'vertical velocity'
Funke et al. [2009]	Arctic	satellite	-350 to -400	Sept./Oct.	'vertical velocity'
Funke et al. [2009]	Arctic	satellite	-200 to -300	Nov./Dec.	'vertical velocity'
Funke et al. [2009]	Arctic	satellite	-1200	after SSW	'vertical velocity'
Di Biagio et al. [2010]	Arctic	ground-based	-200 to -300	after SSW	'descent rate'

the descent rate calculation. In this temporal resolution (example for 70 km altitude in Fig. 7.1, top), the descent rates exhibit a strong variability in time. This confirms that the observed CO is influenced by different competing processes, which partly act on short time scales. Hence, the descent rate variability represents the strong dynamical short-term variability expected to be present in this region. This underlines the complexity of extracting the pure descent from the CO time series; a period with clear continuous descent (negative values of  $w_{\text{CO}}$ ) can hardly be seen, although it is expected to be present.

To get an idea of the processes influencing CO on longer time scales, the derived descent rate time series has been smoothed with a method described before (Sect. 6.2.1); the descent rate time series has been Fourier transformed and periods shorter than 20 d have been removed from the spectrum, which has then been retransformed. The obtained smoothed time series of descent rates (Fig. 7.1, bottom) exhibits the three distinct periods that have been identified earlier directly in the CO time series (Sect. 4.4.2). First, a significant influence of the descent of air manifests itself here indeed through continuously negative values in October and November 2009. The estimated descent rates of  $-200$  m/d to  $-300$  m/d match the order of the previous studies (Table. 7.1). Second, the strong disturbance by the SSW in January 2010 with the associated removal of CO appears in the descent rates as a pronounced positive peak. It is followed by a negative peak and a second phase of continuously negative  $w_{\text{CO}}$ . This phase likely represents the continuing descent in the reestablished vortex after the SSW. Third, the breakup of the vortex leads to positive descent rates since all relevant processes decrease CO: more mixing with mid-latitude air, reactivated chemistry, and also the ascent of air.

The same procedure has been applied to the CO time series modeled by SD-WACCM4. In particular, the subset of profiles from the model grid point closest to Kiruna, 'SDWACCM' (Sect. 6.2.1), has been employed here again. Prior to the descent rate derivation, the profiles have been converted to the KIMRA retrieval grid (Sect. 4.2.2) and convolved with the KIMRA AVKs  $\mathbf{A}_{\text{vmr}}$ . As expected from the SD-WACCM4 validation results (Chap. 6), the descent rates derived from KIMRA and SDWACCM CO (Fig. 7.1) show a good agreement, in particular with respect to the long-term behavior. The model data fills, furthermore, the gaps in the KIMRA data, particularly the gap in December 2009 and January 2010. This period showed pronounced variability due to a strong disturbance of the polar vortex in early winter, which was already mentioned in Sect. 6.2.2 and has also been described by Pitts et al. [2011]. It is a good example of the difficulty of attributing CO changes to the dynamical causes and therefore of the difficulty

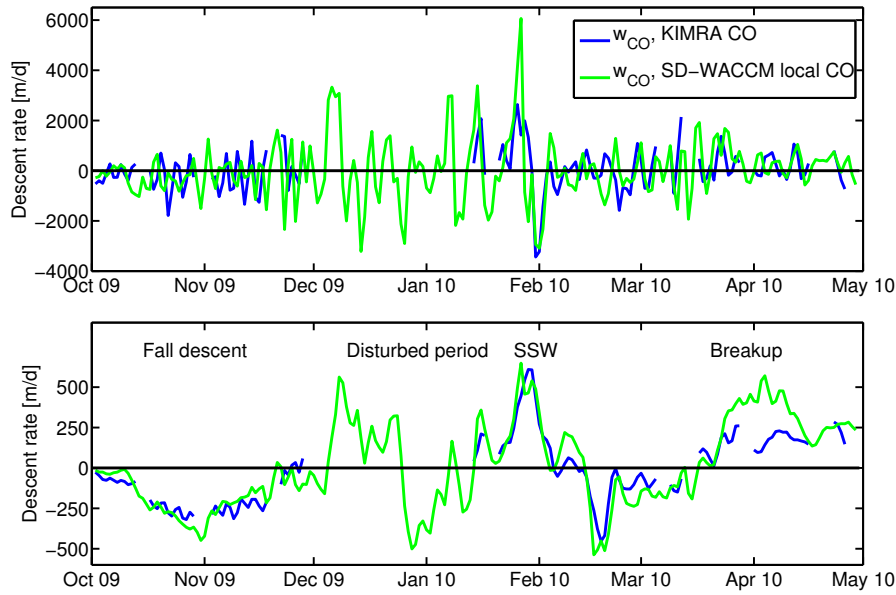


Figure 7.1: Descent rates  $w_{CO}$  at 70 km altitude for the winter 2009/2010 derived from the CO time series measured by KIMRA and simulated by SD-WACCM4. The sign is defined in a way that negative values indicate descent if interpreted as actual vertical motion. Interruptions of the blue curves indicate a lack of KIMRA measurements. **Top:** Descent rates plotted with a temporal resolution of 1 d. The curves exhibit a strong variability, consistent with the dynamical short-term variability expected to be present in this region. **Bottom:** Same data as in the top panel, but smoothed by eliminating all Fourier components with periods less than 20 d. Note the change of the y-axis scale. The smoothed curves reveal the major phases of polar winter dynamics as denoted in the plot, which are discussed further in the text (Sect. 7.1.2).

of attributing the derived descent rates to the actual vertical winds. A strong ascent of air is unexpected in this region so that the positive values in the first half of December are likely explained by other processes. The cause of the negative values in the second half of December could, however, be explained by both descent and other processes.

## 7.2 Simulation of CO evolutions for realistic and ideal conditions

The following analysis will completely be carried out on the basis of model data. The basic idea is to compare of two fundamentally different simulations of CO time series. The first simulation, here SD-WACCM4, is as close to the real world as possible. The second simulation considers only the descent of air as CO-influencing process. The latter generates the only case for which the descent rates  $w_{CO}$  are definitely equal to the respective vertical winds since the major assumption for the applicability of the derivation method (Sect. 2.4.2.4) is by definition fulfilled. The differences between both simulations indicate therefore the importance of the other processes influencing CO. A straightforward, one-

dimensional simulation has been implemented particularly for this purpose (Sect. 7.2.1) and will be employed here in addition to SD-WACCM4.

Note that SD-WACCM4 will be considered to represent the real atmosphere for the present application. The good SD-WACCM4 validation results (Chap. 6) and the agreement of the descent rates derived from KIMRA and SD-WACCM4 (Sect. 7.1.2) are a strong indication for the tenability of this assumption in the present context. Nevertheless, it should be kept in mind that pure model simulations are the basis for the following.

### 7.2.1 Implementation of the one-dimensional vertical advection simulation

To simulate a CO time series, which is only controlled by vertical advection, the vertical part of the continuity equation,

$$\frac{\partial \tilde{\chi}_{\text{CO}}}{\partial t} = -\tilde{w} \frac{\partial \tilde{\chi}_{\text{CO}}}{\partial z}, \quad (7.3)$$

has to be integrated with time (cf. Eqs. 2.14, 2.15, and 2.18) using appropriate initial and boundary conditions as well as the wind field,  $\tilde{w}$ , of interest. The quantities denoted with a tilde,  $\tilde{w}$  and  $\tilde{\chi}_{\text{CO}}$ , indicate that they are replaced according to the considered situation; either by the local variables  $w$  and  $\chi_{\text{CO}}$  or by the TEM variables  $\bar{w}^*$  and  $\bar{\chi}_{\text{CO}}$ .

Several approaches, ‘advection schemes’, exist for the numerical integration of Eq. (7.3). Tests with comparatively simple schemes like ‘upwind’ were carried out and showed promising results. However, these schemes are not expected to work reliably in the presence of strong gradients, which likely occur in CO time series. Furthermore, the consideration of local vertical winds, which show quick fluctuations and direction reversals, caused problems also for a more sophisticated scheme described by Bott [1989].

Finally, a simple version of the piecewise parabolic method (PPM) [Colella and Woodward, 1984] was employed. This is an established scheme for the numerical modeling of fluids, which is also included in one of the dynamical cores of CAM and therefore WACCM4 [Neale et al., 2010]. The basic idea of this approach is to express the original, discrete CO profile with a piecewise continuous, parabolic function in space, for which Eq. (7.3) can explicitly be solved. This method was implemented reusing fragments of the ‘Virginia Hydrodynamics 1 (VH-1)’ code<sup>1</sup> [Boroson et al., 2001, and references therein].

The calculations are performed on a vertical grid with a spacing of 1 km and a time step of 20 min. The simulated vertical range and time period are adjusted according to the specific requirements. The initial CO profile is taken from a SD-WACCM4 simulation and is interpolated linearly to the vertical simulation grid. The CO vmr at the upper and lower boundary of the simulation are taken from the SD-WACCM4 dataset as well, which is therefore interpolated linearly in time from its one-day resolution to the 20 min time step of the simulation. The respective wind fields, which are also taken from SD-WACCM4, are interpolated similarly in space in time.

<sup>1</sup>Source code and documentation are available at <http://astro.physics.ncsu.edu/pub/VH-1/>, last access on 1 December 2011.

## 7.2.2 Comparison of the simulated CO evolutions

To investigate the questions raised in the introduction to this chapter, CO simulations of two scenarios have been studied for the winter 2009/2010: first, local CO for the location of Kiruna, which represents a ground-based measurement, and second, zonal mean CO averaged between 70°N and 80°N latitude representing data from a satellite measurement. For both cases the original SD-WACCM4 data (referred to as ‘real-world’) have been considered, as well as the one-dimensional simulations (‘vertical-advection-only’).

These vertical-advection-only simulations have been carried out between 10 km to 75 km altitude from October 2009 to April 2010. The upper altitude limit roughly represents the highest altitude up to which the mixing barrier is assumed to be strong enough for the descent rate derivation. Since all external data (initial CO profile, boundary CO, and the vertical winds) are taken from SD-WACCM4 (Sect. 7.2.1), this one-dimensional simulation essentially replaces a specific part of the real-world CO time series simulated by SD-WACCM4. This replaced part represents a CO evolution, which would have been simulated by SD-WACCM4 if only vertical transport had influenced CO. For the first scenario, the simulation of local CO, the local vertical SD-WACCM4 winds,  $w$ , have been taken as input for the vertical-advection-only simulation, whereas the TEM winds  $\bar{w}^*$  have been used for the zonal mean scenario.

Pronounced differences between the real-world simulation and the vertical-advection-only simulation are obvious for the local Kiruna CO scenario (Fig. 7.2). Much higher CO levels reach lower altitudes during the course of the winter. Furthermore, the slopes of the CO contours, which determine the descent rates, are much steeper in the vertical-advection-only case, being partly close to vertical. This means that variations in CO above 75 km altitude appear also at lower altitudes within just a few days. Hence, the strong influence of other processes, which remove CO from the polar middle atmosphere, is evident from comparing both simulations. During the winter months, these processes must be related to horizontal dynamics, particularly to the exchange of air across the mixing barrier since a chemical loss is unlikely during this period. Furthermore, it is evident from the differences in the CO contour slopes that descent rates derived from the real-world CO do not provide a reasonable estimation of the local wind  $w$ .

Also for the zonal mean scenario, pronounced differences are obvious in the amount of CO at lower altitudes between the real-world CO and the vertical-advection-only simulation (Fig. 7.3). However, it appears that the slopes of the CO contours are not changed as much as for the local CO scenario. The rating of the significance of the other processes influencing CO is therefore more complex in the zonal mean case: on the one hand, the other processes have indeed a significant influence on the amount of CO. On the other hand, their inclusion does not clearly influence the slopes of the contours. This preservation of the CO slopes is a major point for the interpretation of the descent rates in the zonal mean scenario; the slopes of the CO contours remain in the order of magnitude that is implied by the TEM wind  $\bar{w}^*$ , despite the strong influence of CO loss processes.

## 7.2.3 Interpretation of the simulation results

The analysis of the simulation results has been carried out on a basic level. It has been focused on the most pronounced influences on CO to gain a general understanding of the

meaning of the descent rates derived from CO. Consequently, the following statements are intended to correspond to the orders of magnitudes of the respective quantities and not to their accurate behavior.

In this sense, a clear answer can be given to the first question raised in the beginning of this chapter, which regards the interpretation of a CO time series that was obtained at one particular location. The comparison of such a local real-world CO time series (Fig. 7.2, top) with a zonal mean real-world time series (Fig. 7.3, top) reveals that the overall appearances of these time series are similar. Particularly, the slopes of the CO contours are comparable. Therefore, the descent rates derived from local and zonally averaged CO time series describe essentially the same quantity. The reason for this is possibly connected to mixing of air within the vortex. This mixing homogenizes the inner vortex air and flattens longitudinal CO gradients within the vortex, so that the zonal mean CO abundance is close to any local value. Furthermore, the vortex rotates, so that different parts of the vortex are measured at one location at different points in time. A time scale for this effect<sup>2</sup> is in the order of 10 d, which is shorter than the smoothing time scale of 20 d (or a few weeks if the descent rates are derived by following a CO isoline by eye) applied to the descent rate time series.

The second question raised in the beginning of this chapter aims at a correct interpretation of the estimated descent rates,  $w_{\text{CO}}$ , particularly if the influences of the other processes are considered, which decrease CO. From a comparison of the slopes of the real-world CO contours (Figs. 7.2, top and 7.3, top) with the slopes of the vertical-advection-only CO contours (Figs. 7.2, bottom and 7.3, bottom), it is evident that the former slopes are only similar to the vertical-advection-only simulation based on the TEM winds  $\bar{w}^*$ , but not to the one based on the local winds  $w$ . The descent rates  $w_{\text{CO}}$  represent therefore the order of magnitude of the TEM winds  $\bar{w}^*$ .

One might argue that this finding resembles the definition of the TEM vertical wind,  $\bar{w}^*$ , which is designed to describe the vertical velocity of the tracer transport. However, the comparison of the real-world CO time series with the vertical-advection-only CO reveals that the connection between  $w_{\text{CO}}$  and  $\bar{w}^*$  is not straightforward. Instead, it is obvious that the basic assumption, made for the descent rate derivation (the domination of the descent over all other processes in their effects on CO), is severely violated in the case of the real-world CO. In contrast to this assumption, the CO amount itself is strongly affected by other processes. A connection between  $w_{\text{CO}}$  and  $\bar{w}^*$  only remains because the slopes of the CO contours are not changed much.

The present study therefore confirms that  $w_{\text{CO}}$  might match the order of magnitude of  $\bar{w}^*$ , but it also reveals that there is a missing link in the chain of reasoning: it is unclear why the slopes of the CO contours remain similar, although CO itself is severely decreased by the other processes. To gain an intuitive understanding of this problem, it is helpful to imagine a case in which the horizontal influences on CO were even stronger. Considering they would, e.g., not only decrease the amount of CO strongly, but they would completely remove the descending CO below 60 km altitude; then the derived descent rates below 60 km altitude would be constantly zero. Thus, there would be no signal of the descent in the CO time series anymore, although the mesospheric air would continue to descend.

---

<sup>2</sup>With the circumference of the Earth of 15000 km at 67°N latitude and a rough estimation of the zonal velocity of 20 m/s (which is in the order of 25 % of the maximum zonal wind speed).

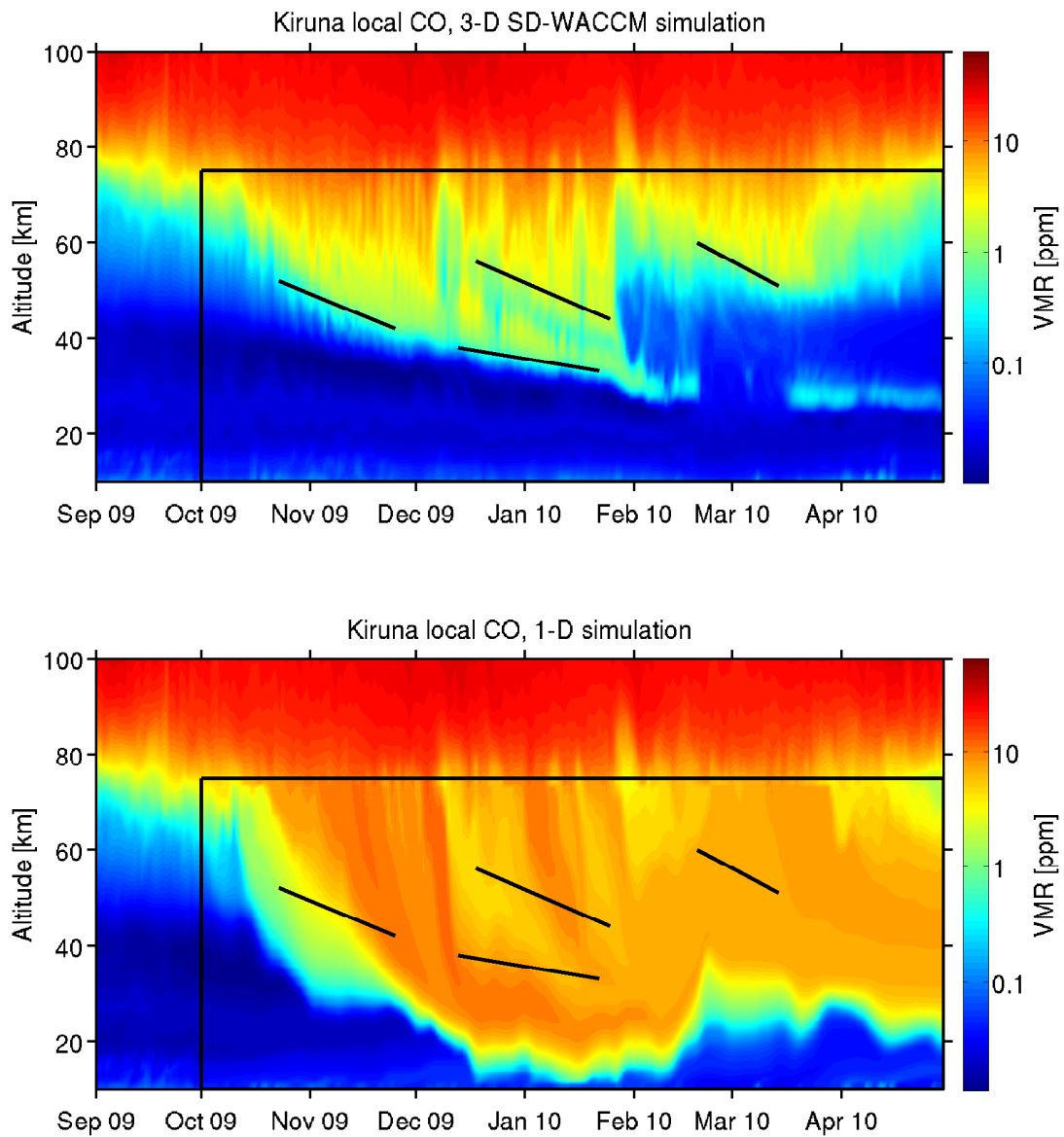


Figure 7.2: Simulation of the CO evolution during the winter 2009/2010 at the particular location of Kiruna for, first, the real-world conditions as simulated by SD-WACCM4 (**top panel**). Second, this time series has been replaced between 10 km and 75 km altitude (enclosed by the black rectangle) by results of the vertical-advection-only simulation from October 2009 on using the local vertical wind  $w(z, t)$  (**bottom panel**). Some of the CO contours of the original time series have been highlighted with black lines, which are equal in both panels. It is evident that much more CO would be present in lower altitudes if only vertical advection would be relevant. Furthermore, many CO contours are nearly vertical between 50 km and 75 km altitude for the case of purely vertical advection.

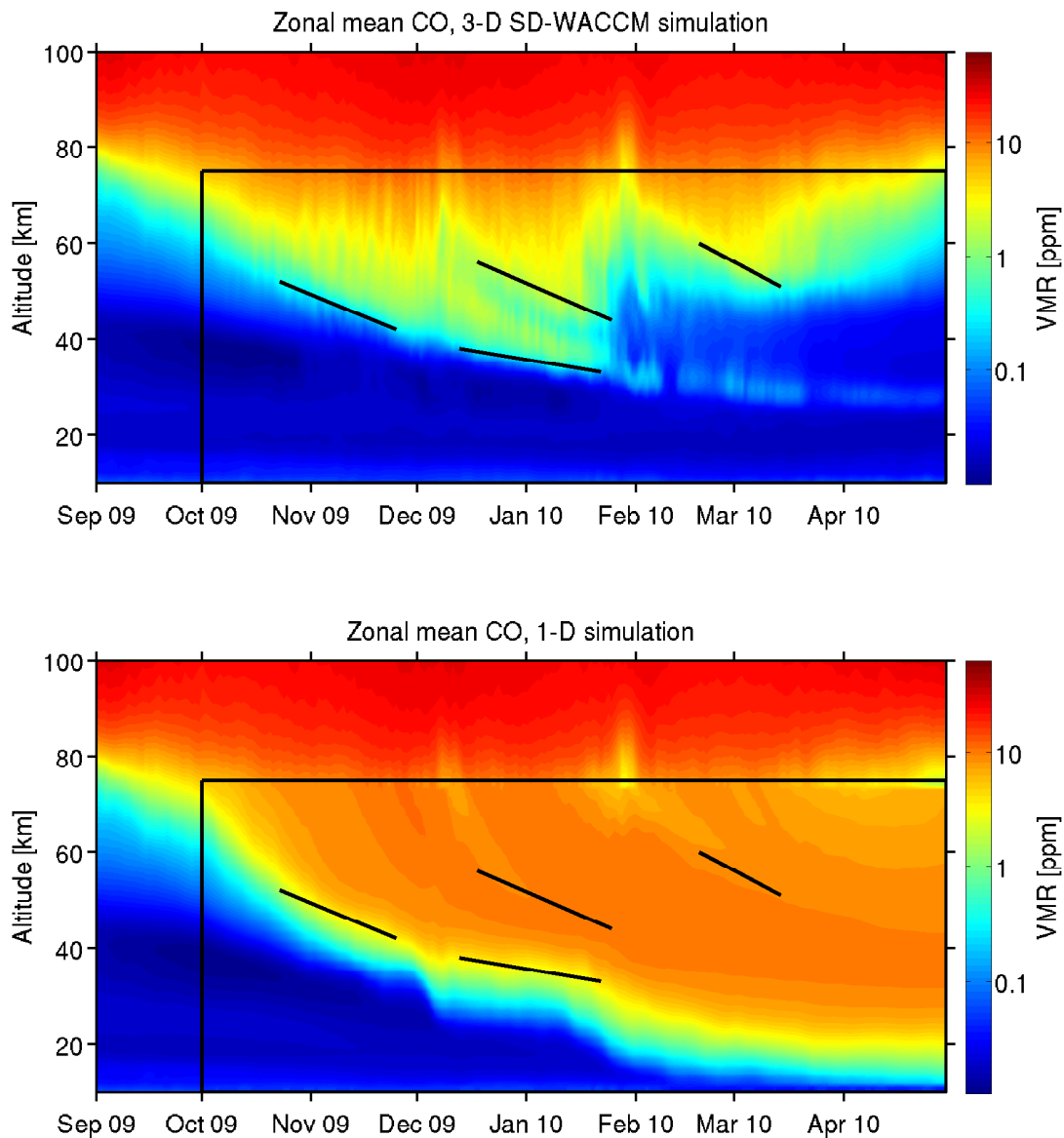


Figure 7.3: Simulation of the CO evolution during the winter 2009/2010 as a zonal mean between  $70^{\circ}\text{N}$  and  $80^{\circ}\text{N}$  latitude for, first, the real-world conditions as simulated by SD-WACCM4 (**top panel**). Second, this time series has been replaced between 10 km to 75 km altitude (enclosed by the black rectangle) by results of the vertical-advection-only simulation from October 2009 on using the TEM vertical wind  $\bar{w}^*(z, t)$  (**bottom panel**). The black lines, highlighting CO contours, are equal to those in Fig. 7.2. As in Fig. 7.2, it is evident that much more CO would be present in lower altitudes if only vertical advection would be relevant. However, the slopes of the CO contours between 50 km and 75 km are much less changed for the case of purely vertical advection with TEM winds.

### 7.3 Comparison of the descent rates and the TEM wind in SD-WACCM4

In this section, it is briefly elaborated on the finding that the descent rates derived from CO match at least the order of magnitude of the vertical TEM wind. In order to check whether there is even a closer agreement between both quantities in certain cases, the best agreement of  $w_{CO}$  and  $\bar{w}^*$  has been sought. This has, in turn, been carried out by finding roughly the minimum deviation. Furthermore, it has been considered that the deviation should remain at low levels during longer periods. It was found that these requirements are matched best when considering the descent rates for a fixed CO level during the course of the winter, particularly for about 0.8 ppmv in the winter 2009/2010. This level roughly corresponds to the light blue region in the time series presented before (Fig. 7.2, top), hence to a region where the descent is also seen clearly by eye.

The descent rates have been calculated for both local CO and zonal mean CO from the SD-WACCM4 real-world simulation. They have been smoothed similarly to the KIMRA descent rates with a 20 d time constant (Sect. 7.1). As expected, the derived time series of descent rates (Fig. 7.4, top) exhibits the same phases as before (Sect. 7.1.2): the descent in fall 2009, a quite disturbed period in December 2009, the SSW in January 2010 and the breakup of the vortex in spring 2010. Furthermore, the figure confirms that the descent rates derived from both local and zonal mean CO are comparable (cf. Sect. 7.2.3). However, the descent rates from zonal mean CO are, expectedly, less noisy.

It is evident from Fig. 7.4 (top) that the absolute value of  $w_{CO}$  is mostly lower than that of  $\bar{w}^*$ . Hence,  $w_{CO}$  can at least be seen as lower bound of  $\bar{w}^*$ . This is consistent with the fact that the other relevant processes dominantly remove the CO, which descends from higher altitudes. The few occasions during which the absolute value of  $w_{CO}$  is greater than that of  $\bar{w}^*$  must, in turn, be caused by a quick change from CO-poor to CO-rich air above the particular region. Hence, the responsible process is probably horizontal advection of inhomogeneous air masses during an overpass of the vortex boundary (Sect. 2.4.2.3).

The deviations of the descent rates  $w_{CO}$  from the vertical wind  $\bar{w}^*$  (Fig. 7.4, bottom) are smallest for two distinct phases during the course of the winter: during fall and some time after the SSW. This is consistent with the expectation that the polar vortex is most stable during these phases and confirms that the estimation of  $\bar{w}^*$  from a CO time series works best during these seasons. However, even these relatively small deviations range from 10 % to about 100 % of  $\bar{w}^*$ , showing that the other processes influencing CO are nearly always of importance. Furthermore, the deviations are themselves variable (and not, e.g., a constant offset), in agreement with the expected variable nature of the horizontal dynamics. It is therefore concluded that the descent rates  $w_{CO}$  do not represent more than the order of magnitude of  $\bar{w}^*$ . Furthermore, even this weak connection is not apparent during distinct periods with strong disturbances as, e.g., during the SSW, when deviations are in the order of a few hundred percent. Even higher deviations are seen during the vortex breakup in spring, which is expected due to the increasing importance of chemical CO loss (Sect. 2.4.2.1).

However, the absolute value of  $w_{CO}$  serves over large periods as lower bound for that of  $\bar{w}^*$ , as seen above. This fact suggests an alternative interpretation of the descent rates, which is discussed below (Sect. 7.4).

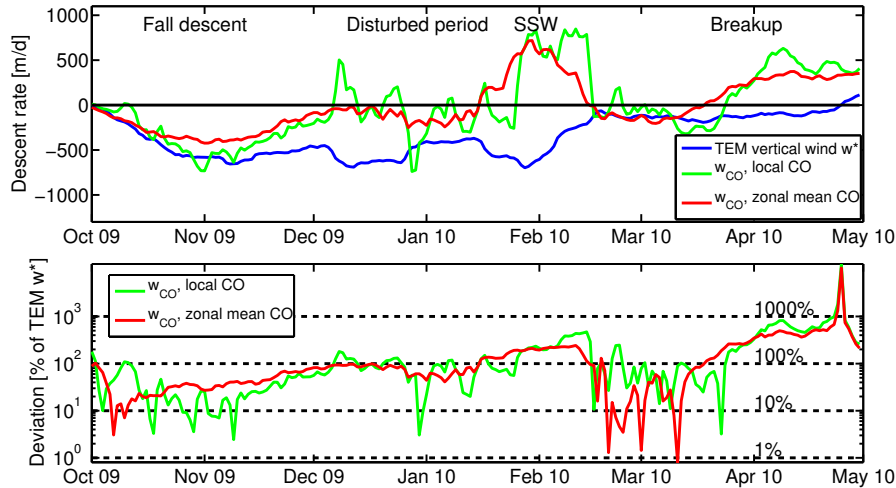


Figure 7.4: Comparison of descent rates derived from CO and the corresponding TEM wind  $\bar{w}^*$  for a fixed CO level of 0.8 ppmv based on SD-WACCM4 data. Curves are smoothed according to Sect. 7.1 with a 20 d time constant. **Top:**  $w_{CO}$ , for both the zonal mean CO and the local CO scenario, as well as  $\bar{w}^*$  for the Kiruna latitude. **Bottom:** Difference of the descent rates and  $\bar{w}^*$  expressed in percent of  $\bar{w}^*$ . Best agreement of  $w_{CO}$  and  $\bar{w}^*$  is found for periods during fall and some time after the SSW. However, the figure demonstrates the difficulty of precisely estimating the vertical wind based on descent rates from CO.

## 7.4 Proposed future research and an alternative interpretation of the descent rates from CO

Future research should emphasize an improvement of the understanding of the horizontal dynamics in the vicinity of the vortex boundary. This should also explain why the CO contour slopes experience only a comparatively slight change, although the inner-vortex CO vmr is strongly decreased by horizontal dynamics. This is a difficult field since it refers back to the known open questions related to the strength of the mixing barrier. Further insights can therefore only be expected from a continuation of the iterative process of improving the understanding of measured and simulated data alternately. In this context, it is important to note that SD-WACCM4 is a new powerful tool on the part of modeling, as has been shown in this work (Chap. 6). A promising approach based on SD-WACCM4 is a detailed altitude- and time-resolved analysis of the individual continuity equation terms for different species. Such an analysis is expected to provide a clearer idea of how air with mesospheric composition is modified while it descends into the stratosphere. This approach could also help to prove the following hypothetical interpretation of  $w_{CO}$ .

Although it is difficult to establish a clear connection between the descent rates and the vertical wind, the descent rates might be a useful quantity themselves. The main motivation for the investigation of the vertical transport is the potential appearance of air with a mesospheric composition in the stratosphere. In particular, the transport of mesospheric ozone and  $\text{NO}_x$  is of interest for the quantification of stratospheric ozone depletion (Sect. 2.3.3). Assuming that the horizontal processes, which have a strong

influence on CO, act similarly on all descending mesospheric species, the modification of CO would be characteristic for the modification of the overall mesospheric composition. In this sense, the descent rates,  $w_{\text{CO}}$ , could be seen as an ‘effective’ vertical transport velocity of the mesospheric air, which considers both effects: the dynamical vertical velocity  $\bar{w}^*$  and the removal of mesospheric air by horizontal influences, which tends to delay the appearance of this air at a certain stratospheric altitude. The major precondition for such an interpretation of  $w_{\text{CO}}$  is that the overall dynamical effects on CO are indeed representative for the complete mesospheric air. This assumption appears to be reasonable since CO is a tracer for dynamics in this region, but it has still to be validated.

## 7.5 Summary

Descent rates of mesospheric air,  $w_{\text{CO}}$ , have been estimated from the KIMRA CO time series, as well as from collocated SD-WACCM4 model data. Both time series of descent rates agree with each other and, moreover, agree with the order of magnitude of descent rates derived by previous studies for different winters.

It has been explained that a precise interpretation of the descent rates derived from CO is still unclear, despite the number of previous studies. First, it was unclear whether the descent rates derived from a CO time series obtained at one location (representing ground-based observations) are equal to those from a zonal mean CO time series (representing satellite observations). Second, the connection of  $w_{\text{CO}}$  and the actual vertical wind velocity is not straightforward due to the poorly known influences on CO of other processes than the descent (particularly the CO removal by horizontal dynamics). These issues have been tackled with a modeling study. CO time series of the comprehensive model SD-WACCM4, which is assumed to represent the real atmosphere, have been compared to simulations of ideal CO time series, which are only influenced by the vertical advection.

With respect to the first issue, it has been shown that the descent rates derived from both local and zonal mean CO are comparable. The results regarding the second issue are ambivalent. It has been shown that the order of magnitudes of the descent rates,  $w_{\text{CO}}$ , and the TEM vertical wind,  $\bar{w}^*$ , agree during longer periods in the season, particularly during fall and after an SSW. It has, however, also been shown that the existence of even this weak connection is difficult to explain since the CO removing processes are not neglectable during any phase of a winter, in contrast to the common assumption. Their main influence affects, however, mainly the abundance of CO, whereas the slopes of the CO contours are only affected to a smaller extent. The reasons for this unexpected finding are unclear. However, it implies that the order of magnitude of  $w_{\text{CO}}$  indeed agrees mostly with  $\bar{w}^*$ , whereas a more precise estimate of  $\bar{w}^*$  is not possible since the pure descent signal is still distorted by the residual influence of the CO removing processes.

Exploring the reasons for this result demands for further research with a special emphasis on the horizontal dynamics close to the vortex border. An extensive modeling study, in which all terms of the continuity equation for different species are precisely analyzed, has been proposed. Furthermore, an alternative interpretation of the descent rates derived from CO has been suggested;  $w_{\text{CO}}$  may indicate the ‘effective’ vertical velocity of mesospheric air, which considers the actual vertical wind  $\bar{w}^*$  and, moreover, the removal of mesospheric air by horizontal dynamics.

## 8 Summary and Outlook

The polar winter middle atmosphere dynamics exhibits a pronounced variability. It thereby also introduces variability to other atmospheric components, in particular to the ozone layer, which leads to complex interactions and feedbacks in the climate system. The complex processes causing the observed variability are not fully understood. Furthermore, the full extent of this variability has probably not been observed so far. Further observations and their reproduction by atmospheric models are therefore required.

The present thesis has contributed to this field in diverse aspects from an observational perspective with the focal point being the application of middle atmospheric CO as a tracer for polar dynamics. First, a time series of vertical CO profiles has been retrieved from ground-based microwave observations obtained with the KIMRA instrument in Kiruna, Sweden (northward of the Arctic Circle). Second, a comparison of time-averaged profiles between the KIMRA dataset and all recent satellite datasets has been performed to examine the consistency of these different observation techniques. Third, the KIMRA dataset has been employed to validate the representation of polar middle atmosphere dynamics in SD-WACCM4, a recently developed special version of the comprehensive state-of-the-art atmosphere model WACCM4. And fourth, model studies have been carried out to clarify the meaning of the descent rates of mesospheric air, which have been derived from CO time series in previous publications as well as in the present thesis. Each of these topics is summarized briefly in the following; more detailed summaries are found at the end of the respective chapters.

**The retrieval of CO vmr profiles** has been performed for the first two winters (2008/2009 and 2009/2010) of operational KIMRA measurements (Chap. 4). A detailed analysis of the retrieval characteristics has revealed that the KIMRA CO retrieval provides information between 40 km and 80 km altitude with a vertical resolution of 16 km to 22 km. Furthermore, it has been shown that such CO retrievals are particularly complex; residual CO signals from the thermosphere, where the increasing temperature causes ambiguities of the received linewidths, must be accounted for. An error assessment has been performed, showing that the main contributions to the total error arise from the noise on the spectra and the uncertainty of the temperature profiles used. All features of major interest of the polar winter dynamics have qualitatively been identified in the obtained CO time series: the descent of mesospheric air in fall, the SSWs, and the vortex breakups in spring.

**The first comparison of ground-based microwave observations with satellite observations** of middle atmosphere CO profiles has been carried out (Chap. 5). In particular, the KIMRA CO profiles have been compared to datasets of all three relevant satellite instruments, MLS, ACE-FTS and MIPAS. The comparison has revealed that KIMRA is generally consistent with the satellite datasets below 65 km. However, the KIMRA profile shape deviates systematically from those of the satellite datasets, causing the KIMRA profiles to be strongly high-biased above 70 km altitude. This bias is probably

connected to the residual contributions from the thermosphere to the received signal. However, the deviation does not affect the temporal variability of CO in the KIMRA dataset, which is the relevant point for the investigation of dynamical variability based on KIMRA CO.

**A validation of the polar middle atmosphere dynamics in SD-WACCM4** has been conducted (Chap. 6). SD-WACCM4 is a special version of NCAR's comprehensive chemistry-climate model WACCM4. It is nudged with analyzed meteorological data and is therefore directly comparable to measurements, in contrast to the free-running WACCM4. SD-WACCM4 has recently been developed, so that its validation is of high priority at present. One of the first comparisons to measurements has been performed in this thesis; based on the tracer properties of CO, the representation of polar middle atmosphere dynamics in SD-WACCM4 has been examined indirectly by comparing the simulated CO evolution to the KIMRA and MLS CO time series. This comparison benefits from the particular advantage of ground-based observations, which provide a consistent time series with high temporal resolution for a certain location. The comparison is therefore particularly challenging for the global model since it has only been evaluated at one model grid point, instead of, e.g., in a zonal mean sense. This grid point is closest to the measurement location in Kiruna, which is known to show particularly strong dynamical variability. The comparison has revealed that the polar winter middle atmosphere dynamics is very well represented in SD-WACCM4. Correlation coefficients between the modeled and the measured time series are as high as 0.9. The good agreement is particularly true for slowly varying behavior (time scales of 20 d and more), whereas the agreement of rapid variations drops with increasing altitude. This behavior has been attributed to the gravity wave parametrization in SD-WACCM4. Overall, this study strongly supports the expectation that SD-WACCM4 is a powerful tool for diagnosing the polar winter middle atmosphere.

**The meaning of descent rates of mesospheric air derived from CO time series** has been investigated (Chap 7). First, descent rates have been derived from the KIMRA CO time series using a common approach. The results generally agree with previous studies. However, it has been explained that a precise interpretation of descent rates derived from CO is generally unestablished; the observed CO may be affected by processes other than the descent, which would distort the attribution of the descent rates to actual vertical winds. This issue has been investigated with a modeling approach. CO from an SD-WACCM4 simulation, which is regarded as representing the real atmosphere, has been compared to a simulated ideal CO time series, which is certainly only influenced by vertical advection. It has been shown that, first, descent rates from local CO time series (representing ground-based observations) are comparable to those from zonal mean CO (representing satellite observations). Second, it has been shown that there is no period within the season during which CO-loss by other processes (mainly horizontal dynamics) can be neglected, in contrast to an assumption commonly made for at least the fall season. Therefore, descent rates represent, at best, the order of magnitude of the vertical wind velocity of the residual circulation. It has, however, been proposed that the descent rates might be a useful quantity themselves. They could be interpreted alternatively as the 'effective' velocity of mesospheric air, which explicitly considers the removal of fractions of the downwelling air. However, more details on processes acting horizontally across the vortex border must be known to confirm this interpretation.

---

**The implications and benefits for future research** of the individual results are discussed briefly in the following.

The IRF intends to continue the KIMRA CO observations on a long-term basis. The developed retrieval setup will therefore continue to be applied to retrieve the ongoing KIMRA observations and to generate a consistent long-term CO time series. Moreover, the experience gained with respect to the CO retrieval will be beneficial for the setup of long-term ground-based microwave CO observations in Ny Ålesund, Spitsbergen (79° N), which is intended by the Institute of Environmental Physics (IUP) at the University of Bremen. Furthermore, the already retrieved KIMRA CO time series itself as well as the developed comparison approaches will be of interest for future model comparisons. In particular, comparisons to the Bremen three-dimensional Chemistry Transport Model (B3DCTM) and the Karlsruhe Simulation Model of the Middle Atmosphere (KASIMA) are intended for the near-future.

The comparison of the KIMRA CO profiles to satellite observations is expected to be of particular interest in future. Since the recent generation of satellites will cease operation during the coming years and the next generation might not be operational early enough [personal communication with Christian von Savigny, IUP, University of Bremen, December 2011], the intercalibration between these satellite generations has to be based on long-term ground-based measurements. The preparation for this situation was not the major focus of this work. Nevertheless, the conducted satellite comparison has laid the foundation for applying the KIMRA dataset in this context. Generally, it can be seen from the present thesis that such an intercalibration on the basis of ground-based observations will not be straightforward. First, it is complicated by the different vertical coverages and the partly small number of coincidences between the individual datasets. Second, the systematic deviation of the profile shapes between KIMRA and the satellites might be an inherent property of the ground-based microwave CO observations. Other research groups that perform long-term ground-based microwave CO observations should therefore follow up on this comparison and repeat and refine the presented comparison approach with their data to check for consistency. To be prepared for the gap in satellite measurements, a reliable and consistent relationship between the present satellite observations and the individual ongoing ground-based long-term observations has to be established in the near future. In the context of an expected lack of satellite observations, another outcome of this work is of importance; namely that local CO time series, as seen by ground-based instruments, are comparable to zonal mean CO time series, which are usually derived from satellite observations (Chap 7). Analyses based on such time series can therefore be continued using ground-based observations.

The presented validation of SD-WACCM4 is expected to be of broad scientific interest because SD-WACCM4 is —as a new general-purpose tool— of relevance for many fields in atmospheric science. Particularly, the research on the special features of the polar middle atmosphere (descent of air, vortex strength, SSWs, and the vortex breakup) will benefit from the comparison presented; it demonstrates the very good representation of these features in the model, but also reveals the model limits. Furthermore, these results also support a productive application of this model for the research on interactions between dynamics, ozone, and climate change.

The investigation of an adequate interpretation of the descent rates derived from CO has shown that the feasibility of deducing pure vertical wind velocities from CO is limited

and available numbers should be handled with care. The demonstrated importance of dynamical influences on CO that are due to processes other than descent supports that future research should put additional emphasis on the exploration of the horizontal vortex dynamics. Only the consideration of the complete three-dimensional processes will allow further advancements in the quantification of the influence of descending mesospheric air. This field is known to bear many open questions and to be challenging for both observations and modeling. A promising approach is, however, the extensive analysis of the individual terms of the three-dimensional continuity equation for several species (CO, NO<sub>x</sub>, O<sub>3</sub> etc.) in model data, e.g., simulated with SD-WACCM4. This analysis is expected to provide new ideas concerning the properties of the polar vortex transport barrier and to stimulate maybe also new observation approaches.

# Appendix



# A Comparison of the time-averaged CO profiles including SD-WACCM4

This chapter is based on the publication by Hoffmann et al. [2012]. It is a brief extension to the validation of the CO representation in the model SD-WACCM4 (Chap. 6). Here, time-averaged profiles of the subsets SDWACCM and SDWACCM AREA (Sect. 6.2.1) are compared to those of KIMRA and MLS analog to the time-averaged profile comparison presented in Chap. 5. In contrast to the preprocessing applied there (Sect. 5.1), the upper profile parts are not replaced with the KIMRA a priori. This modification of the satellite profiles was only necessitated by the inclusion of the MIPAS and ACE-FTS datasets, which are not employed here. This means particularly that the MLS profiles can be used here in the complete relevant altitude range between 40 km to 80 km altitude.

The resulting time-averaged profiles (Fig. A.1, left) are based on an average over the 214 days with at least one profile per day in each dataset. In addition, the absolute deviations  $\Delta\chi_{\text{CO}}$  of the individual mean profiles from the KIMRA mean profile (Fig. A.1, right) were computed using Eq. (5.2).

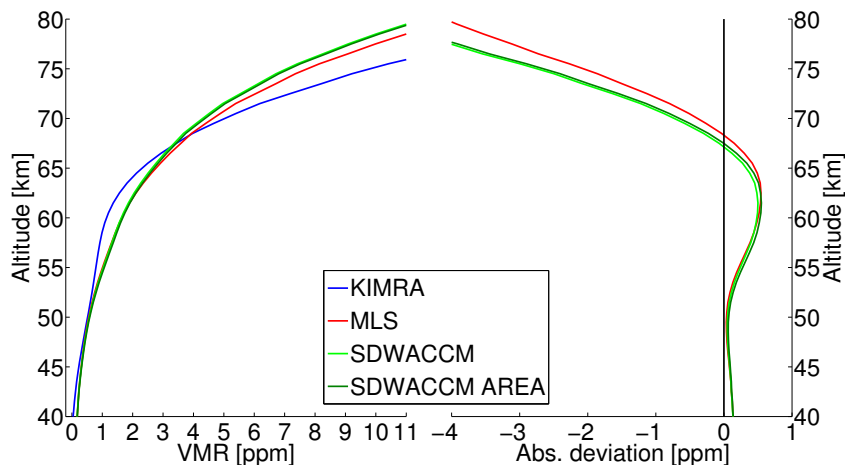


Figure A.1: Comparison of time-averaged profiles for all datasets included in the SD-WACCM4 validation (Chap. 6): KIMRA, MLS, SDWACCM, and SDWACCM AREA. **Left:** Mean profiles. **Right:** deviation  $\Delta\chi_{\text{CO}}$  between the profiles of KIMRA and the other datasets. Figure adopted from Hoffmann et al. [2012].

The comparison (Fig. A.1) reveals that the profile shape of KIMRA deviates from the other datasets, consistently with the findings of the satellite comparison (Chap. 5); whereas the SD-WACCM4 and the MLS profiles are more curved, the KIMRA profile

shows less CO increase with altitude below 60 km and a stronger increase with altitude above 60 km. This leads to an oscillatory shape of the deviation between KIMRA and the other datasets. Furthermore, KIMRA shows a high bias above approximately 70 km altitude, which increases with altitude.

The profile shapes of MLS and SDWACCM are consistent, but SDWACCM shows slightly lower CO vmr values starting at approximately 60 km and increasing with altitude to approximately 1 ppmv at 80 km altitude. This deviation cannot be attributed to a location mismatch since the SDWACCM AREA profile, for which the same collocation criteria as for MLS are applied, shows a similar deviation. However, in this comparison based on KIMRA, all profiles are smoothed with the KIMRA AVKs, so that the altitude resolution at 80 km is approximately 20 km and the origin of the discrepancy is also smoothed.

# List of Figures

2.1	Global and annual mean vertical temperature profile of the atmosphere . . .	6
2.2	Sketch of forces driving the middle atmosphere circulation . . . . .	10
2.3	Sketch of the middle atmosphere circulation . . . . .	11
2.4	Manifestation of the polar vortex in different atmospheric parameters . . .	15
2.5	Manifestation of an SSW in different atmospheric parameters . . . . .	17
2.6	Illustration of the influence of the meridional transport on tracers . . . . .	18
2.7	Illustration of the application of CO as tracer for vertical motions . . . . .	29
2.8	The first CO profiles obtained from ground-based microwave measurements of thermal emission lines . . . . .	30
4.1	Map of Europe showing the location of the KIMRA instrument . . . . .	48
4.2	Emission lines around 230 GHz . . . . .	49
4.3	Typical example of a measured and fitted spectrum . . . . .	53
4.4	Half widths of emission lines from different altitudes . . . . .	54
4.5	Average retrieval characteristics . . . . .	56
4.6	Example of AVK functions . . . . .	59
4.7	Factors for the conversion from the normalized to the vmr retrieval . . . . .	60
4.8	Typical examples of retrieved CO profiles . . . . .	61
4.9	Complete retrieved CO time series measured with KIMRA . . . . .	62
4.10	CO time series of the KIMRA period measured with MLS . . . . .	63
4.11	Typical examples of error contributions to the retrieved profiles . . . . .	65
4.12	Test of the retrieval stability under the influence of a changed a priori . . .	67
5.1	Investigation of the influence of the collocation area on the satellite com- parison results . . . . .	76
5.2	Investigation of the influence of the PV deviation on the satellite compar- ison results . . . . .	76
5.3	Investigation of a time dependence of the satellite comparison results . . .	78
5.4	Comparison of mean profiles from KIMRA with MIPAS NOM and MLS . . .	80
5.5	Comparison of mean profiles from KIMRA with ACE-FTS and MLS . . . . .	80
5.6	Comparison of mean profiles from KIMRA with MIPAS MA and MLS . . . . .	81
5.7	Comparison of mean profiles from KIMRA with ACE-FTS, MIPAS MA, and MLS . . . . .	81
6.1	Evolution of the CO vmr at 60 km as measured by KIMRA and MLS and as simulated by SD-WACCM4 . . . . .	89
6.2	Altitude profiles of the correlation coefficients for the comparison pairs KIMRA–SDWACCM, KIMRA–SDWACCM AREA, and KIMRA–MLS . . . . .	90
6.3	Detail of the sensitivity of the KIMRA measurements . . . . .	91

6.4	Differences between the correlation coefficients of KIMRA–MLS and KIMRA–SDWACCM . . . . .	92
6.5	Altitude profiles of the MLS–SDWACCM correlation coefficients . . . . .	93
6.6	Altitude profiles of the correlation coefficients as in Fig. 6.2, but for an alternative KIMRA–SDWACCM comparison (different nudging applied). . . . .	94
7.1	Descent rates $w_{CO}$ at 70 km altitude for the winter 2009/2010 derived from the CO datasets of KIMRA and SD-WACCM4 . . . . .	100
7.2	Realistic and ideal simulation of the CO evolution at the particular location of Kiruna . . . . .	104
7.3	Realistic and ideal simulation of the CO evolution as a zonal mean between 70°N and 80°N latitude . . . . .	105
7.4	Comparison of descent rates derived from CO and the TEM wind $\overline{w}^*$ . . . . .	107
A.1	Comparison of time-averaged profiles of KIMRA, MLS, SDWACCM, and SDWACCM AREA . . . . .	115

# List of Tables

4.1	Basic characteristics of the retrieved dataset. . . . .	50
4.2	Error contributions considered in the KIMRA error assessment . . . . .	64
4.3	Details of an experiment that investigates the a priori influence . . . . .	66
5.1	Properties of the satellite datasets considered in the satellite comparison . .	74
5.2	Summary of the satellite comparison experiments. . . . .	75
7.1	Publications including descent rates derived from CO . . . . .	99



# Acronyms

**ACE-FTS** Atmospheric Chemistry Experiment – Fourier Transform Spectrometer

**ADC** Analog-to-digital converter

**AOS** Acusto-optical spectrometer

**ARTS** Atmospheric radiative transfer simulator

**AVK** Averaging kernel

**B3DCTM** Bremen three-dimensional Chemistry Transport Model

**CAM** Community Atmosphere Model

**CCM** Chemistry-climate model

**CCSM** Community Climate System Model

**CESM** Community Earth System Model

**CFC** Chlorofluorocarbon

**CTM** Chemistry-transport model

**CTS** Chirp-transform spectrometer

**ECMWF** European Centre for Medium-Range Weather Forecasts

**EPP** Energetic particle precipitation

**ESSReS** Earth System Sciences Research School

**FASCOD** Fast Atmospheric Signature Code

**FFTS** Fast Fourier transform spectrometer

**FPGA** Field programmable gate array

**FTIR** Fourier transform infrared spectroscopy

**FWHM** Full width at half maximum

**GCM** General circulation model

- GEOS-5** Goddard Earth Observing System Model, version 5
- GMAO** Global Modeling and Assimilation Office
- GOMOS** Global Ozone Monitoring by Occultation of Stars
- HF** High-frequency variability
- HITRAN** High-resolution transmission molecular absorption database
- HWHM** Half width at half maximum
- IAA** Instituto de Astrofísica de Andalucía
- IMK** Institute for Meteorology and Climate Research
- IPCC** Intergovernmental Panel on Climate Change
- IRF** Swedish Institute of Space Physics (Institutet för rymdfysik)
- IUP** Institute of Environmental Physics (Institut für Umweltphysik)
- JPL** Jet Propulsion Laboratory
- KASIMA** Karlsruhe Simulation Model of the Middle Atmosphere
- KIMRA** Kiruna microwave radiometer
- KIT** Karlsruhe Institute of Technology
- LF** Low-frequency variability
- LO** Local oscillator
- MIPAS** Michelson Interferometer for Passive Atmospheric Sounding
- MIPAS MA** MIPAS middle atmosphere mode
- MIPAS NOM** MIPAS nominal mode
- MIPAS UA** MIPAS upper atmosphere mode
- MLS** Microwave Limb Sounder
- MLT** Mesosphere-lower thermosphere
- MOZART** Model for ozone and related chemical tracers
- NAT** Nitric acid trihydrate
- NCAR** National Center for Atmospheric Research

- NH** Northern Hemisphere
- OE** Optimal estimation
- PPM** Piecewise parabolic method
- PSC** Polar stratospheric cloud
- PV** Potential vorticity
- QBO** Quasi-biennial oscillation
- QDV** Quasi-decadal variability
- RAM** Radiometer for atmospheric measurements
- SABER** Sounding of the Atmosphere using Broadband Emission Radiometry
- SD** Specified dynamics
- SD-WACCM4** Specified Dynamics version of the Whole Atmosphere Community Climate Model, version 4
- SDWACCM** Subset of all CO profiles at the grid-point closest to Kiruna simulated with SD-WACCM4
- SDWACCM AREA** Subset of all CO profiles within in a circle around Kiruna simulated with SD-WACCM4
- SH** Southern Hemisphere
- SMR** Sub-Millimeter Radiometer
- SNR** Signal-to-noise ratio
- SSB** Single side band
- SST** Sea surface temperature
- SSW** Sudden stratospheric warming
- TEM** Transformed Eulerian-mean
- UV** Ultraviolet
- vmr** Volume mixing ratio
- WACCM4** Whole Atmosphere Community Climate Model, version 4



# Symbols

$\mathbf{A}$	Averaging kernel matrix
$\mathbf{A}_b$	Averaging kernel matrix with respect to forward model parameters
$A^{ij}$	Element of the averaging kernel matrix
$\mathbf{A}_{\text{norm}}$	Averaging kernel matrix normalized with a priori
$\mathbf{A}_{\text{vmr}}$	Averaging kernel matrix with respect to vmr profiles
$\alpha$	Absorption coefficient
$B$	Rotational constant
$B_\nu(T)$	Planck function
$\mathbf{b}$	True forward model parameters
$\hat{\mathbf{b}}$	Estimates of true forward model parameters
$\beta_D$	Doppler broadening parameter
$C$	Continuum Absorption coefficient
$c$	Speed of light
$c_p$	Specific heat of air under constant pressure
$\chi$	Volume mixing ratio
$\bar{\chi}$	Zonal mean volume mixing ratio
$\chi'$	Eddy disturbance of volume mixing ratio
$\chi_{\text{CO}}$	Volume mixing ratio of CO
$\bar{\chi}_{\text{CO}}$	Zonal mean volume mixing ratio of CO
$\bar{\chi}_{\text{CO}}^{\text{KIMRA}}$	Time-averaged volume mixing ratio profile of CO measured with KIMRA
$\bar{\chi}_{\text{CO}}^{\text{Sat}}$	Time-averaged volume mixing ratio profile of CO measured with a satellite
$\tilde{\chi}_{\text{CO}}$	Placeholder for volume mixing ratio of CO in a numerical simulation
$\mathbf{D}$	Contribution function matrix
$D_{\text{ur}}$	Unresolved diffusion term in the continuity equation
$\Delta\chi_{\text{CO}}$	Difference of volume mixing ratio profiles of CO measured with a satellite and KIMRA, respectively
$\Delta M_{\text{atm},r}$	Difference of raw spectra in balanced calibration
$\Delta\nu$	Spectral resolution of a spectrometer
$\Delta P$	Deviation of potential vorticity
$\Delta T_A$	Detection limit of a radiometer
$E_{\text{rot}}$	Energy eigenvalues for rotational transitions
$\epsilon$	Measurement noise on a spectrum in retrieval theory
$\mathbf{F}$	Forward model in retrieval theory

$F(\nu, \nu_{fi})$	Line shape function for the transition between the states $f$ and $i$
$f$	Coriolis parameter
$F_D$	Doppler line shape function
$\mathbf{F}_{EP}$	Eliassen-Palm flux vector
$F_L$	Lorentz line shape function
$F_V$	Voigt line shape function
$g_0$	Standard gravity due to free fall
$\gamma_a$	Air broadening parameter
$\gamma_c$	Collisional half width of pressure broadened line
$\gamma_D$	Half width of Doppler broadened line
$\gamma_v$	Half width of Voigt broadened line
$H$	Scale height (usually 7 km for the middle atmosphere)
$h$	Planck's constant
$H_{rot}$	Rotational Hamiltonian
$\mathbf{I}$	Unity matrix
$I_\nu$	Specific intensity
$J$	Rotational quantum number
$J_C$	Cost function in retrieval theory
$\mathbf{K}$	Jacobian of the forward model
$\mathbf{K}_b$	Jacobian of the forward model with respect to the forward model parameters
$k_B$	Boltzmann's constant
$\lambda$	Longitude
$\mathbf{M}$	TEM eddy flux vector
$m$	Mass of molecule
$M_{atm}$	Uncalibrated spectrum of an atmospheric measurement
$M_c$	Uncalibrated spectrum of a 'cold' black body for the hot-cold-calibration
$M_h$	Uncalibrated spectrum of a 'hot' black body for the hot-cold-calibration
$M_r$	Uncalibrated spectrum of the reference source for the balanced calibration
$n_a$	Temperature exponent of the air broadening parameter
$n_{Air}$	Total number density of the air in a given volume
$n_T$	Number density of a trace constituent in a given volume
$\nu$	Frequency
$\nu_{fi}$	Frequency of transition between the states $f$ and $i$
$\Omega$	Angular speed of the rotation of the earth
$\omega_a$	Absolute vorticity
$P$	Potential vorticity
$p$	Air pressure

---

$p_0$	Some standard pressure (usually 1000 hPa)
$\phi$	Latitude
$\Psi$	Quantum mechanical wave function of a molecule
$R$	Gas constant for air
$r$	Earth's radius
$r_{\text{coll}}$	Radius of collocation circle around Kiruna
$\rho$	Mass density of air
$\rho_0$	Basic mass density of air
$S$	Source term in the continuity equation
$\bar{S}$	Zonal mean source term in the continuity equation
$\mathbf{S}_a$	A priori covariance matrix
$\mathbf{S}_b$	Covariance matrix of the forward model parameters
$\mathbf{S}_\epsilon$	Measurement noise covariance matrix
$\mathbf{S}_\eta$	Covariance matrix of the retrieved profile with respect to the measurement noise
$S_{fi}$	Line intensity for the transition between the states $f$ and $i$
$\mathbf{S}_{\text{fp}}$	Covariance matrix of the retrieved profile with respect to the forward model parameter uncertainties
$\sigma_\eta$	Error of the retrieved profile caused by the measurement noise
$\sigma_{\text{fp}}$	Error of the retrieved profile caused by the errors of the forward model parameters
$\sigma_{\gamma_a}$	Error of the retrieved profile caused by the errors of the used air broadening parameter
$\sigma_{S_{\text{fi}}}$	Error of the retrieved profile caused by the errors of the used line intensity
$\sigma_{n_a}$	Error of the retrieved profile caused by the errors of the used temperature exponent of the air broadening parameter
$\sigma_T$	Error of the retrieved profile caused by the errors of the atmospheric temperature profiles used
$\sigma_{T_C}$	Error of the retrieved profile caused by the error of the calibration of the spectra
$\sigma_{\text{tot}}$	Total error of the retrieved profile
$T$	Temperature
$t$	Time
$T_A$	Antenna temperature
$T_b$	Equivalent brightness temperature
$T_c$	Temperature of a 'cold' black body for the hot-cold-calibration
$T_h$	Temperature of a 'hot' black body for the hot-cold-calibration
$t_{\text{int}}$	Integration time of a measurement
$T_{\text{rec}}$	Receiver temperature

$\bar{T}_S$	Standard mean temperature of the middle atmosphere (usually 240 K)
$T_{\text{sys}}$	System temperature
$T_r$	Temperature of the reference source for a balanced calibration
$\tau$	Optical depth
$\theta$	Potential temperature
$\bar{\theta}$	Zonal mean potential temperature
$u$	Zonal wind
$\bar{u}$	Zonal mean zonal wind
$v$	Meridional wind
$\bar{v}$	Zonal mean meridional wind
$\bar{v}^*$	Meridional wind in TEM formalism
$\overline{v'u'}$	Eddy momentum flux
$\overline{v'\theta'}$	Eddy heat flux
$V_{\text{PSC}}$	Volume of potential PSC formation
$w$	Vertical wind
$\bar{w}$	Zonal mean vertical wind
$\bar{w}^*$	Vertical wind in TEM formalism
$w_{\text{CO}}$	Descent rate derived from a CO time series
$\tilde{w}$	Placeholder for vertical wind used in a numerical simulation
$x$	Zonal coordinate in a local Cartesian coordinate system
$\mathbf{x}$	State of the atmosphere in retrieval theory
$\mathbf{x}_a$	A priori profile
$x_a^i$	Element of the a priori profile in retrieval theory
$\hat{\mathbf{x}}$	Retrieved state of the atmosphere in retrieval theory
$\hat{x}^i$	Element of the retrieved state of the atmosphere in retrieval theory
$Y$	Y-factor in measurement of the receiver temperature
$y$	Meridional coordinate in a local Cartesian coordinate system
$\mathbf{y}$	Microwave spectrum in retrieval theory
$z$	Geometric altitude
$z^i$	Element of the vertical retrieval grid

# Bibliography

- C. P. Aellig, N. Kämpfer, and A. Hauchecorne. Variability of mesospheric CO in the fall and winter as observed with ground-based microwave radiometry at 115 GHz. *J. Geophys. Res.*, 100:14125–14130, 1995.
- D. Allen, J. Stanford, M. Lopez-Valverde, N. Nakamura, D. Lary, A. Douglass, M. Cerniglia, J. Remedios, and F. Taylor. Observations of middle atmosphere CO from the UARS ISAMS during the early northern winter 1991/92. *J. Atmos. Sci.*, 56:563–583, 1999.
- D. Allen, J. Stanford, N. Nakamura, M. López-Valverde, M. López-Puertas, F. Taylor, and J. Remedios. Antarctic polar descent and planetary wave activity observed in ISAMS CO from April to July 1992. *Geophys. Res. Lett.*, 27:665–668, 2000.
- M. Allen, Y. L. Yung, and J. W. Waters. Vertical transport and photochemistry in the terrestrial mesosphere and lower thermosphere (50-120 km). *J. Geophys. Res.*, 86:3617–3627, 1981.
- G. P. Anderson, S. A. Clough, F. X. Kneizys, J. H. Chetwynd, and E. P. Shettle. AFGL atmospheric constituent profiles (0-120 km). Technical Report TR-86-0110, AFGL, 1986.
- D. Andrews, J. Holten, and C. Leovy. *Middle Atmosphere Dynamics*. Academic Press, 1987.
- A. O. Benz, P. C. Grigis, V. Hungerbühler, H. Meyer, C. Monstein, B. Stuber, and D. Zardet. A broadband FFT spectrometer for radio and millimeter astronomy. *Astron. Astrophys.*, 442:767–773, 2005. doi: 10.1051/0004-6361:20053568.
- H. Berg. *Weiterentwicklung der Millimeterwellenradiometrie stratosphärischer Spurengase in Emission und Absorption*. PhD thesis, Institut für Meteorologie und Klimaforschung, Forschungszentrum Karlsruhe GmbH, 2000.
- H. Berg, R. Krupa, G. Hochschild, G. Kopp, and M. Kuntz. Millimeter wave radiometer with adjustable internal calibration load for high resolution measurements of stratospheric constituents. In *Proceedings of 2nd ESA Workshop on Millimetre Wave Technology and Applications: Antennas, Circuits and Systems*, pages 372–377, 1998.
- R. M. Bevilacqua, A. A. Stark, and P. R. Schwartz. The variability of carbon monoxide in the terrestrial mesosphere as determined from ground-based observations of the  $J = 1 \rightarrow 0$  emission line. *J. Geophys. Res.*, 90:5777–5782, 1985.
- H. Bönisch, A. Engel, T. Birner, P. Hoor, D. W. Tarasick, and E. A. Ray. On the structural changes in the Brewer-Dobson circulation after 2000. *Atmos. Chem. Phys.*, 11:3937–3948, 2011.
- B. Boroson, T. Kallman, J. M. Blondin, and M. P. Owen. Testing hydrodynamic models of LMC X-4 with ultraviolet and X-Ray spectra. *Astrophys. J.*, 550:919–930, 2001. doi: 10.1086/319773.

- T. Borsdorff and R. Sussmann. On seasonality of stratomesospheric CO above midlatitudes: New insight from solar FTIR spectrometry at Zugspitze and Garmisch. *Geophys. Res. Lett.*, 36:L21804, 2009. doi: 10.1029/2009GL040056.
- A. Bott. A positive definite advection scheme obtained by nonlinear renormalization of the advective fluxes. *Mon. Weather Rev.*, 117:1006–1016, 1989. doi: 10.1175/1520-0493(1989)117<(\$1006:APDASO\$)\$2.0.CO;2.
- I. S. Boyd, A. D. Parrish, L. Froidevaux, T. von Clarmann, E. Kyrölä, J. M. Russell, and J. M. Zawodny. Ground-based microwave ozone radiometer measurements compared with Aura-MLS v2.2 and other instruments at two network for detection of atmospheric composition change sites. *J. Geophys. Res.*, 112:D24S33, 2007. doi: 10.1029/2007JD008720.
- G. P. Brasseur and S. Solomon. *Aeronomy of the Middle Atmosphere*. Springer, 3 edition, 2005.
- A. W. Brewer. Evidence for a world circulation provided by the measurements of helium and water vapour distribution in the stratosphere. *Q. J. Roy. Meteor. Soc.*, 75:351–363, 1949. doi: 10.1002/qj.49707532603.
- S. Bühler, P. Eriksson, T. Kuhn, A. von Engeln, and C. Verdes. ARTS, the atmospheric radiative transfer simulator. *J. Quant. Spectrosc. Ra.*, 91:65–93, 2005. doi: 10.1016/j.jqsrt.2004.05.051.
- S. Chapman. On ozone and atomic oxygen in the upper atmosphere. *Philos. Mag.*, 10:369–383, 1930. doi: 10.1080/14786443009461588.
- R. T. Clancy, D. O. Muhleman, and G. L. Berge. Microwave spectra of terrestrial mesospheric CO. *J. Geophys. Res.*, 87:5009–5014, 1982.
- C. Clerbaux, M. George, S. Turquety, K. A. Walker, B. Barret, P. Bernath, C. Boone, T. Borsdorff, J. P. Cammas, V. Catoire, M. Coffey, P. F. Coheur, M. Deeter, M. De Maziere, J. Drummond, P. Duchatelet, E. Dupuy, R. de Zafra, F. Eddounia, D. P. Edwards, L. Emmons, B. Funke, J. Gille, D. W. T. Griffith, J. Hannigan, F. Hase, M. Hoepfner, N. Jones, A. Kagawa, Y. Kasai, I. Kramer, E. Le Flochmoen, N. J. Livesey, M. Lopez-Puertas, M. Luo, E. Mahieu, D. Murtagh, P. Nedelec, A. Pazmino, H. Pumphrey, P. Ricaud, C. P. Rinsland, C. Robert, M. Schneider, C. Senten, G. Stiller, A. Strandberg, K. Strong, R. Sussmann, V. Thouret, J. Urban, and A. Wiacek. CO measurements from the ACE-FTS satellite instrument: data analysis and validation using ground-based, airborne and spaceborne observations. *Atmos. Chem. Phys.*, 8:2569–2594, 2008.
- P. Colella and P. R. Woodward. The piecewise parabolic method (PPM) for gas-dynamical simulations. *J. Comput. Phys.*, 54:174–201, 1984. doi: 10.1016/0021-9991(84)90143-8.
- R. L. de Zafra and G. Muscari. CO as an important high-altitude tracer of dynamics in the polar stratosphere and mesosphere. *J. Geophys. Res.*, 109:D06105, 2004. doi: 10.1029/2003JD004099.
- C. Di Biagio, G. Muscari, A. di Sarra, R. L. de Zafra, P. Eriksen, G. Fiocco, I. Fiorucci, and D. Fuà. Evolution of temperature, O<sub>3</sub>, CO, and N<sub>2</sub>O profiles during the exceptional 2009 Arctic major stratospheric warming as observed by lidar and millimeter-wave spectroscopy at Thule (76.5°N, 68.8°W), Greenland. *J. Geophys. Res.*, 115:D24315, 2010. doi: 10.1029/2010JD014070.

- G. M. B. Dobson. Origin and distribution of the polyatomic molecules in the atmosphere. *P. Roy. Soc. Lond. A Mat.*, 236:187–193, 1956.
- D. G. Dritschel and M. E. McIntyre. Multiple jets as PV staircases: The phillips effect and the resilience of Eddy-Transport barriers. *J. Atmos. Sci.*, 65:855–874, 2008. doi: 10.1175/2007JAS2227.1.
- E. Dupuy, J. Urban, P. Ricaud, E. Le Flochmoem, N. Lautie, D. Murtagh, J. De La Noe, L. El Amraoui, P. Eriksson, P. Forkman, U. Frisk, F. Jegou, C. Jimenez, and M. Olberg. Strato-mesospheric measurements of carbon monoxide with the Odin Sub-Millimetre Radiometer: Retrieval and first results. *Geophys. Res. Lett.*, 31:L20101, 2004. doi: 10.1029/2004GL020558.
- D. H. Ehhalt, L. E. Heidt, R. H. Lueb, and W. Pollock. The vertical distribution of trace gases in the stratosphere. *Pure Appl. Geophys.*, 113:389–402, 1975. doi: 10.1007/BF01592926.
- L. K. Emmons, S. Walters, P. G. Hess, J.-F. Lamarque, G. G. Pfister, D. Fillmore, C. Granier, A. Guenther, D. Kinnison, T. Laepple, J. Orlando, X. Tie, G. Tyndall, C. Wiedinmyer, S. L. Baughcum, and S. Kloster. Description and evaluation of the Model for Ozone and Related chemical Tracers, version 4 (MOZART-4). *Geosci. Model Dev.*, 3:43–67, 2010. doi: 10.5194/gmd-3-43-2010.
- P. Eriksson, C. Jiménez, and S. A. Bühler. Qpack, a general tool for instrument simulation and retrieval work. *J. Quant. Spectrosc. Ra.*, 91:47–64, 2005. doi: 10.1016/j.jqsrt.2004.05.050.
- P. Eriksson, M. Ekström, C. Melsheimer, and S. A. Buehler. Efficient forward modelling by matrix representation of sensor responses. *Int. J. Remote Sens.*, 27:1793–1808, 2006. doi: 10.1080/01431160500447254.
- J. C. Farman, B. G. Gardiner, and J. D. Shanklin. Large losses of total ozone in Antarctica reveal seasonal ClO<sub>x</sub>/NO<sub>x</sub> interaction. *Nature*, 315:207–210, 1985. doi: 10.1038/315207a0.
- P. Forkman, P. Eriksson, A. Winnberg, R. R. Garcia, and D. Kinnison. Longest continuous ground-based measurements of mesospheric CO. *Geophys. Res. Lett.*, 30:1532, 2003. doi: 10.1029/2003GL016931.
- P. Forkman, P. Eriksson, D. Murtagh, and P. Espy. Observing the vertical branch of the mesospheric circulation at latitude 60°N using ground-based measurements of CO and H<sub>2</sub>O. *J. Geophys. Res.*, 110:D05107, 2005. doi: 10.1029/2004JD004916.
- D. C. Fritts, S. L. Vadas, K. Wan, and J. A. Werne. Mean and variable forcing of the middle atmosphere by gravity waves. *J. Atmos. Sol.-Terr. Phy.*, 68:247–265, 2006. doi: 10.1016/j.jastp.2005.04.010.
- B. Funke, M. López-Puertas, M. García-Comas, G. P. Stiller, T. von Clarmann, M. Höpfner, N. Glatthor, U. Grabowski, S. Kellmann, and A. Linden. Carbon monoxide distributions from the upper troposphere to the mesosphere inferred from 4.7 μm non-local thermal equilibrium emissions measured by MIPAS on Envisat. *Atmos. Chem. Phys.*, 9:2387–2411, 2009.
- B. Funke, A. Baumgaertner, M. Calisto, T. Egorova, C. H. Jackman, J. Kieser, A. Krivolutsky, M. López-Puertas, D. R. Marsh, T. Reddmann, E. Rozanov, S.-M. Salmi, M. Sinnhuber, G. P. Stiller, P. T. Verronen, S. Versick, T. von Clarmann, T. Y. Vyushkova, N. Wieters, and J. M.

- Wissing. Composition changes after the "Halloween" solar proton event: the High Energy Particle Precipitation in the Atmosphere (HEPPA) model versus MIPAS data intercomparison study. *Atmos. Chem. Phys.*, 11:9089–9139, 2011. doi: 10.5194/acp-11-9089-2011.
- R. R. Garcia and W. J. Randel. Acceleration of the Brewer-Dobson circulation due to increases in greenhouse gases. *J. Atmos. Sci.*, 65:2731–2739, 2008. doi: 10.1175/2008JAS2712.1.
- R. R. Garcia and S. Solomon. The effect of breaking gravity waves on the dynamics and chemical composition of the mesosphere and lower thermosphere. *J. Geophys. Res.*, 90:3850–3868, 1985. doi: 10.1029/JD090iD02p03850.
- R. R. Garcia, D. R. Marsh, D. E. Kinnison, B. A. Boville, and F. Sassi. Simulation of secular trends in the middle atmosphere, 1950-2003. *J. Geophys. Res.*, 112:D09301, 2007. doi: 10.1029/2006JD007485.
- P. R. Gent, G. Danabasoglu, L. J. Donner, M. M. Holland, E. C. Hunke, S. R. Jayne, D. M. Lawrence, R. B. Neale, P. J. Rasch, M. Vertenstein, P. H. Worley, Z. Yang, and M. Zhang. The Community Climate System Model Version 4. *J. Climate*, 24:4973–4991, 2011. doi: 10.1175/2011JCLI4083.1.
- S. H. W. Golchert. *Stratospheric Water Vapour in the Tropics - Observations by Ground-Based Microwave Radiometry*. PhD thesis, University of Bremen, 2009.
- P. Goldsmith, M. Litvak, R. Plambeck, and D. Williams. Carbon monoxide mixing ratio in the mesosphere derived from ground-based microwave-measurements. *J. Geophys. Res.*, 84: 416–418, 1979.
- K. U. Grossmann, O. Gusev, and P. Knieling. The distribution of carbon monoxide in the upper mesosphere and lower thermosphere during CRISTA-1 and -2. *J. Atmos. Sol.-Terr. Phys.*, 68: 1764–1780, 2006. doi: {10.1016/j.jastp.2006.05.022}.
- K. Hamilton. Free and forced interannual variability of the circulation in the extratropical northern hemisphere middle atmosphere. In D. E. Siskind, S. D. Eckermann, and M. E. Summers, editors, *Atmospheric Science Across the Stratopause. Geophysical Monograph 123*, pages 227–239. American Geophysical Union, 2000.
- P. H. Haynes, M. E. McIntyre, T. G. Shepherd, C. J. Marks, and K. P. Shine. On the "Downward Control" of extratropical diabatic circulations by Eddy-Induced mean zonal forces. *J. Atmos. Sci.*, 48:651–678, 1991. doi: 10.1175/1520-0469(1991)048<0651:OTCOED>2.0.CO;2.
- P. B. Hays and J. J. Olivero. Carbon dioxide and monoxide above the troposphere. *Planet. Space Sci.*, 18:1729–1733, 1970.
- C. G. Hoffmann, U. Raffalski, M. Palm, B. Funke, S. H. W. Golchert, G. Hochschild, and J. Notholt. Observation of strato-mesospheric CO above Kiruna with ground-based microwave radiometry — retrieval and satellite comparison. *Atmos. Meas. Tech.*, 4:2389–2408, 2011. doi: 10.5194/amt-4-2389-2011.
- C. G. Hoffmann, D. E. Kinnison, R. R. Garcia, M. Palm, J. Notholt, U. Raffalski, and G. Hochschild. CO at 40-80 km above Kiruna observed by the ground-based microwave radiometer KIMRA and simulated by the Whole Atmosphere Community Climate Model. *Atmos. Chem. Phys. Discuss.*, 12:559–587, 2012. doi: 10.5194/acpd-12-559-2012.

- C. G. Hoffmann, M. Palm, J. Notholt, U. Raffalski, and G. Hochschild. A brief example on the application of remotely sensed tracer observations in atmospheric science — studying the impact of stratosphere-mesosphere coupling on polar ozone variability. In G. Lohmann, D. Wolf-Gladrow, J. Notholt, V. Unnithan, K. Grosfeld, and A. Wegner, editors, *Earth System Sciences: Bridging the gaps between disciplines — A multi-disciplinary Helmholtz Graduate Research School*. Springer, submitted (publication scheduled for 2012).
- J. Holton. *An Introduction to Dynamic Meteorology*. Elsevier, 2004.
- J. R. Holton and M. J. Alexander. The role of waves in the transport circulation of the middle atmosphere. In D. E. Siskind, S. D. Eckermann, and M. E. Summers, editors, *Atmospheric Science Across the Stratopause. Geophysical Monograph 123*, pages 21–35. American Geophysical Union, 2000.
- M. A. Janssen, editor. *Atmospheric Remote Sensing by Microwave Radiometry*. John Wiley & Sons, Inc., 1993.
- Y. J. Kasai, T. Koshiro, M. Endo, N. B. Jones, and Y. Murayama. Ground-based measurement of strato-mesospheric CO by a FTIR spectrometer over Poker Flat, Alaska. *Adv. Space. Res.*, 35:2024–2030, 2005. doi: 10.1016/j.asr.2005.04.099.
- D. E. Kinnison, G. P. Brasseur, S. Walters, R. R. Garcia, D. R. Marsh, F. Sassi, V. L. Harvey, C. E. Randall, L. Emmons, J. F. Lamarque, P. Hess, J. J. Orlando, X. X. Tie, W. Randel, L. L. Pan, A. Gettelman, C. Granier, T. Diehl, U. Niemeier, and A. J. Simmons. Sensitivity of chemical tracers to meteorological parameters in the MOZART-3 chemical transport model. *J. Geophys. Res.*, 112:D20302, 2007. doi: 10.1029/2006JD007879.
- U. Klein. *Aufbau und Betrieb eines breitbandigen, bodengestützten Millimeterwellen-Radiometers zur Messung atmosphärischer Spurenstoffe*. PhD thesis, University of Bremen, 1993.
- R. Krupa. *Millimeterwellen-Radiometrie stratosphärischer Spurengase unter Anwendung balancierter Kalibrierung*. PhD thesis, Universität Fridericiana Karlsruhe, 1998.
- R. Krupa, G. Hochschild, H. Fischer, and W. Wiesbeck. Balanced calibration technique with an internal reference load for ground based millimeter wave radiometry. In *IEEE International Geoscience and Remote Sensing Symposium Proceedings*, volume I, 1998.
- K. F. Künzi and E. R. Carlson. Atmospheric CO volume mixing ratio profiles determined from ground-based measurements of the  $J = 1 \rightarrow 0$  and  $J = 2 \rightarrow 1$  emission lines. *J. Geophys. Res.*, 87:7235–7241, 1982.
- K. Labitzke. Stratospheric-Mesospheric Midwinter Disturbances: A Summary Of Observed Characteristics. *J. Geophys. Res.-Oceans Atmos.*, 86:9665–9678, 1981.
- K. Labitzke and M. Kunze. On the remarkable Arctic winter in 2008/2009. *J. Geophys. Res.*, 114:D00I02, 2009. doi: 10.1029/2009JD012273.
- J. F. Lamarque, L. K. Emmons, P. G. Hess, D. E. Kinnison, S. Tilmes, F. Vitt, C. L. Heald, E. A. Holland, P. H. Lauritzen, J. Neu, J. J. Orlando, P. Rasch, and G. Tyndall. CAM-chem: description and evaluation of interactive atmospheric chemistry in CESM. *Geosci. Model Dev. Discuss.*, 4:2199–2278, 2011. doi: 10.5194/gmdd-4-2199-2011.

- D. J. Lary. Catalytic destruction of stratospheric ozone. *J. Geophys. Res.*, 102:21,515–21,526, 1997.
- R. S. Lindzen. Turbulence and stress owing to gravity wave and tidal breakdown. *J. Geophys. Res.*, 86:9707–9714, 1981. doi: 10.1029/JC086iC10p09707.
- N. Livesey, W. Read, L. Froidevaux, A. Lambert, G. Manney, H. Pumphrey, M. Santee, M. Schwartz, S. Wang, R. Cofield, D. Cuddy, R. Fuller, R. Jarnot, J. Jiang, B. Knosp, P. Stek, P. Wagner, and D. Wu. Aura Microwave Limb Sounder (MLS) — version 3.3 level 2 data quality and description document. Technical Report JPL D-33509, Jet Propulsion Laboratory, California Institute of Technology, 2011.
- M. A. López-Valverde, M. López-Puertas, J. J. Remedios, C. D. Rodgers, F. W. Taylor, E. C. Zipf, and P. W. Erdman. Validation of measurements of carbon monoxide from the improved stratospheric and mesospheric sounder. *J. Geophys. Res.*, 101:9929–9955, 1996.
- G. L. Manney, R. W. Zurek, L. Froidevaux, J. W. Waters, A. O’Neill, and R. Swinbank. Lagrangian transport calculations using UARS data. Part II: ozone. *J. Atmos. Sci.*, 52:3069–3081, 1995. doi: 10.1175/1520-0469(1995)052<3069:LTCUDP>2.0.CO;2.
- G. L. Manney, M. J. Schwartz, K. Krüger, M. L. Santee, S. Pawson, J. N. Lee, W. H. Daffer, R. A. Fuller, and N. J. Livesey. Aura Microwave Limb Sounder observations of dynamics and transport during the record-breaking 2009 Arctic stratospheric major warming. *Geophys. Res. Lett.*, 36:L12815, 2009. doi: 10.1029/2009GL038586.
- G. L. Manney, M. L. Santee, M. Rex, N. J. Livesey, M. C. Pitts, P. Veefkind, E. R. Nash, I. Wohltmann, R. Lehmann, L. Froidevaux, L. R. Poole, M. R. Schoeberl, D. P. Haffner, J. Davies, V. Dorokhov, H. Gernandt, B. Johnson, R. Kivi, E. Kyro, N. Larsen, P. F. Levelt, A. Makshtas, C. T. McElroy, H. Nakajima, M. C. Parrondo, D. W. Tarasick, P. von der Gathen, K. A. Walker, and N. S. Zinoviev. Unprecedented Arctic ozone loss in 2011. *Nature*, 478:469–475, 2011. doi: 10.1038/nature10556.
- D. Marsh. *Aeronomy of the Earth’s Atmosphere and Ionosphere*, volume 2 of *IAGA Special Sopron Book Series*, chapter Chemical-dynamical coupling in the Mesosphere and Lower Thermosphere, pages 3–17. Springer, 1 edition, 2011.
- M. McIntyre. Dynamic meteorology / potential vorticity. In J. Holton, editor, *Encyclopedia of Atmospheric Sciences*, pages 685–694. Academic Press, Oxford, 2003. ISBN 978-0-12-227090-1.
- M. McIntyre and T. Palmer. The ‘surf zone’ in the stratosphere. *J. Atmos. Terr. Phys.*, 46: 825–849, 1984. doi: 10.1016/0021-9169(84)90063-1.
- M. E. McIntyre and T. N. Palmer. Breaking planetary waves in the stratosphere. *Nature*, 305: 593–600, 1983. doi: 10.1038/305593a0.
- Y. J. Meijer, D. P. J. Swart, M. Allaart, S. B. Andersen, G. Bodeker, I. Boyd, G. Braathen, Y. Calisesi, H. Claude, V. Dorokhov, P. von der Gathen, M. Gil, S. Godin-Beekmann, F. Goutail, G. Hansen, A. Karpetchko, P. Keckhut, H. M. Kelder, R. Koelemeijer, B. Kois, R. M. Koopman, G. Kopp, J. Lambert, T. Leblanc, I. S. McDerimid, S. Pal, H. Schets, R. Stubi, T. Suortti, G. Visconti, and M. Yela. Pole-to-pole validation of envisat GOMOS ozone profiles using data from ground-based and balloon sonde measurements. *J. Geophys. Res.*, 109:D23305, 2004. doi: 10.1029/2004JD004834.

- C. Melsheimer, C. Verdes, S. A. Buehler, C. Emde, P. Eriksson, D. G. Feist, S. Ichizawa, V. O. John, Y. Kasai, G. Kopp, N. Koulev, T. Kuhn, O. Lemke, S. Ochiai, F. Schreier, T. R. Sreerexha, M. Suzuki, C. Takahashi, S. Tsujimaru, and J. Urban. Intercomparison of general purpose clear sky atmospheric radiative transfer models for the millimeter/submillimeter spectral range. *Radio Sci.*, 40:RS1007, 2005. doi: 10.1029/2004RS003110.
- K. Minschwaner, G. L. Manney, N. J. Livesey, H. C. Pumphrey, H. M. Pickett, L. Froidevaux, A. Lambert, M. J. Schwartz, P. F. Bernath, K. A. Walker, and C. D. Boone. The photochemistry of carbon monoxide in the stratosphere and mesosphere evaluated from observations by the Microwave Limb Sounder on the Aura satellite. *J. Geophys. Res.*, 115:D13303, 2010. doi: 10.1029/2009JD012654.
- P. W. Mote, K. H. Rosenlof, M. E. McIntyre, E. S. Carr, J. C. Gille, J. R. Holton, J. S. Kinnersley, H. C. Pumphrey, J. M. Russell, and J. W. Waters. An atmospheric tape recorder: The imprint of tropical tropopause temperatures on stratospheric water vapor. *J. Geophys. Res.*, 101:3989–4006, 1996.
- S. Müller, A. Murk, C. Monstein, and N. Kämpfer. Intercomparison of digital fast Fourier transform and acoustooptical spectrometers for microwave radiometry of the atmosphere. *IEEE Trans. Geosci. Remote Sens.*, 47:2233–2239, 2009.
- E. Nash, P. Newman, J. Rosenfield, and M. Schoeberl. An objective determination of the polar vortex using Ertel’s potential vorticity. *J. Geophys. Res.-Atmos.*, 101:9471–9478, 1996.
- R. B. Neale, C. C. Chen, A. Gettelman, P. H. Lauritzen, S. Park, D. L. Williamson, A. J. Conley, R. R. Garcia, D. E. Kinnison, J. F. Lamarque, D. R. Marsh, M. Mills, A. K. Smith, S. Tilmes, F. Vitt, H. Morrison, P. Cameron-Smith, W. D. Collins, M. J. Iacono, R. C. Easter, S. J. Ghan, X. Liu, P. J. Rasch, and M. A. Taylor. Description of the NCAR Community Atmosphere Model (CAM 5.0). Technical Report NCAR/TN-486+STR, National Center for Atmospheric Research, 2010.
- R. B. Neale, J. Richter, S. Park, P. H. Lauritzen, S. J. Vavrus, P. J. Rasch, and M. Zhang. The Mean Climate of the Community Atmosphere Model (CAM4) in Forced SST and Fully Coupled Experiments. *J. Climate*, submitted, 2011.
- P. A. Newman, J. F. Gleason, R. D. McPeters, and R. S. Stolarski. Anomalously low ozone over the Arctic. *Geophys. Res. Lett.*, 24:2689–2692, 1997. doi: 10.1029/97GL52831.
- J. Olivero and R. Longbothum. Empirical fits to the Voigt line width: A brief review. *J. Quant. Spectrosc. Ra.*, 17:233–236, 1977. doi: doi:10.1016/0022-4073(77)90161-3.
- M. Palm, C. G. Hoffmann, S. H. W. Golchert, and J. Notholt. The ground-based MW radiometer OZORAM on Spitsbergen — description and status of stratospheric and mesospheric O<sub>3</sub>-measurements. *Atmos. Meas. Tech.*, 3:1533–1545, 2010. doi: 10.5194/amt-3-1533-2010.
- A. Parrish, R. L. de Zafra, P. M. Solomon, and J. W. Barrett. A ground-based technique for millimeter wave spectroscopic observations of stratospheric trace constituents. *Radio Sci.*, 23: 106–118, 1988.
- J. Pearson, H. Müller, H. Pickett, E. Cohen, and B. Drouin. Introduction to submillimeter, millimeter and microwave spectral line catalog. *J. Quant. Spectrosc. Ra.*, 111:1614–1616, 2010. doi: 10.1016/j.jqsrt.2010.02.002.

- M. C. Pitts, L. R. Poole, A. Dörnbrack, and L. W. Thomason. The 2009-2010 Arctic polar stratospheric cloud season: a CALIPSO perspective. *Atmos. Chem. Phys.*, 11:2161–2177, 2011. doi: 10.5194/acp-11-2161-2011.
- H. C. Pumphrey, M. J. Filipiak, N. J. Livesey, M. J. Schwartz, C. Boone, K. A. Walker, P. Bernath, P. Ricaud, B. Barret, C. Clerbaux, R. F. Jarnot, G. L. Manney, and J. W. Waters. Validation of middle-atmosphere carbon monoxide retrievals from the Microwave Limb Sounder on Aura. *J. Geophys. Res.-Atmos.*, 112:D24S38, 2007. doi: 10.1029/2007JD008723.
- U. Raffalski, H. Berg, G. Hochschild, and G. Kopp. Continuous ozone measurements over Kiruna during winter/spring 2002: A new millimeter wave radiometer operated at the Swedish Institute of Space Physics, Kiruna, Sweden. In *Proceedings of the Sixth European Symposium on Stratospheric Ozone Research, Gothenburg*, pages 369–372, 2002.
- U. Raffalski, G. Hochschild, G. Kopp, and J. Urban. Evolution of stratospheric ozone during winter 2002/2003 as observed by a ground-based millimetre wave radiometer at Kiruna, Sweden. *Atmos. Chem. Phys.*, 5:1399–1407, 2005. doi: 10.5194/acp-5-1399-2005.
- C. E. Randall, V. L. Harvey, G. L. Manney, Y. Orsolini, M. Codrescu, C. Sioris, S. Brohede, C. S. Haley, L. L. Gordley, J. M. Zawodny, and J. M. Russell III. Stratospheric effects of energetic particle precipitation in 2003-2004. *Geophys. Res. Lett.*, 32:L05802, 2005.
- C. E. Randall, V. L. Harvey, C. S. Singleton, P. F. Bernath, C. D. Boone, and J. U. Kozyra. Enhanced  $\text{NO}_x$  in 2006 linked to strong upper stratospheric Arctic vortex. *Geophys. Res. Lett.*, 33:L18811, 2006.
- C. E. Randall, V. L. Harvey, C. S. Singleton, S. M. Bailey, P. F. Bernath, M. Codrescu, H. Nakajima, and J. M. Russell III. Energetic particle precipitation effects on the Southern Hemisphere stratosphere in 1992-2005. *J. Geophys. Res.*, 112:D08308, 2007a.
- C. E. Randall, V. L. Harvey, D. E. Siskind, J. France, P. F. Bernath, C. D. Boone, and K. A. Walker.  $\text{NO}_x$  descent in the Arctic middle atmosphere in early 2009. *Geophys. Res. Lett.*, 36:L18811, 2009.
- D. Randall, R. Wood, S. Bony, R. Colman, T. Fichet, J. Fyfe, V. Kattsov, A. Pitman, J. Shukla, J. Srinivasan, R. Stouffer, A. Sumi, and K. Taylor. Climate models and their evaluation. In S. Solomon, D. Qin, M. Manning, Z. Chen, M. Marquis, K. Averyt, M. Tignor, and H. Miller, editors, *Climate Change 2007: The Physical Science Basis. Contribution of Working Group I to the Fourth Assessment Report of the Intergovernmental Panel on Climate Change*. Cambridge University Press, 2007b.
- E. E. Remsberg, B. T. Marshall, M. Garcia-Comas, D. Krueger, G. S. Lingenfelter, J. Martin-Torres, M. G. Mlynczak, J. M. Russell, A. K. Smith, Y. Zhao, C. Brown, L. L. Gordley, M. J. Lopez-Gonzalez, M. Lopez-Puertas, C. She, M. J. Taylor, and R. E. Thompson. Assessment of the quality of the version 1.07 temperature-versus-pressure profiles of the middle atmosphere from TIMED/SABER. *J. Geophys. Res.*, 113:D17101, 2008. doi: 10.1029/2008JD010013.
- M. Rex, R. J. Salawitch, N. R. P. Harris, P. von der Gathen, G. O. Braathen, A. Schulz, H. Deckelmann, M. Chipperfield, B. Sinnhuber, E. Reimer, R. Alfier, R. Bevilacqua, K. Hoppel, M. Fromm, J. Lumpe, H. Küllmann, A. Kleinböhl, H. Bremer, M. von König, K. Künzi, D. Toohey, H. Vömel, E. Richard, K. Aikin, H. Jost, J. B. Greenblatt, M. Loewenstein, J. R. Podolske, C. R. Webster, G. J. Flesch, D. C. Scott, R. L. Herman, J. W. Elkins, E. A. Ray,

- F. L. Moore, D. F. Hurst, P. Romashkin, G. C. Toon, B. Sen, J. J. Margitan, P. Wennberg, R. Neuber, M. Allart, B. R. Bojkov, H. Claude, J. Davies, W. Davies, H. De Backer, H. Dier, V. Dorokhov, H. Fast, Y. Kondo, E. Kyrö, Z. Litynska, I. S. Mikkelsen, M. J. Molyneux, E. Moran, T. Nagai, H. Nakane, C. Parrondo, F. Ravagnani, P. Skrivankova, P. Viatte, and V. Yushkov. Chemical depletion of Arctic ozone in winter 1999/2000. *J. Geophys. Res.*, 107: 8276, 2002. doi: 10.1029/2001JD000533.
- M. Rex, R. J. Salawitch, P. von der Gathen, N. R. P. Harris, M. P. Chipperfield, and B. Naujokat. Arctic ozone loss and climate change. *Geophys. Res. Lett.*, 31:L04116, 2004.
- M. Rex, R. J. Salawitch, H. Deckelmann, P. von der Gathen, N. R. P. Harris, M. P. Chipperfield, B. Naujokat, E. Reimer, M. Allaart, S. B. Andersen, R. Bevilacqua, G. O. Braathen, H. Claude, J. Davies, H. De Backer, H. Dier, V. Dorokhov, H. Fast, M. Gerding, S. Godin-Beekmann, K. Hoppel, B. Johnson, E. Kyrö, Z. Litynska, D. Moore, H. Nakane, M. C. Parrondo, A. D. Risley, P. Skrivankova, R. Stübi, P. Viatte, V. Yushkov, and C. Zerefos. Arctic winter 2005: Implications for stratospheric ozone loss and climate change. *Geophys. Res. Lett.*, 33:L23808, 2006. doi: 10.1029/2006GL026731.
- C. P. Rinsland, R. J. Salawitch, M. R. Gunson, S. Solomon, R. Zander, E. Mahieu, A. Goldman, M. J. Newchurch, F. W. Irion, and A. Y. Chang. Polar stratospheric descent of  $\text{NO}_y$  and CO and Arctic denitrification during winter 1992-1993. *J. Geophys. Res.*, 104:1847–1861, 1999.
- C. D. Rodgers. *Inverse Methods for Atmospheric Sounding*. World Scientific Publishing, 2000.
- L. Rothman, D. Jacquemart, A. Barbe, D. C. Benner, M. Birk, L. Brown, M. Carleer, J. Chackerian, K. Chance, L. Coudert, V. Dana, V. Devi, J. Flaud, R. Gamache, A. Goldman, J. Hartmann, K. Jucks, A. Maki, J. Mandin, S. Massie, J. Orphal, A. Perrin, C. Rinsland, M. Smith, J. Tennyson, R. Tolchenov, R. Toth, J. V. Auwera, P. Varanasi, and G. Wagner. The HITRAN 2004 molecular spectroscopic database. *J. Quant. Spectrosc. Ra.*, 96:139–204, 2005. doi: 10.1016/j.jqsrt.2004.10.008.
- E. Rozanov, L. Callis, M. Schlesinger, F. Yang, N. Andronova, and V. Zubov. Atmospheric response to  $\text{NO}_y$  source due to energetic electron precipitation. *Geophys. Res. Lett.*, 32: L14811, 2005.
- R. J. Salawitch, S. C. Wofsy, E. W. Gottlieb, L. R. Lait, P. A. Newman, M. R. Schoeberl, M. Loewenstein, J. R. Podolske, S. E. Strahan, M. H. Proffitt, C. R. Webster, R. D. May, D. W. Fahey, D. Baumgardner, J. E. Dye, J. C. Wilson, K. K. Kelly, J. W. Elkins, K. R. Chan, and J. G. Anderson. Chemical loss of ozone in the Arctic polar vortex in the winter of 1991-1992. *Science*, 261:1146–1149, 1993.
- M. R. Schoeberl and D. L. Hartmann. The dynamics of the stratospheric polar vortex and its relation to springtime ozone depletions. *Science*, 251:46–52, 1991.
- M. R. Schoeberl, B. N. Duncan, A. R. Douglass, J. Waters, N. Livesey, W. Read, and M. Filipiak. The carbon monoxide tape recorder. *Geophys. Res. Lett.*, 33:L12811, 2006. doi: 10.1029/2006GL026178.
- A. Seppälä, C. E. Randall, M. A. Clilverd, E. Rozanov, and C. J. Rodger. Geomagnetic activity and polar surface air temperature variability. *J. Geophys. Res.*, 114:A10312, 2009. doi: 10.1029/2008JA014029.

- T. G. Shepherd. Transport in the middle atmosphere. *J. Meteorol. Soc. Jpn.*, 85B:165–191, 2007.
- D. T. Shindell, D. Rind, and P. Lonergan. Increased polar stratospheric ozone losses and delayed eventual recovery owing to increasing greenhouse-gas concentrations. *Nature*, 392:589–592, 1998. doi: 10.1038/33385.
- B.-M. Sinnhuber, M. Weber, A. Amankwah, and J. P. Burrows. Total ozone during the unusual Antarctic winter of 2002. *Geophys. Res. Lett.*, 30(11):1580, 2003. doi: 10.1029/2002GL016798.
- S. Solomon, P. J. Crutzen, and R. G. Roble. Photochemical coupling between the thermosphere and the lower atmosphere. 1. Odd nitrogen from 50 to 120 km. *J. Geophys. Res.*, 87(C9): 7206–7220, 1982.
- S. Solomon, R. R. Garcia, J. J. Olivero, R. M. Bevilacqua, P. R. Schwartz, R. T. Clancy, and D. O. Muhleman. Photochemistry and transport of carbon monoxide in the middle atmosphere. *J. Atmos. Sci.*, 42:1072–1083, 1985.
- S. Solomon, G. H. Mount, R. W. Sanders, R. O. Jakoubek, and A. L. Schmeltekopf. Observations of the nighttime abundance of OClO in the winter stratosphere above Thule, Greenland. *Science*, 242:550–555, 1988.
- T. Steck, T. von Clarmann, H. Fischer, B. Funke, N. Glatthor, U. Grabowski, M. Höpfner, S. Kellmann, M. Kiefer, A. Linden, M. Milz, G. P. Stiller, D. Y. Wang, M. Allaart, T. Blumenstock, P. von der Gathen, G. Hansen, F. Hase, G. Hochschild, G. Kopp, E. Kyrö, H. Oelhaf, U. Raffalski, A. R. Marrero, E. Remsberg, J. Russell III, K. Stebel, W. Steinbrecht, G. Wetzel, M. Yela, and G. Zhang. Bias determination and precision validation of ozone profiles from MIPAS-Envisat retrieved with the IMK-IAA processor. *Atmos. Chem. Phys.*, 7:3639–3662, 2007.
- S. Tegtmeier, K. Krüger, I. Wohltmann, K. Schoellhammer, and M. Rex. Variations of the residual circulation in the Northern Hemispheric winter. *J. Geophys. Res.*, 113:D16109, 2008a.
- S. Tegtmeier, M. Rex, I. Wohltmann, and K. Krüger. Relative importance of dynamical and chemical contributions to Arctic wintertime ozone. *Geophys. Res. Lett.*, 35:L17801, 2008b.
- A. Thorne. *Spectrophysics*. Chapman and Hall & Science Paperbacks, London, 1974.
- V. Velasco, S. W. Wood, M. Sinnhuber, I. Kramer, N. B. Jones, Y. Kasai, J. Notholt, T. Warneke, T. Blumenstock, F. Hase, F. J. Murcray, and O. Schrems. Annual variation of strato-mesospheric carbon monoxide measured by ground-based Fourier transform infrared spectrometry. *Atmos. Chem. Phys.*, 7:1305–1312, 2007. doi: 10.5194/acp-7-1305-2007.
- B. Vowinkel. *Passive Mikrowellenradiometrie*. Vieweg, 1988.
- J. Waters, L. Froidevaux, R. Harwood, R. Jarnot, H. Pickett, W. Read, P. Siegel, R. Cofield, M. Filipiak, D. Flower, J. Holden, G. Lau, N. Livesey, G. Manney, H. Pumphrey, M. Santee, D. Wu, D. Cuddy, R. Lay, M. Loo, V. Perun, M. Schwartz, P. Stek, R. Thurstans, M. Boyles, K. Chandra, M. Chavez, G. Chen, B. Chudasama, R. Dodge, R. Fuller, M. Girard, J. Jiang, Y. Jiang, B. Knosp, R. LaBelle, J. Lam, K. Lee, D. Miller, J. Oswald, N. Patel, D. Pukala, O. Quintero, D. Scaff, W. V. Snyder, M. Tope, P. Wagner, and M. Walch. The Earth Observing System Microwave Limb Sounder (EOS MLS) on the Aura satellite. *IEEE Trans. Geosci. Remote Sens.*, 44:1075–1092, 2006. doi: 10.1109/TGRS.2006.873771.

- J. W. Waters, W. J. Wilson, and F. I. Shimabukuro. Microwave measurement of mesospheric carbon monoxide. *Science*, 191:1174–1175, 1976. doi: 10.1126/science.191.4232.1174.
- D. W. Waugh and P.-P. Rong. Interannual variability in the decay of lower stratospheric Arctic vortices. *J. Meteorol. Soc. Jpn.*, 80:997–1012, 2002.
- WMO. Scientific assessment of ozone depletion: 2010. *Global Ozone Research and Monitoring Project*, Report No. 52, 2011.
- S. C. Wofsy, J. C. McConnell, and M. B. McElroy. Atmospheric CH<sub>4</sub>, CO, and CO<sub>2</sub>. *J. Geophys. Res.*, 77:4477–4493, 1972.



# Acknowledgements

I very much appreciate the great support, personal interest, and encouragement, which I experienced in the past years during my work on this thesis. It is a great pleasure to recall all these key moments during which personal interactions with colleagues, partners, and friends inspired me to push this work forward. I am deeply grateful to all these people and would like to mention a few of them in the following.

I thank Justus Notholt for the possibility to conduct this work in his research group, for giving me sufficient room to develop the project independently with my own ideas, and for supporting their realization whenever necessary. I am grateful to Mathias Palm for the very close cooperative work, his advice on scientific and technical issues, the permanent approachability, the steady encouragement, and the intense discussions throughout the whole project. Christian von Savigny and Markus Rex agreed willingly on being external members of my PhD-committee and supported me throughout the whole project. I appreciate their willingness to share their expert knowledge and to answer all my questions in readily understandable words. Furthermore, I would like to thank Christian von Savigny for agreeing to be the second reviewer of this thesis.

I would like to thank all my present and former colleagues at the IUP at the University of Bremen for creating such an enjoyable working climate for supporting my work in various aspects. I thank Sven Golchert for being very helpful and committed in every respect and particularly for many insightful discussions on the microwave technique, retrieval issues, and the associated pitfalls. Without being directly involved in my every day work, Tine Weinzierl was all the more important for maintaining a positive mood after failings and even more for enjoying all the small steps forward. Nadine Wieters was a constant companion during my time at the IUP and it was a pleasure to be with her on all the conference trips, especially in Granada. Nadine together with her modeling colleagues Holger Winkler and Miriam Sinnhuber were, furthermore, very involved in supporting the modeling aspects of my work. I would like to thank my office colleagues Katinka Petersen, Christof Petri and Stefan Kowalewski for the relaxed, but effective, office atmosphere, for lots of spontaneous discussions and even more for all the jokes, laughter, and shared sweets. Moreover, I would like to thank Birgit Teuchert and Peter Grupe for the important supportive work regarding administration and IT issues.

The success of my PhD-project is strongly connected to close collaborations with external partners and it was a great pleasure to work with all these people from different parts of the world. I would like to thank Uwe Raffalski (IRF, Kiruna, Sweden) for making the unpublished KIMRA CO spectra available for my work, as well as for the pleasant correspondence throughout the whole project. I am deeply grateful to the WACCM group at NCAR, Boulder, USA, especially to Douglas Kinnison and Rolando Garcia. My research stay at NCAR was an inspiring, effective, and refreshing time and became the highlight of my time as doctoral candidate. The special scientific atmosphere at NCAR, the contact to NCAR staff and visitors from all over the world, and particularly the guid-

ance by the WACCM group made this stay a unique experience, which I would not want to have missed. I am, furthermore, pleased about the fact that this close cooperation remained lively after returning to Bremen. Aside from having me as a guest for three months, I would like to thank the WACCM group for making available the unpublished SD-WACCM model data. I would like to thank Bernd Funke (IAA, Granada, Spain) for making available the MIPAS NOM and the unpublished MIPAS MA data and even more for the pleasant correspondence and the detailed discussions. I would like to thank the MIRA group (KIT, Karlsruhe, Germany), particularly Gerd Hochschild and Jochen Groß, for the long-standing close cooperation and especially for supporting me in understanding the technical details of the KIMRA instrument, which they originally developed. Furthermore, I thank the groups of ACE-FTS, MLS, SABER, and ECMWF for providing the respective datasets.

I enjoyed being a member of Earth System Sciences Research School (ESSReS), alongside my work on this thesis. I thank ESSReS and particularly the ESSReS coordinator Klaus Grosfeld for offering and organizing this well balanced mixture of interdisciplinary courses, seminars, excursions, and personal coachings, which was an important enrichment of my time as doctoral candidate. Moreover, I would like to thank Klaus Grosfeld for his strong personal interest in the progress of my work and his steady encouragement. I would like to thank all ESSReS students for their inspiring company in the past years.

I appreciate that Denise Müller agreed willingly to proofread this manuscript and I thank her for quickly, professionally, and patiently accomplishing this inconvenient work. Furthermore, I thank Janina Messerschmidt and Nicholas Deutscher for helpful comments on the manuscript.

Finally, I would like to thank my family and my friends for supporting this work in many ways. Particularly, for motivating me by showing interest in my work and in the broad field of environmental science, for reminding me that there are still things to be discovered beyond science, and for their understanding when I was short on time. Special thanks go to my parents, Monika and Waldemar Hoffmann, for their steady confidence in me and for supporting my decision to extend my academic education with a doctorate.

**Financial support.** This project has been funded by the German Research Foundation (Deutsche Forschungsgemeinschaft, DFG) with the projects NO 404/8-1 and PA 1714/3-2.

A three-month research stay at the National Center for Atmospheric Research (NCAR) in Boulder, USA, for the preparation of the KIMRA–SD-WACCM4 comparison was funded by the German Academic Exchange Service (Deutscher Akademischer Austauschdienst, DAAD).

A one-week business trip to San Francisco, USA, for the attendance of the Fall Meeting 2010 of the American Geophysical Union (AGU) in was funded by the Earth System Sciences Research School (ESSReS), an initiative of the Helmholtz Association of German research centers at the Alfred Wegener Institute for Polar and Marine Research.